UAV-RGB and Multispectral Pleiades images, for tree species identification and forest carbon estimation in Amtsvenn, Germany.

AGBOR ESONG EFFIOM
FEBRUARY, 2018

SUPERVISORS:
ir. L.M. van Leeuwen – de Leeuw
dr. P. Nyktas

UAV-RGB and Multispectral Pleiades images, for tree species identification and forest carbon estimation in Amtsvenn, Germany.

AGBOR ESONG EFFIOM
Enschede, The Netherlands, FEBRUARY, 2018

Thesis submitted to the Faculty of Geo-Information Science and Earth Observation of the University of Twente in partial fulfilment of the requirements for the degree of Master of Science in Geo-information Science and Earth Observation.
Specialization: Natural Resources Management

SUPERVISORS:
ir. L.M. van Leeuwen – de Leeuw
dr. P. Nyktas

THESIS ASSESSMENT BOARD:
dr. Y. A. Hussin (Chair)
dr. T.L.U. Kauranne (External Examiner, Lappeenranta University of Technology, Finland)

ABSTRACT

Forest carbon estimation currently relies on remote sensing technics, in combination with field measurement. High-resolution active sensors are commonly utilized for carbon estimation, but their cost prohibits communities from reaping the benefits of maintaining their forest under the UN REDD+ programme. Images from these platforms are not readily available, and their use still suffers from species identification problems. Multispectral Pleiades is cheaper but lacks sufficient spatial resolution for scene description. UAV-RGB platforms are inexpensive and flexible but their low spectral resolution camera limits species identification. This study explored the combination of UAV-RGB and multispectral Pleiades images for species classification and carbon estimation through Object Based Image Analysis. As a starting point, the present study assessed the effect of flight pattern and flight height of the DJ Phantom 4 for optimal image calibration. Then, the study investigated the effect of filtering on segmentation accuracy of UAV-RGB images, and evaluated the effect of combining multispectral pleiades with UAV-RGB on the segmentation accuracy for Crown Projection Area estimation. In addition, the study compared the performance of Multi-Resolution and Simple Linear Iterative Clustering segmentation algorithms. Further more, the effect of combining multispectral pleiades with UAV-RGB on the classification accuracy was measued, and the performance of Support Vector Machines, Random Trees and Maximum Likelihood classifiers in ArcMap was assessed. Finally, CPA-DBH relationships for main tree species were evaluated and used to model DBH, and carbon. The results show that flight pattern of Phantom 4 with RGB camera over forest stands has an effect on the quality of point cloud and orthophoto, with parallele flight plan having more chances to produce better quality point cloud and orthophoto. Also, the flight height above tree canopy has a strong influence on the number of calibrated images. The study demonstrates that the addition of multispectral pleiades image significantly increased the accuracies of segmentating and classifying UAV-RGB images ($p < 0.05$). Also, the classifications of SVM and RT classifiers is significantly better ($p < 0.05$) than that of the ML classifier. The modelled DBH and AGB for Scots pine and Birch were not significantly different from the field derived DBH and AGB. UAV-RGB and UAV-Pleiades images, combined in the procedure described in this work have potentiall to isolate tree species, model DBH and fores AGB.

Keywords: UAV-RGB, multispectral Pleiades, OBIA, tree-species identification, Carbon estimation.

ACKNOWLEDGEMENTS

This is the time to appreciate the support from the University of Twente and the Faculty of ITC through the UTS-ITC Excellence Scholarship programme for the opportunity to pursue this MSc. Degree. A peaceful salute to all the staff of ITC faculty, especially those of the department of NRS for sharing their knowledge, and for the series of workshops that guided the reporting of this research work.

Sincere gratitude goes to Ms Ir. L.M. Louise van Leeuwen and dr. P. Nyktas for supervising this thesis. Their guidance and constructive feedback, comments and encouraging words throughout this thesis phase have been remarkable. Your patience and kindness are highly appreciated.

Many thanks also to dr Yousif Hussin, for his comments and suggestions during the proposal and mid-term defence. I am thankful to the remote sensing and UAV labs for their great support during image acquisition. Many thanks also to Mr Watse and Wouter Borre for their pilot services employed during image acquisition in Amtsvenn and Neede respectively.

I am grateful to J. Erdbrügger, for making available her field work data, which I used to conduct this study.

I commend the love, and encouragement that sprang from across the student community in ITC especially from beautiful mates in NRS, great friends from GFM, LA, EO and UPM. Those words we shared along our path to ITC hotel, and in the kitchens of ITC hotel, and all through the course of the ups and downs that characterize our study were encouraging.

Okojie, Enuwamhangbe, Akpejiori, Sheikh, Usman McOkoye, Roni, Ning, Badui, Robert and Miller, thank you all for being there at the moments you did.

I am indebted to my family, especially Victor E.Mengot for their patience, love, care and financial support throughout my stay in Enschede.

Above all, I thank the Almighty God for the Grace to complete.

Agbor Esong Effiom
Enschede, The Netherlands
February 2018.

TABLE OF CONTENTS

LIST OF FIGURES

LIST OF TABLES

1. INTRODUCTION

1.1. Background

Forests play a significant role in the fight against the impacts of climate change. Four billion hectares of forest worldwide (equivalent to 31% of the total land area), contribute to the ecology, social, and economic proponents of life (FAO, 2010). Forests and forest soils store more than one trillion tons of carbon, twice the amount free in the atmosphere (Bonan, 2008). Forests share 80% of total exchange of carbon between the atmosphere and the terrestrial ecosystem (Koju, Zhang, & Gilani, 2017). A healthy and growing forest stand sequesters carbon and reduces the concentration of CO2 in the atmosphere. On the other hand, a degraded, cleared or burned forest increases the amount of heat-confining carbon dioxide (CO2) into the atmosphere, enhancing climate change and its effects. The conversion of forest to other land use types is responsible for ten percent of net global carbon emissions(IPCC, 2013). Thus, monitoring forest aboveground carbon is vital for assessing the effectiveness of policies geared towards halting or reversing deforestation.

Forest aboveground carbon is about 50% of the Above Ground Biomass (AGB) (Assefa, Mengistu, Getu, & Zewdie, 2013). AGB is the mass of all the organic matter in plant tissues above the soil including stem, branches, foliage, bark and seeds (Gibbs & Herold, 2007). There is a growing need for consistent forest biomass monitoring, in the context of sustainable livelihood, ecosystem services and Reducing Emissions from Deforestation and forest Degradation (REDD+). Under the REDD program, member nations must estimate their baseline carbon stocks, monitor, record and verify any changes due to the implementation of their emission reduction programs to benefit financially (Patenaude, Milne, & Dawson, 2005; Ward, 2013).

Forest emissions reduction and greenhouse gas inventories programs need rigorous scientific methods to quantify carbon stocks across different landscapes over time (Gonzalez et al., 2010). Approaches to biomass and carbon estimation include field measurements, GIS-based assessments and remote sensing (Dengsheng Lu, 2006). GIS-based methods extrapolate existing forest inventory volume data to biomass using wood density. Remote sensing based methods use the statistical relationship between satellite extracted tree parameters and ground-based measurements for biomass estimation (Gibbs & Herold, 2007).

Forest tree parameters such as Crown Projection Area (CPA), Diameter at Breast Height (DBH) and tree Height (H) are estimated by recent and accurate remote sensing methods(White et al., 2016; M a Wulder, 1998; Z. Zhang, Cao, & She, 2017), and used together with species-specific allometric equations to assess carbon stocks. Remote sensing methods rely on the reflectance of the tree crowns, and this is the portion recognised from the image. The relationship between CPA and DBH for tree species is essential for estimating aboveground carbon. The relationship is built using the CPA extracted from the remotely sensed image. Once the CPA is known, DBH and related biomass can be calculated (Obeyed, 2014; Onilude, Akinyemi, Julius A.J, Ogunremi, & Ogunremi, 2015; Shah & Acharya, 2010; Sharma, Vacek, & Vacek, 2016). However, the relation between DBH and biomass is species specific, depends on wood density, thus, there is a growing need for carbon assessment methods to capture tree species-specific information (Schwenk, Donovan, Keeton, & Nunery, 2012).Spatial heterogeneity in species composition and stand structure of forest play a sensitive role in accurate carbon estimation (Hu, Su, Li, Li, & Ke, 2015). Thus, to sustainably manage the forest, it is crucial to increase the precision of carbon stock measurements with species-specific allometric equations to capture biodiversity and ecosystem services.

Multispectral imagery, like Geo-Eye, Worldview, IKONOS, Birdseye and Quick Bird have been used to extract forest inventory parameters for individual tree species and vegetation classification (M. A. Wulder, White, Niemann, & Nelson, 2004), and carbon estimation (Karna et al., 2015; Fassnacht et al., 2016). The availability of these high-resolution images brought a shift from the traditional Pixel Based (PB) to Object-Based Image Analysis (OBIA), which is considered ideal for tree crown delineation and species isolation (Ke, Quackenbush, & Im, 2010; Zhang & Qiu, 2012). The fundamental processes in OBIA are segmentation and classification, mostly performed in the eCognition environment. Accurate segmentation of individual tree crowns (as CPA) supports improved species identification, better estimates of aboveground carbon and sustainable forest management (Pouliot, King, Bell, & Pitt, 2002).

The eCognition software package is robust with promising performance and is host to different segmentation and classification algorithms. Multiresolution, region growing and multiresolution region growing are common segmentation algorithms in eCognition. Classification algorithms in eCognition include Maximum likelihood (ML), K-Nearest Neighbour (K-NN), Support Vector Machine (SVM) and Random Trees (RT) algorithms. However, other segmentation and classification algorithms are implemented in ESRI's ArcMap and different environments with little or no additional cost. It is common practice to use ArcMap, eCognition and other commercial software for segmentation and classification because of their robustness. However, a reduction in the number of commercial software to estimate AGB could be cost relieving for communities and organisations involved. Therefore, the use of ArcMap (commercial) and open-source environments can be relatively cheaper compared to the use of ArcMap and eCognition (both commercial). For example, segmentation can be done in R-environment (open source), while classification can be done in ArcMap. Simple Linear Iterative Clustering (SLIC) is a segmentation algorithm implemented as a plugin in QGIS (Crommelinck et al., 2017), GRASS GIS (Kanavath & Metz, 2017).SLIC can also be executed in R (Adelabu, Mutanga, Adam, & Cho, 2013), and Python. Maximum likelihood (ML), Nearest neighbour (NN), Random Trees (RT), Random Forest (RF) and Support Vector Machines (SVM) are supervised classification algorithms implemented in R, Python, and ArcMap environments.

Unmanned Aerial Vehicles (UAVs) are platforms capable of carrying sensors for monitoring, and mapping of the environment and natural resources. According to Nex & Remondino (2014), UAVs come in varied flavours, and constitute an essential source of relatively cheaper remote sensing data for applications in many fields; including, but not limited to agriculture, forestry, mining, urban planning, and land management. UAVs can be of fixed wing or Rotary blade and can carry RGB, multispectral sensor or even Lidar depending on the weight of the UAV (Bailey, 2012).

Species identification has been carried out using high-resolution optical UAV images (Näsi et al., 2016; Nevalainen et al., 2017). The extraction of tree structural parameters (Birdal, Avdan, & Türk, 2017; Ramón, Raúl, Lorenzo, & Pablo, 2015; Zarco-Tejada, Diaz-Varela, Angileri, & Loudjani, 2014) for carbon estimation has been performed using High-resolution imagery from optical UAV. The results from the mentioned studies have been promising. The processing of UAV images follows a photogrammetric workflow to generate 3D products (point cloud, digital surface model, and orthophoto) as main outputs. The quality of the point cloud and orthophoto depends on the quality, number and distribution of ground control points, focal length of the camera sensor, and flight parameters like flight height, forward and side overlap, and flight pattern (Nasrullah, 2016), and climatic conditions.

Accurate species discrimination requires high spectral resolution, while a precise description of texture and shape (in segmentation) needs high spatial resolution (Ghassemian, 2016). UAVs capture images with high spatial resolution, and when equipped with multispectral sensors, they provide high spectral resolution images required for segmentation and species identification. However, multi or hyperspectral sensors are more expensive than the UAV itself. For this reason, most UAVs use low-cost RGB camera sensors, which produce images with high spatial but low spectral resolution from which species recognition is challenging.

Image integration could be the way to enhance tree species identification with UAV-RGB images (Sahu & Parsai, 2012; Sheldon, Xiao, & Biradar, 2012; Ghassemian, 2016). Image integration is a process of exploiting the strengths of two or more images from same or different sensors to achieve better results. Integration here refers to the addition and final mixing of image properties, or the addition of image layers (no blending of properties) (Alkema, Bijker, Sharifa, Vekerdy, & Verhoef, 2013). Image integration can extend to fusion, where relevant information from a set of images is combined and mixed into a single, more informative and complete image (Sahu & Parsai, 2012). Image fusion could involve merging a high spatial resolution panchromatic image and a rich multispectral image to obtain a spatially and spectrally enhanced image (Jagalingam & Hegde, 2015). On the other hand, image integration could be limited to the overlaying of multi-source or multi-sensor images as separate layers in a procedure to enhance the quality of expected output (Alkema et al., 2013). The inability of a single imaging sensor to completely capture all the necessary information for detecting an object or classify a scene is the reason for the full exploitation of multi-source data integration and advanced image analytical or numerical procedures (Ghassemian, 2016). High spatial resolution imagery produced by UAVs may address the challenge of species identification if spectrally enhanced by combining it with an image from a high-resolution multispectral sensor which has NIR or Red-edge band.

1.2. Research problem

UAVs are relatively cheaper and flexible, producing images with potentials for the estimation of tree structural parameters and tree species identification. The quality of images and resulting 3D products from UAV platforms depends on a host of factors; including, flight altitude, overlap (side and forward), camera sensor on board, camera focal length, shutter exposure speed, lens aperture and environmental factors like wind, sun, clouds and rain. However, the determination of optimal flight parameters necessary to produce good quality 3D products must precede the use of UAV images for segmentation and tree species classification. Studies reported that Canon ELPH 520 HS digital camera, when attached to a commercial multirotor UAV produces good quality 3D products at a flight height of 20m above trees, with side overlap of 80% (Dandois, Olano, & Ellis, 2015; Nasrullah, 2016). DJ Phantom 4 is a new and relatively cheaper drone, with RGB inbuilt camera sensor, reinforced gimbal for greater flight stability, and refined motors for increased flight efficiency (DJ phantom four user manual). DJ phantom 4 images captured with inbuilt RGB camera sensor have been used to estimate tree crown projection area, tree height and subsequent carbon estimation (Hongoa, 2017; Mtui, 2017; Okojie, 2017). However, setting optimal flight height and pattern over forest stands is problematic (Erdbrügger, 2017), with sub-optimal parameters resulting in poor quality images and 3D products derived from the processing of corresponding images. There is a need to investigate optimal flight parameters systematically.

The high-resolution RGB image produced by UAVs can be integrated with multispectral satellite images having the near-infrared band for species identification (Yilmaz & Gungor, 2016) or vice versa. Unlike IKONOS, Worldview, Quick Bird and Birdseye, Pleiades constellations (50cm resolution) provide high-resolution multispectral data in record time with a daily revisit capability at any point on the globe (ASTRIUM, 2012). The Panchromatic version of multispectral images are relatively cheap but cannot be used as standalone for tree crown delineation due to the effect of shadow in the visible spectrum (Srijana Baral, 2011; Haijian, Qiming, & Xinyi, 2008). Most studies involving image integration have done so through one of the many fusion methods, which end up with spectral and or spatial distortions (Pandit & Bhiwani, 2015; Sivagami et al., 2015; Ghassemian, 2016). Few studies have integrated UAV and multispectral Pleiades images, especially as separate layers.

The eCognition software package provides the opportunity for object-based image analysis (OBIA), which is required for the analysis of very high-resolution data. In OBIA, two images are combined as separate layers for segmentation and classification, thus maintaining their spectral and spatial characteristics. Most of the OBIA is performed in the eCognition environment, a robust software package, with promising performance and a host to different segmentation and classification algorithms, but costly (Ke et al., 2010; C. Zhang & Qiu, 2012). Since ArcMap is often used in the post-processing of segmentation and classification results, and it is equally expensive, the entire process of image analysis for AGB estimation becomes unaffordable for most communities and organisations. Despite the availability of different segmentation and classification algorithms in eCognition, their performance has not been compared. However, other platforms are available such as R, Python, QGIS, GRASS where segmentation and classification are possible. These algorithms have not been deeply exploited in literature, and their performance for species identification and carbon estimation has not been compared.

This research aims to explore a low-cost method for high accuracy carbon estimation. The work combines UAV-RGB and multispectral Pleiades images in a procedure that could result in accurate segmentation, species identification, and carbon estimation. It investigates optimal flight parameters for phantom 4 drone over forest stands, compares the accuracy of segmenting UAV-RGB and UAV-Pleiades image configurations in eCognition and R, compares the accuracy of classifying the two image configurations, and finally estimates above ground carbon of dominant tree species.

1.3. Research objective

The primary objective of this research is to assess the added value of combining the UAV-RGB image with multispectral Pleiades image in object-based image analysis for accurate tree crown segmentation, tree species classification and carbon estimation in a temperate forest.

The specific objectives are to;

1. Determine optimal flight pattern and height over forest stand using DJ phantom 4 with RGB camera.
2. Compare the accuracies of segmenting UAV-RGB and UAV-Pleiades images using multiresolution, Simple Linear Iterative Clustering (SLIC), in eCognition, and R environments respectively.
3. Compare the accuracies of tree species classification using Maximum Likelihood, Random Trees and support vector machine classifiers ArcMap
4. Compare the estimated carbon dominant species from field derived DBH and predicted DBH using classified image with the highest accuracy.

1.4. Research questions

1. Which flight pattern is optimal to generate a high-quality point cloud of forest stands using DJ Phantom 4 with RGB camera?, and which flight height yields optimal image calibration?

2. Which image configuration: produces better segmentation (UAV-RGB or UAV-RGB combined with the Pleiades?, and which algorithm: Multi-resolution or SLIC segments with the highest accuracy?

3. What is the difference in classification accuracy of UAV-RGB and UAV-Pleiades images, and which algorithm: Maximum Likelihood, Random Trees and Support Vector Machine classifiers with the highest accuracy?

4. What is the difference in aboveground carbon of dominant tree species estimated from field DBH and predicted DBH using the best-classified image?

1.5. Research hypothesis

The assessment of question will be qualitative, thus the hypothesis presented below are for research questions 2, 3 and 4. T

RQ 2a.

H_O: There is no significant difference in the accuracies of segmenting UAV-RGB and UAV-Pleiades images using Multi-resolution and SLIC algorithms in eCognition and R environments respectively.

H_A: There is a significant difference in the accuracy of segmenting UAV-RGB and UAV-RGB combined with Pleiades images using Multi-resolution and SLIC algorithms in eCognition and R environments respectively.

RQ 2b.

H_O: There is no significant difference in the accuracies of Multi-resolution(eCognition) and SLIC(R) segmentation of UAV-RGB and UAV-Pleiades images.

H_A: There is a significant difference in the accuracies of Multi-resolution(eCognition) and SLIC(R) segmentation of UAV-RGB and UAV-Pleiades images.

RQ 3a.

H_O: There is no significant difference in tree species classification accuracies using segmented UAV-RGB and UAV-Pleiades image configurations.

H_A: There is a significant difference in tree species classification accuracies using segmented UAV-RGB and UAV-Pleiades image configurations.

RQ 3b.

H_O: There is no significant difference in the accuracies of tree species classification done by Maximum Likelihood, Random Trees and Support Vector Machines classifiers using segmented UAV-RGB and UAV-Pleiades image configurations.

H_A: There is a significant difference in the accuracies of tree species classification done by Maximum Likelihood, Random Trees and Support Vector Machines classifiers using segmented UAV-RGB and UAV-Pleiades image configurations.

RQ 4.

H_O: There is no significant difference in the above ground carbon of the dominant tree species estimated from field DBH and predicted DBH.

H_A: There is no significant difference in the above ground carbon of the dominant tree species estimated from field DBH and predicted DBH.

2. MATERIALS AND METHODS

2.1.Description of study area

This study made use of forest blocks in nature reserves in Amstveen and Neede village. Both Amtsvenn and Neede areas are rural with landscape composed of forest patches and agricultural fields. Amtsvenn is close to the city of Gronau in Germany, at the boundary of the Netherlands and Germany, situated at longitude 32558395m E and 5782262m N of UTM 32 N, ETRS89. As can be seen in figure 2-1 below, the Amtsvenn area is host to eight forest blocks, five of which were considered for this study. As can be seen in figure 1 below, the blocks with red polygons are those recruited for this study. The Amtsvenn area was chosen for this study because related work had been started the previous year. Establishing contacts and permit was expected to be much easier.

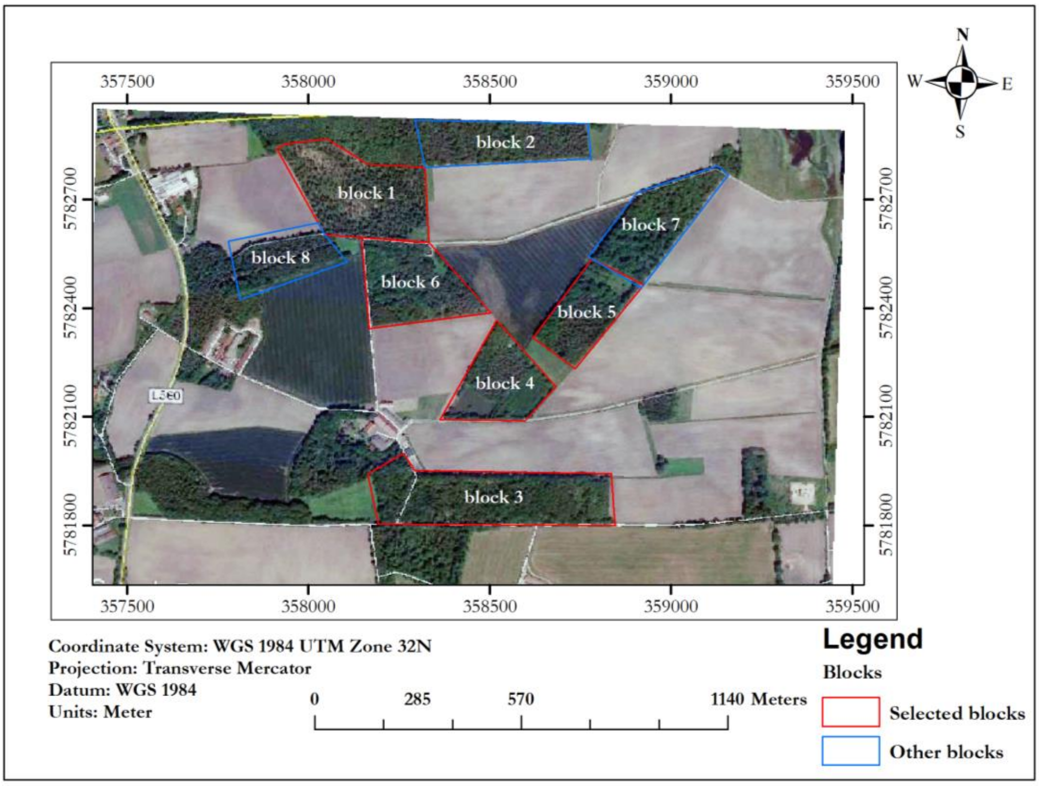

Figure 2-1: Map, showing forest blocks and selected blocks in Amtsvenn, Germany.

The area is divided into blocks with different stand density, structure and composition. Block 1 is an open forest mainly dominated by Scots pine. The tree crowns occupy same canopy level, with spaces between the crowns. Blocks 2 3,4,5 and 6 are dense mixed forest stands, with tree crowns of different sizes, and at different canopy levels. Each of these blocks consists of more than two tree species.

Figure 2-2 below shows the forest block in Neede village. Neede village is located in Berkelland municipality, within the Gelderland province of Netherlands. The community is host to the State-owned forest reserve. The red polygon shows the boundary of the forest block used in this study to augment the need to investigate the effect of flight height on image calibration.

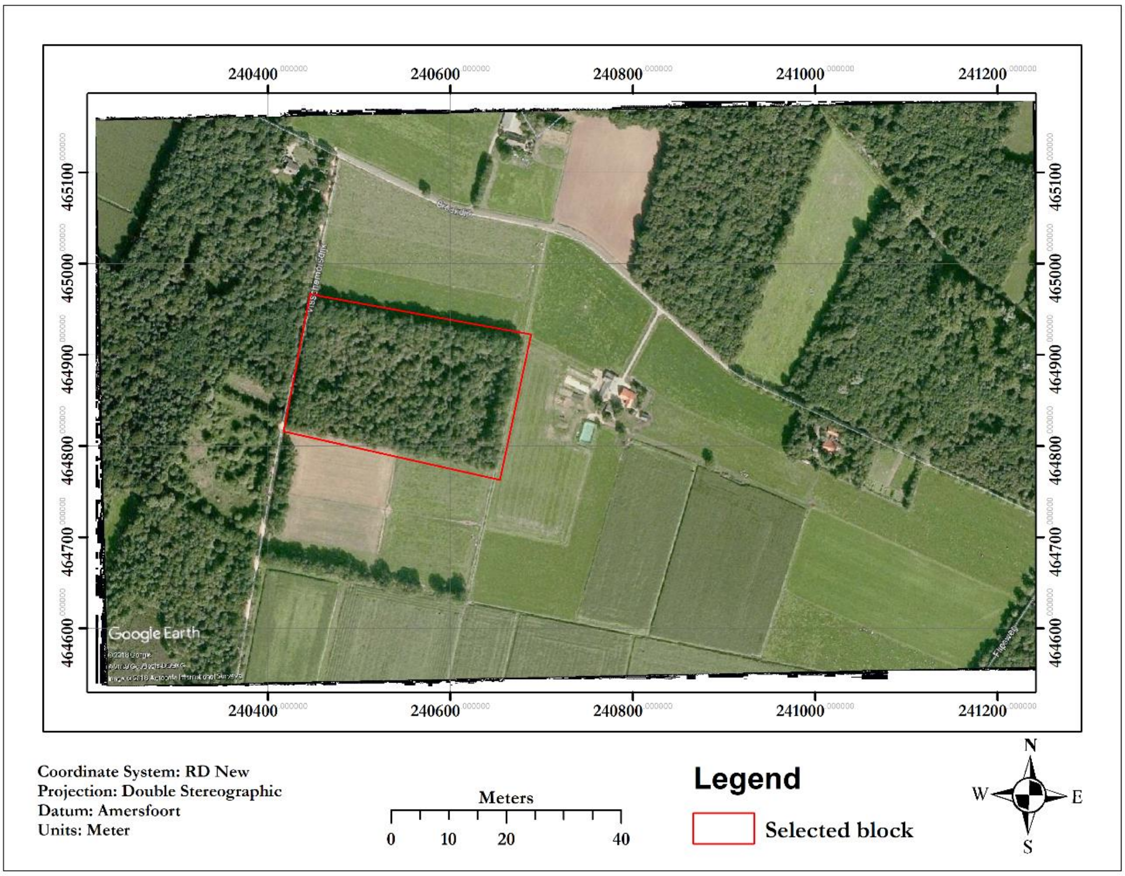

Figure 2-2: State-owned forest block in Neede village, Netherlands.

2.1.1. Climate

Both locations of the study areas experience similar climate conditions, along with the Dutch borders with Germany. They have a temperate climate with a mean monthly temperature of 9.1°C and annual precipitation of about 785mm (Climate-Data.org, 2017). Rainfall is lowest in February (mean of 45mm) and highest in July (mean of 79mm). Average wind speed in these areas is about 4.1 meters per second in the months from January to April and from November to December, while from May to October the mean wind speed is approximately 3.5 meters per second (Weather and Climate.com, 2017). Such wind data guides flight planning for best time to collect data with the drones.

2.1.2. Vegetation

Amtsvenn and Neede areas have several forest blocks within agricultural fields. The forest stands have different stand densities, the composition of both coniferous and deciduous trees, while the farms are predominantly composed of maize and grass. Beech (*Fagus sylvatica*), Scots pine (*Pinus sylvestris*), Oak (*Quercus robur* and *Quercus petraea*), Alder (*Alnus sp*), Douglas fir *(Pseudotsuga menziesii*), European hornbeam and Birch (*Betula sp*) are the most common tree species in the Amtsvenn area (Erdbrügger, 2017; Okojie, 2017). The forest block in Neede is composed of white Birch of different ages, Oak and Scots pine with a mean tree height of 20m for upper story trees.

2.2. Dataset

This study made use of remotely sensed and field data. As seen in table 2-1, true orthophoto (UAV) and multispectral Pleiades data of the study area were used.

Table 2-1: List of data set used, their sources and characteristics

Data type	Characteristic	Source
Multispectral Pleiades with R, G, B and NIR bands	50cm resolution, orthorectified	Airbus Ds Geo SA (through ITC RS lab)
UAV-RGB images	Captured at different heights and flight patterns	Fieldwork in Amtsvenn and Neede
UAV orthophoto Amtsvenn area	the 5cm resolution, RGB, captured with DJ phantom four drone	Erdbrügger (2016) dataset
Tree species, location and DBH	Plot-based, TLS scans and manual measurements	Erdbrügger (2016) field work dataset

Multispectral sensor data was essential for discriminating vegetation and tree species because of its NIR band, and Pleiades data was readily available in the ITC remote sensing lab. The image was aquired on the 4th of September 2014. The UAV flights were scheduled between the 25th August and 9th of September 2017, to reduce variation in image acquisition dates of the existing Pleiades image. However, due to permit issues, the first three flights were done in Amtsvenn, while four flights were done in Neede.
The list of software and equipment used in this study is presented in table 2-2 below.

Table 2-2: List of Software

Software/Algorithm	**Uses**
Pix4D	Photogrammetric Processing of UAV images
eCognition/Multi-Resolution	Segmentation-OBIA
R statistical package	segmentation
ArcMap	Image analysis and map production
Microsoft Office Word	Report writing/Thesis
Microsoft Office Excel	Statistical analysis/visualization
Differential GNSS Leica CS 15	Mark GCPs
DJ Phantom 4 drone	Acquire images

2.3. Methods

This section has four parts, as can be seen in figure 2-3 and figure 2-4 below.
Part 1 includes UAV flight planning, data capture, and field measurements.
Part 2 involves the processing of Pleiades and UAV images, data processing steps and formation of image configurations.
Part 3 looks at the segmentation of the UAV-RGB and UAV-Pleiades images to answer research questions 2a and 2b. It also includes segmentation accuracy of two image configuration and between the two segmentation algorithms. This part will produce the best-segmented image based on accuracy assessment.
Part 4 concentrates on the classification of the resulting images from section 2 using three different classification algorithms. It will answer research question 3 which investigates the difference in classification accuracy between image configurations and between the three classifiers.
Part 5 focuses on the modelling DBH and AGB. The modelled DBH and AGB were compared to infer statistical difference. This section answers question 4.

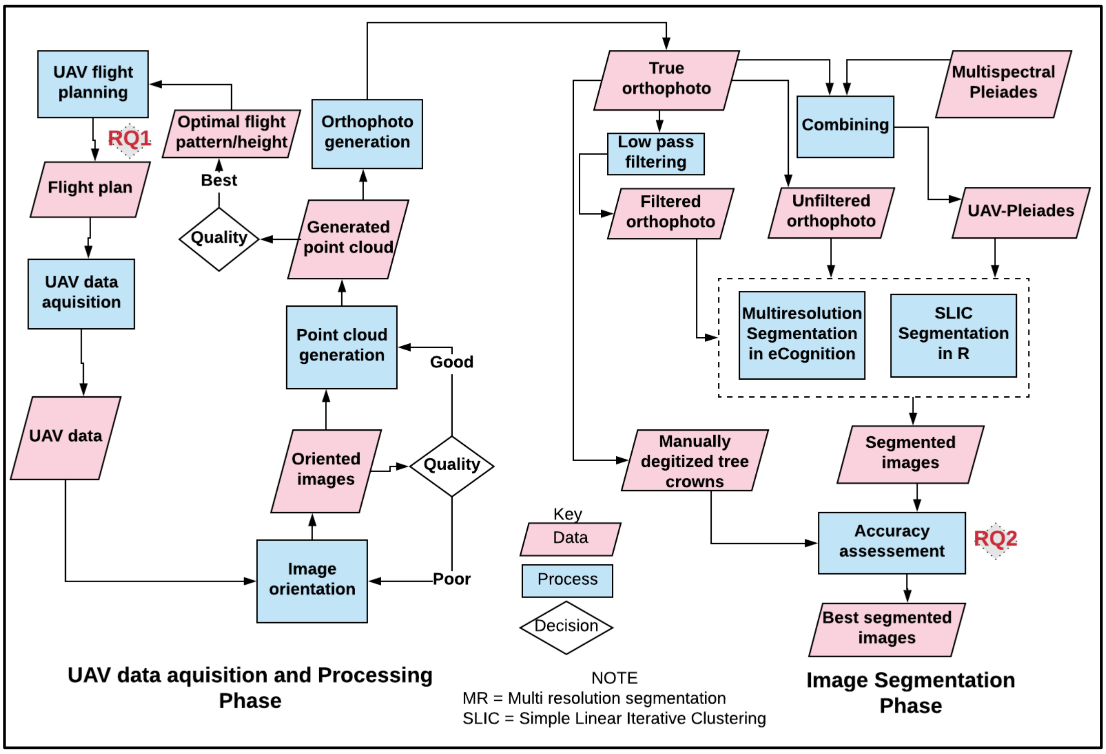

Figure 2-3: UAV data acquisition, processing and image segmentation workflow

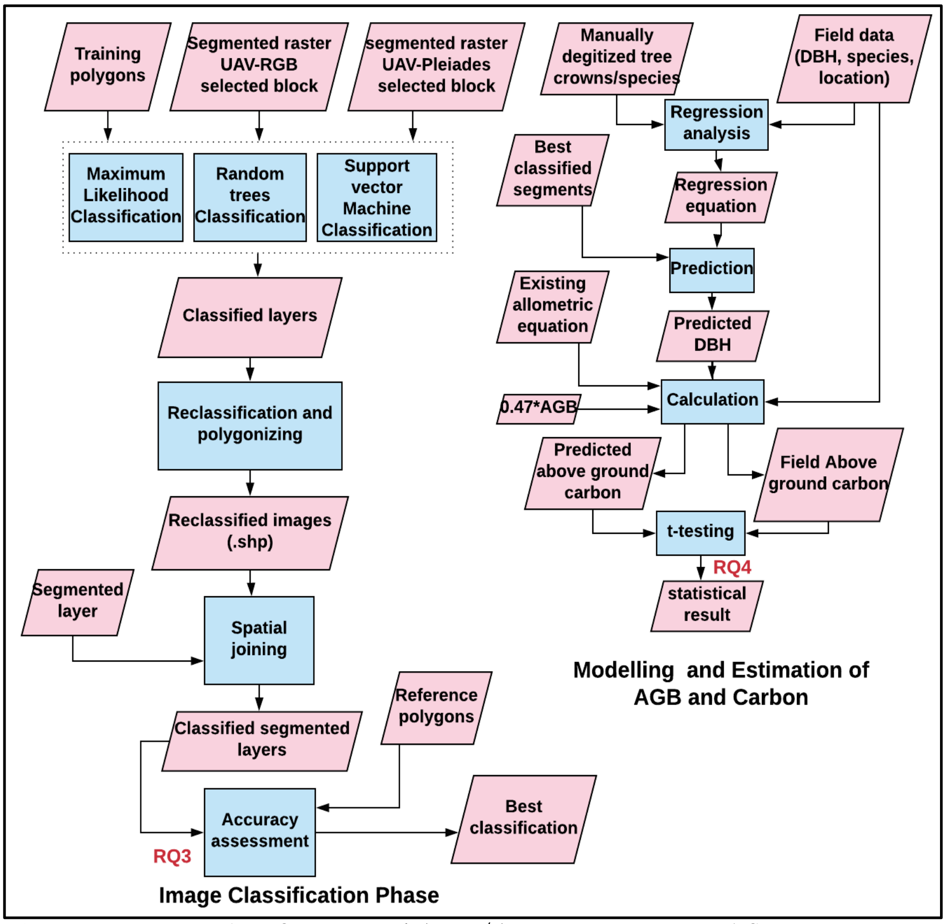

Figure 2-4: Image classification and AGB/AGC estimation workflow

2.3.1. UAV Data acquisition

UAV flights were performed over the 0.5km² study area after the establishment of sufficient and adequately distributed and appropriately located Ground Control Points (GCPs). The locations of GCPs were measured using the differential GNSS Leica CS 15. Accurate GCPs are essential to optimise the rigidity of the bundle block adjustment during image orientation. Preliminary flights were performed in Amtsvenn to investigate the influence of flight pattern on point cloud and orthophoto quality. All flights were conducted using forward and side overlap of 85% and 70% respectively. Three flights were done in Amtsvenn at heights of 40m and 45m in parallel and perpendicular grids (figure 2-5) to produce an orthophoto of 1.5cm resolution. Due to permit issues, subsequent flights could not be done in Amtsvenn. The three flights were thus used to assess the influence of flight pattern over open pine forest on the quality of resulting point cloud and orthophoto.

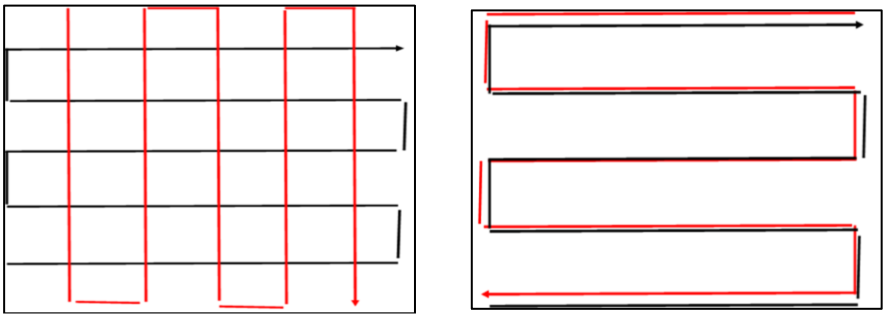

Figure 2-5: Double grid perpendicular and parallel flight patterns: flights at nadir, 85 and 70% forward and side overlap, varying flight heights above tree canopy

However, four single grid flights were performed over a 17.9ha forest stand in Neede village; The single grid flights were done at heights of 40m, 60m, 80m and 100m above tree canopy to investigate optimal flight height of the phantom 4 drone over forest stands. With a mean tree height of 20m, the flights had mean ground sampling distances of 2.5cm, 3cm, 4cm and 5cm respectively.

2.3.2. Field Measurements

Field data for the same area collected in 2016 were used to continue the study. Data harmonisation and extraction made use of GIS operations like query, editing of attribute tables, coordinate reconciliation, overlays, spatial joins and data export. The extracted point data of tree species and location were overlaid on the orthophoto to confirm with the described fifteen plot locations and tree identities in five of the blocks.

2.3.3. Sampling Design

According to the lineage of the 2016 data, a circular plot-based design was used for data collection (Erdbrügger, 2017). All trees with DBH greater than 10cm were recorded within a 500square meter circular plot (12.5m radius). Tree species, DBH and location, were recorded. Trees with DBH less 10cm were not recorded because their contribution to biomass is assumed negligible (Brown, 2002).

2.4. Data Processing

UAV-RGB images were captured using DJ Phantom 4 with RGB camera sensor on board, while Pleiades image of the same area was obtained from Airbus Ds Geo SA, through ITC RSLAB.

2.4.1. Pleiades data processing

The Pleiades dataset provided by ITC is orthorectified panchromatic and multispectral (RGB and NIR) images. The reference system of the Pleiades products was assessed. The study area was extracted by the mask from the multispectral Pleiades image with a georeferenced shapefile of the study area. The multispectral Pleiades image with the 50cm resolution was resampled to 30cm resolution in ArcMap to ensure that pixels from UAV and Pleiades fit well. Upscaling does not create any new or non-existing data but instead squeezes data occupying 50cm to fit into a 30cm pixel. The nearest neighbour resampling algorithm is chosen because it preserves pixel values (Baboo & Devi, 2010; Bakx et al., 2013).

2.4.2. UAV data processing

A total of 554 and 359 images were captured for the parallel and perpendicular flight patterns respectively over an area of 4.1ha in Amtsvenn. For the flights in Neede, 233, 157, 122 and 85 images were captured at heights of 60m, 80m, 100m and 120m from the ground respectively, over an area of 17.9ha. The UAV images were processed using Structure From Motion (SfM), the photogrammetric process of constructing three-dimensional structure of the scene, and camera position by analysing the sequence of images (Alcantarilla, Bartoli, & Davison, 2012). This process begins with tie-point detection, description, and matching to give the images relative orientation. The photos were given absolute orientation with coordinates on the ground (GCPs). A Random Sample Consensus (RANSAC) operation reduces reprojection errors during image orientation (Fischler & Bolles, 1981). Once the images have been correctly orientated, point cloud, digital surface model, and orthophoto are generated. The quality of the image orientation process determines the quality of the subsequent products. There are some software packages for processing UAV images. Amongst them are popular commercial packages like Pix4D Mapper (Pix4D), Agisoft Photoscan (PS), and Capturing Reality (ReCap) (Remondino, Nocerino, Toschi, & Menna, 2017). In this study, the UAV images were processed in Pix4D. In the pix4D software, processing goes through three critical stages; initial processing, point cloud densification and finally DSM and orthomosaic generation.

The initial processing phase involves tie-point detection, description, and matching to give the images relative orientation. Due to the side and forward overlap, consecutive images have similar features. Tie-points refer to 2D points identifying same features in different images. Once the images are loaded into pix4D, the software detects identical elements in the images. Based on these similar elements (2D points), a third point is located (3D point in space), and the images are given an orientation relative to one another in space With identified tie-points, the images are calibrated. The software then iteratively uses samples of the tie points to build a model that determines the best orientation of the images. This iterative process is described as Random Sample Consensus (RANSAC). RANSAC reduces the errors associated with giving the photos geolocation on the ground (fixed orientation) (Fischler & Bolles, 1981). Once the report shows sufficient image calibration, ground control points collected during fieldwork are loaded to optimise the calibration process and give the calibrated images geolocation on the ground (fixed orientation). Once the quality is appropriate, as revealed by green checks in the quality report, the next phase is initiated. As can be seen in the figure below, the green checks indicate sound quality of a successful processing phase.

Processed	2017-10-22 19:12:43
Camera Model Name(s)	FC330_3.6_4000x3000 (RGB)
Average Ground Sampling Distance (GSD)	4.07 cm / 1.6 in
Area Covered	0.1726 km^2 / 17.2617 ha / 0.0667 sq. mi. / 42.6766 acres
Time for Initial Processing (without report)	12m:29s

Quality Check

Images	median of 43991 keypoints per image	
Dataset	122 out of 122 images calibrated (100%), all images enabled	
Camera Optimization	0.21% relative difference between initial and optimized internal camera parameters	
Matching	median of 10353.1 matches per calibrated image	
Georeferencing	yes, 8 GCPs (8 3D), mean RMS error = 0.028 m	

Figure 2-6: A snapshot of an instance of quality check in Pix4D image processing

In the point cloud densification phase, based on the selected options like image scale, point cloud density, a densified point cloud is generated by aerial triangulation. Point cloud densification is important for the construction of orthophoto and other 3D products like DEM and DSM. The processing choice affects the processing time and quality. In this study, image scale for point cloud generation and densification was set to multiscale ½ image size, meaning half of the image quality is utilized, while point density was set to optimal. According to the Pix4D user manual, these point cloud generation and densification is the most "expensive" phase, requiring time and computer resources. These options, therefore, allow for a right balance between cost in time and computer resources and product quality(Pix4D SA, 2017). These options allow for a balance between quality and processing time.

The last phase, the generation of DSM and orthomosaic also requires the selection of proper options based on project requirements. In this project, the resolution of products was set to 1 x ground sampling distance (default), and the DSM was generated by triangulation because this method preserves the characteristics of points from the original image (Pix4D SA, 2017). At the end of each of the phases described above, the quality report guides the user whether to continue or not.

2.4.3. Filtering and Resampling UAV-RGB image

The resolution of the UAV-RGB orthophoto was high (3.4cm) and had some noise. It was filtered with a low pass filter in ArcMap and resampled to 30cm using nearest neighbour algorithm. Resampling to 30cm was done because this resolution has been reported to be suitable for segmentation of tree crowns (Okojie, 2017). Filtering removed small objects that induce noise, while resampling with the nearest neighbour preserves the spectral properties of each tree crown and prepares the resolution for better segmentation. However, for this study, filtered and unfiltered UAV-RGB images were used to analyse the influence of filtering on segmentation.

2.4.4. Formation of UAV Pleiades Image Configuration

UAV-Pleiades image configuration could be assembled through two procedures; uploading required bands (RGB from UAV and NIR from the multispectral Pleiades) in eCognition, or layer stacking the needed bands into one raster image using the Composite band tool in ArcMap. The first option was only possible in eCognition but not in the other segmentation environments. The second option was adopted to ensure a fair comparison. Required bands from UAV-RGB were layer stacked with the NIR band from the multispectral Pleiades. This procedure was successful when all the bands to be layer stacked were in the same 8unsigned or 16unsigned bits.

2.5. Object-Based Image Analysis

Object-based image analysis is a classification procedure that treats spatial features in an image as objects, rather than as pixels. The availability of very high-resolution images brought a shift in image analysis, from pixel-based to object based. Very high-resolution models are loaded with abundant information that cannot be sufficiently handled with pixel-based analysis (Wei, Chen, & Ma, 2005; Zhu, Cai, Liu, & Huang, 2016). The main parts of OBIA are segmentation and classification

2.5.1. Image Segmentation

Segmentation is the building block of OBIA. It identifies homogenous areas based on shape, colour, size, and groups them into specific objects called segments (Möller, Lymburner, & Volk, 2007). There are many different segmentation algorithms, amongst which multi-resolution is powerful when dealing with very high-resolution images (Belgiu & Drăguţ, 2014). Most of the other segmentation algorithms need to be adapted to extract specific objects of interest (Hay, Castilla, Wulder, & Ruiz, 2005). Adjusting makes the segmentation process highly subjective to trial-and-error (Arvor, Durieux, Andrés, & Laporte, 2013; X. Zhang, Wang, Yang, & Li, 2016). Segmentation algorithms are implemented in different environments, amongst which are eCognition, QGIS, GRASS, R Studio, Python and ArcMap. Most of OBIA has been developed around eCognition, while R is an open source environment which is user-friendly and can host the implementation of some segmentation algorithms. In this study, segmentation was done in eCognition and R environments.

The entire study area was divided into forest blocks because of differences in forest structure, and also to reduce image size for faster processing. The blocks were numbered 1, 2, 3, 4, 5 and 6. Five of the blocks are those from which field data were collected in 2016, while block 2 had no recorded field data. A total of three image configurations were segmented; filtered UAV-RGB, unfiltered UAV-RGB, and UAV-Pleiades. Two segmentation algorithms were used to segment the image configurations in two different environments. Multiresolution segmentation was done in eCognition, while SLIC segmentation was done in R.

2.5.1.1. Multiresolution segmentation in eCognition

There are many different segmentation algorithms in eCognition, amongst which multi-resolution is powerful when dealing with very high-resolution images (Belgiu & Drăguţ, 2014). Also, attempts have been made to advance methods for objective identification of optimal segmentation parameters to some degree of automation (Anders, Seijmonsbergen, & Bouten, 2011; Drăguţ, Tiede, & Levick, 2010a; Esch, Thiel, Bock, Roth, & Dech, 2008). Most of these methods have been designed for Multiresolution segmentation, making it more robust and popular (Esch et al., 2008). For these reasons, MR segmentation algorithm was used in this study with the Estimator of Scale Parameter (ESP) tool. The determination of optimal scale parameter for multiresolution segmentation was done using the ESP2 tool. This tool automatically segments each image configuration into three levels, corresponding to levels of homogeneity. In this process, the tool calculates Local Variance of objects for each level (mean standard deviation of objects for each level). The rate of change in local variance per iteration is then plotted against increasing scale value to show the optimum scale value for image segmentation. Figure 2-7 below shows the Local Variance graph for the segmentation of the open forest block in the study area.

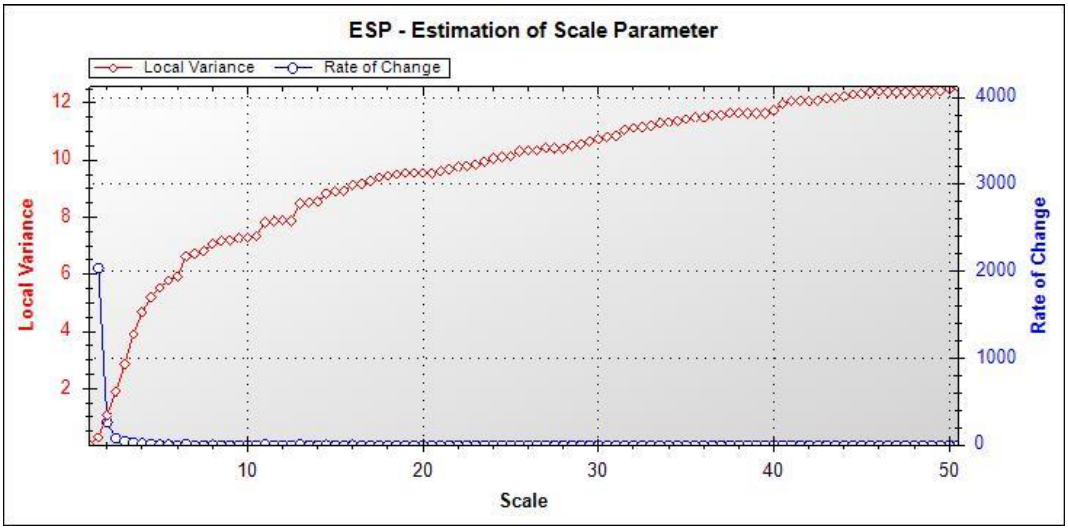

Figure 2-7: Local Variance, Rate of Change versus Scale parameter for optimal image segmentation using ESP2 tool

The red line represents the local variation in the image objects from pixel level, while the blue line represents the rate of change in local contrast as the object size increases, and the vertical dotted grid lines are the optimal scale for each scene. As can be seen from the graph, the local variance jumps high at the start as the size of objects increases due to the high resolution of the image (Drăguţ et al., 2010), While the rate of change is in the opposite direction, slowly because of the scene (forest).

However, default parameters (step sizes for each of the three levels, shape and compactness) in ESP2 tool were inappropriate for segmenting the tree crowns within the forest blocks. Thus, step level sizes were iteratively reduced, and by visual assessment, the combination with the best segmentation levels was selected. Besides setting the shape and compactness parameters, the step level sizes were also varied to obtain proper segmentation. Appendix I shows the different settings that were used to segment the forest blocks under different image configurations. The best segmentation levels for each forest block were exported as shapefile, smoothed polygon for accuracy assessment in ArcMap.

2.5.1.2. SLIC segmentation in R environment

Amongst the machine learning segmentation algorithms that can be implemented in R environment, Simple Linear Iterative Clustering (SLIC) is simple to use and understand, and it adheres to boundaries (Stutz, 2015; Stutz, Hermans, & Leibe, 2016). Also, SLIC improves segmentation performance and is computationally faster and memory efficient. Like Multiresolution in eCognition, SLIC uses Color, brightness, and compactness, to link connected pixels into clusters (Achanta et al., 2012). SLIC is available in GRASS (Kanavath & Metz, 2017), QGIS, Python and R. The implementation of SLIC in GRASS was not possible due to file format compatibility issues. The plugin of SLIC in QGIS is limited to the delineation of parcel boundaries and roads. Python and R environments require scripts, but the implementation of SLIC in R was chosen because of its user friendly scripting language.

SLIC is a gradient-based segmentation algorithm which adopts a k-means clustering approach to efficiently generate equally sized superpixels based on image colour space (Crommelinck et al., 2017). Superpixels are a cluster of connected pixels(comparable to image objects) with similar features like colour, brightness, and texture (Achanta et al., 2012).By k-means clustering, the algorithm initialises some centroids(k-centroids) within an image based on the number of colour clusters in the image as shown in figure 2-7A(Jeevan, 2015). Based on these k-clusters, supper pixels will be assigned to each cluster based on their distances from the centroids. Once assigned, a new centroid(k-mean) will be calculated as the mean of all superpixels belonging to a particular centroid as shown in figure 2-8B.

The difference between the first and adjusted middle is calculated as residual. The number of centroids or k-means determine the amount of equally sized clusters to be generated.

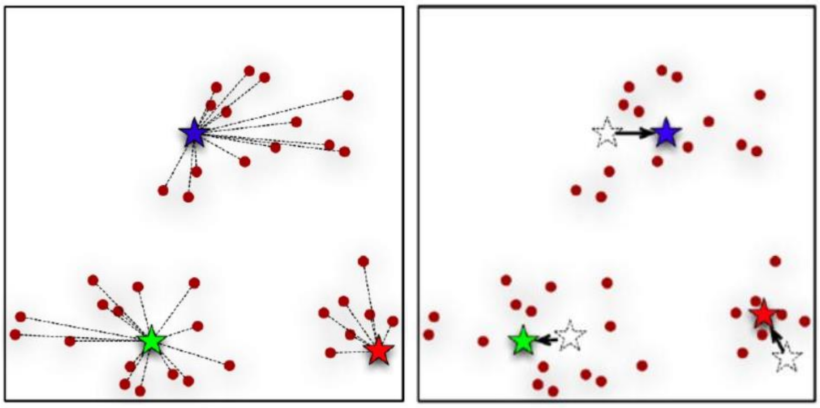

A **B**

Figure 2-8: Illustration of k-mean clustering for the creation of a cluster of superpixels: A shows the initial means, represented by the blue, red and green stars while B shows the re-calculated means and shift of centre from initial mean(white

The algorithm estimates two parameters; the ***k**-parameter which* specifies the number of approximately similarly sized superpixels to be produced, and the compactness parameter **m** which controls the trade-off between superpixels' homogeneity and boundary adherence. SLIC has been applied for the segmentation of diseased tree crowns, and it performed well (Yuan & Hu, 2016).

The images to be segmented were exported from ArcMap as a raster in .jpeg format (unsigned 8bits), compatible with the SLIC script implemented in R version 3.4.2. SLIC segmentation of both image configurations followed the steps as outlined in the R script (Simon, 2017). The detailed script is presented in appendix II. The main steps are shown in figure 2-9 below.

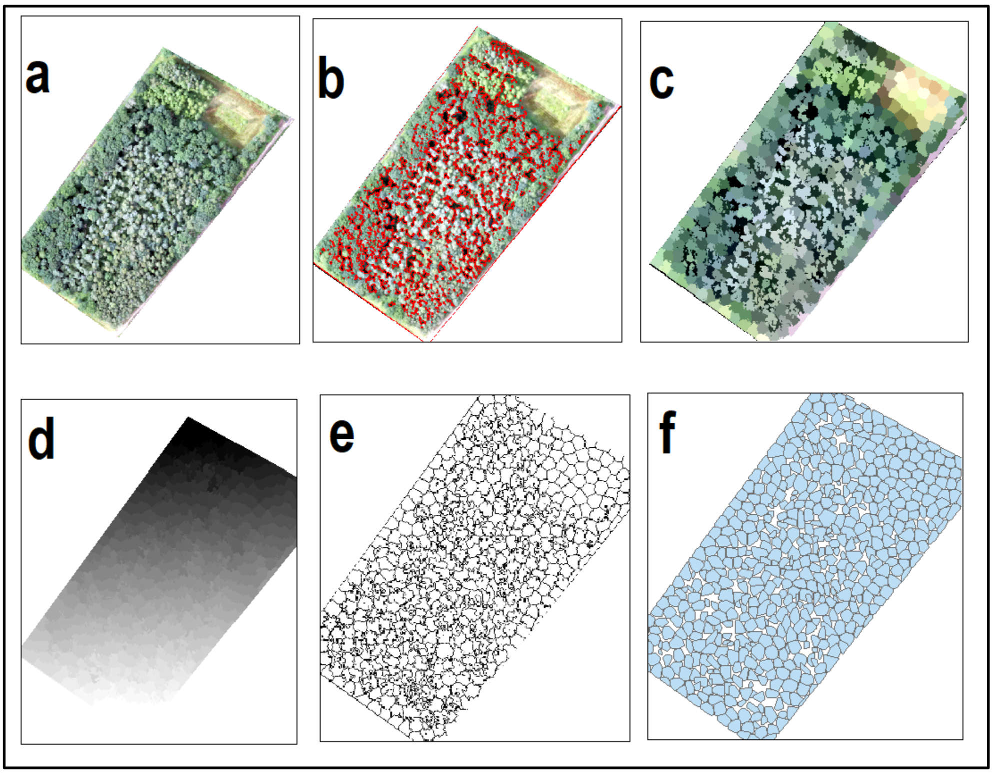

Figure 2-9: Input, and output for the main steps in SLIC segmentation(original image (a), separating shadows from trees (b), RGB converted to CALIEB colour space (c), grey scale representation of colours (d), segmented image (e), post processed segments (f).

The image (**a**) is read and loaded into the R environment. K-means clustering is then performed with two centres. This process separates shadows from tree crowns (**b**). Section two converts the image from RGB to a colour space that indicates RGB values with three axes: L, a, and b. Light and dark along the 'L' axis, red and green along the 'a' axis, and blue and yellow along the 'b' axis. The relative scales of spatial to colour dimensions are left as default, but the ratio of spatial and spectral scales is divided by 10times the compactness value (Simon, 2017), to ensure that the resulting features(supper pixels) have similar scales. Based on the colour space, the grey scale axis is used to create outlines of segments (**d**). Finally, the image is segmented and the layers displayed on the original image(**e**). The layers (**e**) were exported for post-processing in ArcMap. The post-processed output (**f**) was used to assess segmentation accuracy.

Post-processing comprised of geo-referencing with affine polynomial transformation, extracting forest area by the mask, deleting smaller polygons with an area less than one square meter, applying minimum bounding geometry and finally smoothening with 300 as value for smoothing tolerance. The resulting segments were visually assessed before accuracy assessment.

2.5.2. Image Classification

Image classification is the process of assigning landcover classes to specific pixels. It also refers to the process of appointing segmented image objects to particular cover types or species following image segmentation. Classification can be unsupervised, supervised or object based or both. The first two have been very popular and mostly used for pixel-based classification. However, Object-based supervised image classification is in recent times used for the classification of very high-resolution images (Juniati & Arrofiqoh, 2017; Weih & Riggan, 2010). Some classification methods have been used for tree species classification using remote sensing images. Amongst these are Maximum Likelihood (ML), Random Forest (RF), Random Trees (RT) and Support Vector Machines (SVM) classifiers (Adelabu et al., 2013; Carleer & Wolff, 2004; Cho et al., 2010; Lobo, 1997). These supervised classification algorithms can be implemented in eCognition and ArcMap environments. These classifiers, operate using similar principles; use training samples, validation samples and vote of the plurality to finally classify an object into a specific class (eCognition User guide, 2016). The classification environment in eCogniton was not user friendly, with training samples failing to display on screen. Segments were thus exported with feafure values into ArcMap for classification. The use of ArcMap was engineered by its user friendly environment for the implementation of RT, SVM and ML classifiers.

2.5.2.1. Random Trees

Random Trees is a supervised classification algorithm that uses a bagging operation to create some trees (ntree) from a random subset of samples from the training data. In a bagging process, the algorithm generates many subsets (ntrees) from the input training data with replication (can choose one point more than once) and classifies each into the number of classes (mtry) as in the training set. The classification of each subset (tree) is then averaged to get final classification with reduced variance. Random trees are a combination of tree predictors that depends on the values from random subsets sampled independently with the same number of samples in the training set (eCognition User guide, 2016). Each tree is grown autonomously to a maximum size based on a bootstrap sample from the training dataset with the same number of classes, and each node (classification) is split using the best among a subset of "mtry," input variables or classes (Breiman, 2001). The decision to classify elements in the subset of specific classes (mtry) is based on pure samples that are present in the subset. The multiple classification trees then vote by diversity on the correct classification (Lawrence, Wood, & Sheley, 2006). The data that are not found in the trees are classified as out-of-bag (OOB) data. An average of the OOB error rates gives the OOB classification error for each input variable (mtry). The classification is assessed using validation data from the field, and a confusion matrix is generated.

2.5.2.2. Support Vector Machine Classification

A Support Vector Machine (SVM) is a supervised discriminative classifier defined by a separating hyperplane. The hyperplane is a line that separates the training data set into the number of classes, based on training data statistics. From a given training sample data, the algorithm outputs an optimal hyperplane which categorises new examples. It is binary, using two classes (present /absence) of training samples in a multi-dimensional feature space to fit an optimal separating hyperplane. The classifier then maximises the distance between the closest training sample (support vector) and the hyperplane (Burges, 1998; Hsu, Hsu, Chang, & Lin, 2010).

2.5.2.3. Maximum Likelihood Classification

Maximum Likelihood is a supervised classifier popularly used in remote sensing image classification. It considers the variance and covariance of class signatures to assign each object or pixel to a class (Sisodia, Tiwari, & Kumar, 2014). The algorithm uses the basis that the mean and covariance of each class in the training sample is normally distributed, to fit models describing each class (Bakx et al., 2013; Hogland, Billor, & Anderson, 2013). Based on the fitted models from the training sample, the class of new objects or pixels is determined by calculating which model is more likely to describe the object. The model with the maximum likelihood is selected. The Maximum likelihood classifier is robust, but also biased to small sample size (Adelabu et al., 2013).

Forest block 4 was selected for classification because it had the highest mean segmentation accuracy from all the image blocks. Also, this block had a reasonable number of trees for three of the primary species in the study area (Beech, Birch and Scots pine). Maximum Likelihood, Random trees and Support Vector Machines classifiers, were implemented in ArcMap to classify the segments. The segmented layers were exported from eCognition with eight features in its attribute table for UAV-

RGB and ten features for UAV-Pleiades. These features represent segment statistics that would be used for classification in ArcMap. The Random trees, Support vector machines and Maximum likelihood classifiers in ArcMap require segmented raster as input. For this reason, each feature was extracted by conversion to a segmented raster layer. Features were normalised to avoid attributes with numerically higher ranges from dominating those with numerically lower ranges during classification (Hsu et al., 2010). Linearizing each feature also avoids numerical difficulties during calculations of segment statistics by the algorithm. Each feature was normalised to have values between 0 and 1, using raster calculator with the expression below.

Normalized feature = (feature value - minimum)/(maximum value -minimum value)

Normalisation also gave each feature the characteristic normal distribution which makes training and classification faster (Hua et al., 2006; Kuzmin, Korhonen, Manninen, & Maltamo, 2016). All normalised features were layer stacked to create a segmented raster layer (a requirement for implementing the classification algorithms in ArcMap), with the number of bands corresponding to the number of features used. Amongst the layer stacked features, four were selected for classification of UAV-RGB (mean values of Red, Green, Blue, brightness and standard deviation) while eight were selected for classification of UAV-Pleiades (1=Red, 2=Green, 3=Blue, 4=NIR, 5=Mean brightness, 6=compactness, 7=Roundness, 8=Standard deviation)

Two sets of training and reference data were digitised in ArcMap based on field data. Training samples were randomly selected, but the digitising was done such that each sample is a pure representation of the class it represents. Five classes were used; Birch, Beech, Scots pine, water and shadow. From the UAV-RGB image, 30, 21, 20,19 and 14 samples of Scots pine, Birch, water, Beech and Shadow were collected respectively. On the other hand, 41, 28, 20, 4 and 29 samples of Scots pine, Birch, water, Beech and Shadow were respectively collected from the UAV-Pleiades image. Samples for each class were merged for each image configuration to obtain a value for each class. All classifiers used the same training and validation data set containing five classes (Birch, Beech, Scots pine, water and shadow) for the same image configuration. Class separability of the training samples was done using the mean layer statistics. As can be seen in figure 2-10, the plotted ban statistics show that the four classes can be better separated in bands (layers) 1 and 2 for the UAV-RGB layer. Within band two, there is a possible mixing of Beech and Scots pine.

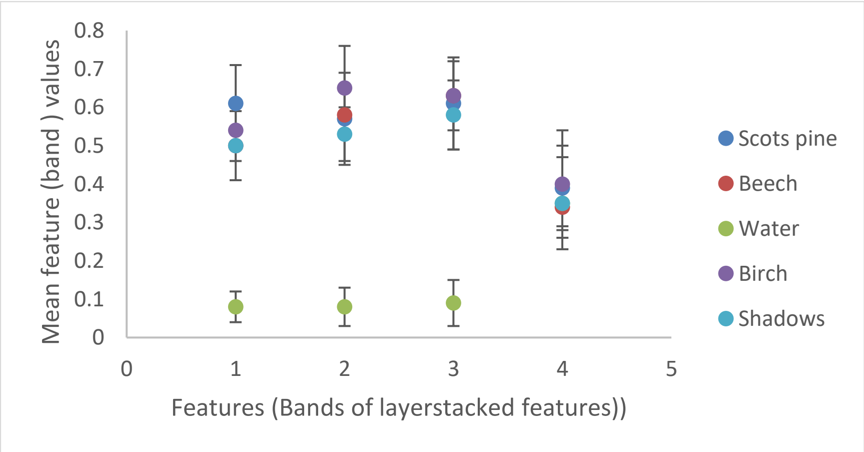

Figure 2-10: Comparing class separability amongst the layers in the UAV-RGB layer stack raster (1=Red, 2=Green, 3=Blue, 4=Mean brightness, =Standard deviation)

On the other hand, the four classes are separated into bands 2, 3, 4 and 5 for the UAV-Pleiades image as shown in figure 2-11. In bands 2 and 3 and 5, there is a possible mixture of Birch and Scots pine, while in band 4, all classes are well separated.

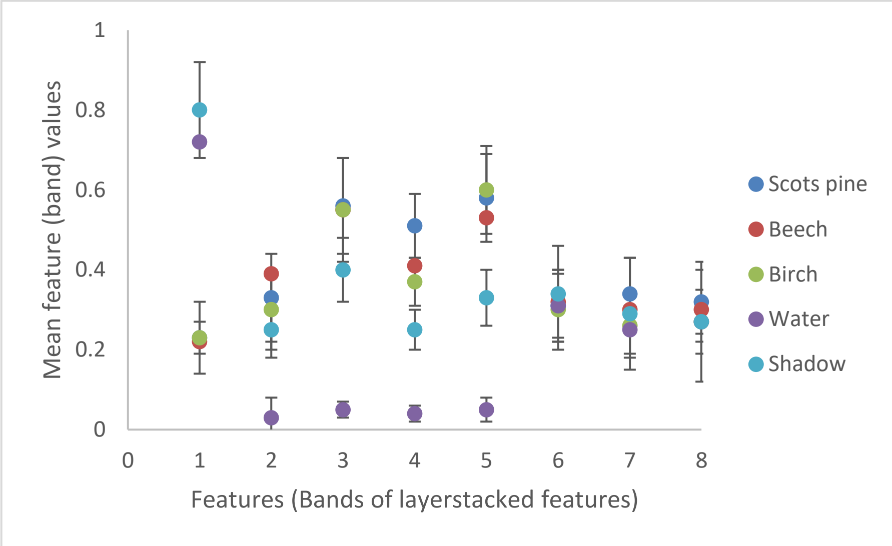

Figure 2-11: Comparing class separability between the different image layers (bands) for UAV-Pleiades segmented raster layer. (1=Red, 2=Green, 3=Blue, 4=NIR, 5=Mean brightness, 6=compactness, 7=Roundness, 8=Standard deviation)

With the training data from each image configuration, all three classifiers were trained to generate respective classifier definition files which were later used for classification. In the case of Random trees classifier, the number of trees or subset was set to 500 (number of subsets created, classified and results averaged to get final classification), with a maximum number of samples and sample depth left as default. For Support Vector Machines, the number of subset per class was set at 500. This number refers to the number of subsets that need to be classified and averaged to get the final classification. These settings were chosen after some iterations.

The detailed segment statistics represented by the classified segmented raster files were converted to shapefile. A spatial join between the classified shapefile and the automatically segmented layer(from eCognition) was performed. The segments from eCognition were used as a target while the classified shapefile was used as a joint feature. In this process, the class values corresponding to cover type were transferred to the corresponding segments from eCognition. The attribute table of the resulting product was edited to add species name, following the grid code values. The layers were then visualised with cover type field as classified segments.

2.6. Above ground biomass and carbon stock Estimation

This process made use of allometric equations that relates DBH and CPA, and DBH and AGB. A review of common mistakes with the use of allometric equations recommends that simpler models with fewer parameters and no polynomial terms, are relatively better because: they are easier to be tested in replication and cross-validation tests. Also, because such models suffer less from the influence of statistics and collinearity, and parameters are easier to interpret biologically (Sileshi, 2014). Jose (2009) established the relationship between biomass and DBH for some temperate tree species in the form $\mathbf{y_{ou} = a(DBH)^b}$ with '**a**' and '**b**' significantly different from zero ($p < 0.01$). The nature and strength of the predicted relationship for each species were assessed by interpreting the signs of the regression coefficients and the magnitude of the R^2 and adjusted R^2. Appropriate species-specific allometric equations relating biomass (AGB) with DBH for each species were sourced from existing literature and GlobAllomeTree (2017) and used to estimate aboveground biomass and carbon for each tree species using field derived DBH. Table 2-3 below shows the set of selected allometric equations for each species. The selection process considered sample size, location of study, R^2 value and year of publication

Table 2-3: Selected species allometric equations for eight tree species in the study area.

Species	Equation	Sample size	R2	Location	Source
Fagus sylvatica (Beech)	Biomass=0.0798*(DBH)^2.601	38	0.99	netherlands	Bartelink(1997)
Pinus sylvestris (Scots pine)	log10 Biomass=-1.89+2.74*LOG10((DBH))	20	0.99	Finland	Drexhage and Colin (2001).
Quercus petraea(Oak)	log10 Biomass=-1.56+2.44*LOG10((DBH))	71	0.94	France	Drexhage and Colin (2001)
Pseudotsuga menziesii (Douglas fir)	Biomass=-1.62+2.41*LOG((DBH))	23	1	netherlands	Bartelink, H. H. 1996
Betula(Birch)	Biomass=0.1993*(DBH)^2.2491	13	0.99	uk	Hughes(1971)
European hornbeam	log Biomass=-5.777+2.481*LOG((DBH))	15	0.71	Poland	Oleksyn et al.(1999)
Mountain ash	Biomass=0.1245*(DBH)^2.3585	7	0.97	Bavaria	Dietrich et al.(2002)
Alder(alnus)	Biomass=0.00079*(DBH)^2.28546	n/a	0.99	Sweden	Johansson(2000).

Source: www.GlobeAllomeTree.org (2017)

The excel file containing measurements of location; field measured DBH and species information was converted to a shapefile in ArcMap. The shapefile was overlaid on the orthophoto, and corresponding tree crowns were manually digitised at a constant scale of 1:400. A spatial join between the trees shapefile and manually digitised crowns transferred DBH values to corresponding crowns of tree species. The resulting shapefile thus contained DBH, species and similar CPA information in its attribute table. The trees were sorted in Microsoft office excel based on species, and correlation analysis was done to investigate the relationship between CPA and DBH, as well as its significance. A regression analysis was then used to quantify any existing relation between DBH and CPA. Based on the statistical significance of the modelled relationship, appropriated models were chosen for each species.

The chosen models were used to predict AGB of the automatically segmented and classified tree crown projection areas. The segments of the selected species were selected and exported as shapefile. The areas of the exported segments were calculated and exported to Microsoft Office Excel 2016. The DBH of classified crowns for each tree was modelled and used to estimate AGB. This procedure was done for the best classification from each image configuration. The modelled AGB was compared with field-derived AGB to infer a statistical difference. A conversion factor of 0.47AGB equals carbon was used to translate biomass to carbon estimates in kg (IPCC, 2006).

2.7. Data analysis

Data analysis made use of software packages like Pix4D (UAV image processing), eCognition and R-studio (segmentation) and ArcMap (accuracy assessments and visualization).

2.7.1. Optimal flight pattern

The quality of the resulting point clouds was assessed using the quality report from pix4D. The geolocation details; mean and median point density (2D and 3D key points) and root mean square error of GCPs and Check Points (CPs) were assessed to judge the quality of point cloud and orthophoto from the two flight patterns. 2D points represent x and y location of features that have been identified, described and matched on two or more images (Nex & Remondino, 2014). These points are used for image matching during the photogrammetric process of image orientation. 3D points represent x, y, and z location of points in space determined through epipolar geometry, and used for relative orientation of the images. The GCPs are the x,y and z location of points collected using RTK/GNSS, and used to give the images coordinates on the ground (absolute orientation). The differences between the x,y and z locations of images and the GCPs is used to estimate the RMSE (Remondino, Nocerino, Toschi, & Menna, 2017). A t-test was performed, comparing the errors in GCP location between parallel and perpendicular flight patterns. The relationship between the flight height above the tree canopy, the percentage of calibrated images and RMSE of GCPs and CPs were assessed to determine the optimal flight height of the DJ Phantom 4 over forest stands. The root means square orientation errors were compared for flight patterns, and visualised using tables and graphs. Tables and graphs were also plotted to recognise any relationship between flight height and the number of calibrated images, flight height and RMSE of the GCPs.

2.7.2. Segmentation accuracy assessment

Evaluating the quality of segmentation is essential for the validation of the OBIA process. Segmentation quality can be assessed using analytical, empirical goodness of fit, and empirical discrepancy methods. Analytical methods directly assess the performance of segmentation algorithm based on principle, requirement, and complexities (Zhang, 1996). The empirical goodness of fit methods judges the quality of segmented images as a proxy for the performance of the algorithm. Empirical discrepancy methods use the difference between the reference (manually delineated tree crowns) and segmented crowns, to judge the algorithm performance. A review of image segmentation evaluation methods reveals that empirical discrepancy methods are better because they try to capture the application throughout the discrepancy measures (Zhang, 1996).

The best way to measure segmentation accuracy depends on the consequences of any segmentation error. In this study, segmentation is done to estimate tree Crown Projection Area, to be used as input in species-specific allometric equations for AGB and carbon estimation. The consequence of segmentation error is either an overestimation or underestimation of CPA and thus AGB and carbon of tree species. For this reason, Segmentation accuracy was assessed using area estimation techniques (Möller et al., 2007), in a three-step procedure according to Clinton, Holt, Yan, & Gong (2010) and as shown in the equations below.

Over segmentation = 1- (area(ADi ∩ ARi)/area(ADi)…………………………equation 1
Under segmentation = 1- (area(ADi ∩ ARi)/area(ARi)…………………..……equation 2
Total detected error = $\sqrt{((\text{Overs segmentation}^2 + \text{Under segmentation}^2)/2)}$….equation 3
Where,
ADi = Area of detected objects, that are in a one-to-one spatial relationship with reference polygons.
ARi = Area of reference polygons
Area(ADi ∩ ARi) = Area of reference polygons that have been correctly segmented.

The accuracy assessment made use of manually digitised polygons obtained for each block from the filtered and resampled orthophoto. 54 polygons were delineated for block 3, 52 for block 5, 123 for block 1, 70 for block 6 and 51 for block 4. A spatial join between reference polygons and the segmented layer was done in ArcMap to identify segmented polygons in a spatial relationship with the reference polygons based on a join count greater than zero. Selection by attribute of polygons from the output based on join count different from zero was made and the results exported as a layer. The reference polygons were used as target features while the segmented layer was joined feature in a spatial join operation. Upon getting the layer of segmented polygons in spatial contact with the reference layer, an intersection was performed with the reference polygon layer to get under segmented and over the segmented area. A field was added to the attribute table of the intersection output and area (ADi ∩ ARi) was obtained by calculating geometry. The area of reference polygon layer represents "ARi" in the equation above while the area of spatial join output represents "ADi". With ADi, ARi, and area (ADi ∩ ARi), over-segmentation, under segmentation and total detected error were calculated.

Three blocks were selected; to investigate a significant difference in the accuracy, of segmenting UAV-RGB and UAV-Pleiades image configurations. Using the same reference polygon layer for each block, spatial join, and the intersection was performed with the respective segmented layers. The resulting area from the outputs (intersection) was extracted for corresponding segments and a two-tailed t-test performed at 95% confidence level.

2.7.3. Classification accuracy assessment

Accuracy assessment is a comparison between a detailed map and some reference information assumed to be correct, following acceptable rules consistently (Strahler et al., 2006). The accuracy of a classification can be judged using accuracy parameters like overall accuracy, per-class accuracy, producer and consumer accuracies. The rules to consistently observe in the process include; the choice of quality index appropriate given the purpose of each study, sampling unit, strategy and sample size (D. Lu & Weng, 2007; Strahler et al., 2006).In this study, the classification was done on a segmented layer with the purpose of accurately linking segments (CPA) to tree species for the modelling of DBH and AGB at the species-specific level. Based on the defined goal, sampling units were chosen as polygons (CPA), while sample size was proportional. Since the segments (CPA) represents a spatial entity that needs to be given identity in the classification process, the area was chosen as the most important index for accuracy (Radoux & Bogaert, 2017).

The detailed raster images were each reclassified and converted to polygons. Through a spatial query between the segmented layer and the reference polygon layer, a subset of segmented polygons was exported as test polygon layer. In a spatial join between reference polygons layer and the test polygons layer, class values were transferred from reference to test polygons. A total of 20 samples were taken for Scots pine (692.73m^2), Birch (1604.29m^2) and water (3087m^2), while 10 and 15 samples were taken for Beech (743.48m^2) and Shadow (4103.91m^2) respectively. An intersection between final test polygons layer and the reclassified polygons was performed, and the output used to extract correctly and wrongly classified area for each tree species. A selection query by attribute {gridecode=1 (2,3…n) AND Class=1 (2,3..n)} was performed and the area of each species correctly and wrongly classified was calculated. The values were input into the confusion matrix for classification accuracy assessment.

A selection by location query was performed between a reference layer and each of the classified layers to extract samples from each layer for comparison. A spatial joint was done with the three layers; reference, and exported test segments from each classified layer. The class values from corresponding segments in both classified layers were judged against those from the reference layer, and a two by two confusion matrix was created. A statistical test was performed to infer a significant difference in the classification of different classifiers using the McNemar test. This test is based on chi-square (z^2) statistics computed from the two error matrices given as

$$\mathbf{z^2 = (f_{12} - f_{21})^2 / (f_{12} + f_{21})},$$

Where f_{12} = number of cases wrongly classified by classifier one but correctly classified by classifier 2, and f_{21} = number of cases correctly classified by classifier one but wrongly classified by classifier 2 (Manandhar, Odeh, & Ancev, 2009). From the McNemar test, if the z-score is greater than 1.96 at 95% confidence level, then the differences in classification results are statistically significant.

2.7.4. Comparing DBH, AGB and Carbon

CPA values were extracted and used to predict DBH of the primary species using different models. The models were compared using their RMSE value and coefficient of determination (R^2 value), and the best models were selected. Using the best models, and CPA samples from the classified segments, DBH and AGB were predicted and compared with field-derived DBH and AGB using a t-test for normally distributed set, and Man Whitney U test for non-normally distributed set, to infer any significant difference.

3. RESULTS

3.1. Descriptive analysis of field data

Descriptive statistics were performed to understand the nature of field data. The results are presented below in graphs and tables.

3.1.1. Species occurrence

The pattern, spread and characteristics of field-derived data were described using descriptive statistics. The bar chart below(figure 3-1) shows the occurrence of tree species within the Amtsvenn area. From the existing data, a total of 391 trees were extracted. From the 391 trees, the dominant species are Fir (36%), Birch (19%), Oak (17%) and Scots pine (13%). The other tree species have been recorded in less than 10% of the samples.

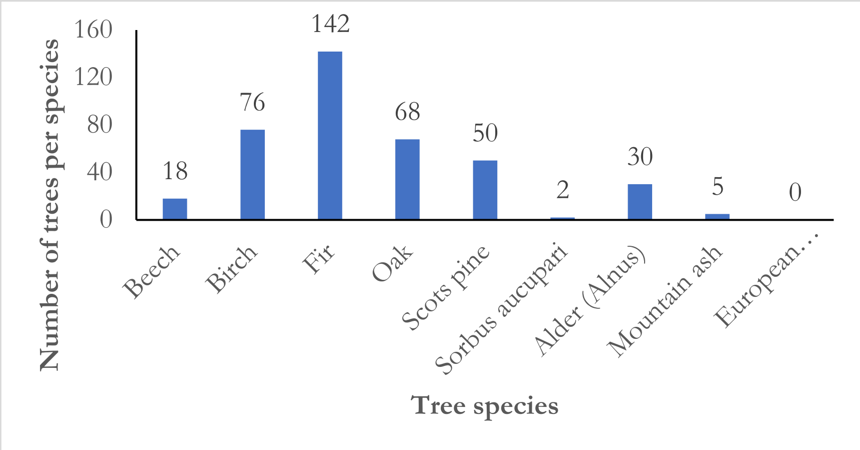

Figure 3-1: Numbers of trees per species recorded within the Amtsvenn area

3.1.2. Diameter at Breast Height

The diameter at breast height for tree species from all the blocks was summarised and described as shown in table 3-1 below. Beech trees had the highest mean DBH followed by Scots pine and Oak. The DBH of all species showed positive skewness from the mean. Because trees with DBH < 10cm were not considered

Table 3-1: Summary statistics for Field measured DBH

Tree species/ (count)	**Mean**	**Std. Error**	**Std. Dev**	**Kurtosis**	**Skewness**	**Skewness z value**	**Kurtosis z-value**
Beech/(18)	33.09	4.2	17.8	2.1	1.5	0.36	0.5
Birch/(149)	19.96	0.88	10.7	**24.8**	**3.7**	**4.2**	**28.31**
Fir/(69)	22.95	0.93	7.7	-0.9	0.3	0.33	-0.96
Oak/(68)	29.75	1.59	13.1	2.1	1.2	0.78	1.34
Scots pine/(50)	34.86	1.19	8.4	1.1	0.9	0.79	0.89
Sorbus aucupari/(2)	12.5	1.7	2.4	n/a	n/a	n/a	n/a
Alder alnus/(30)	15.55	1.87	10.2	**5.4**	**2.5**	1.32	**2.91**
Mountain ash/(5)	13.06	0.85	1.9	**-2.2**	0.1	0.15	**-2.6**
European hornbeam/(17)	20.69	1.58	6.5	0	0.4	0.28	-0.03

DBH measurements for *Alder alnus* and Birch are significantly skewed as shown by their respective skewness z-values of 4.2 and 2.5 respectively. Mountain ash has a sample size too small to be considered for analysis.

The boxplot in figure 3-2 below shows the outliers in the measurements for Beech, Birch, Oak, and Alder. Most of the Oak, Scots pine, Douglas fir and European hornbeam trees had DBH greater than 20cm, while for the other species, most trees had DBH below 20cm. Some of these presumed outliers could be the very few large trees present in the field. The number of trees recorded for *Sorbus aucupari* and *Mountain ash* were lower than 10, probably because they are rare in the study area. These two species were eliminated from further analysis.

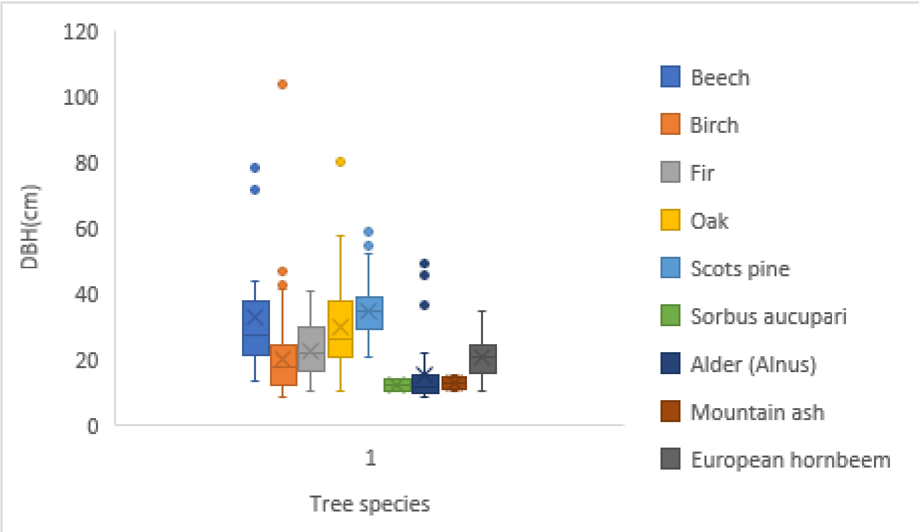

Figure 3-2: Distribution of Field DBH within and between tree species(raw data)

The measured DBH for all species was transformed with the log function, followed by outlier removal. The identification of outliers was done using the 2.2 threshold as described in Hoaglin, Iglewicz, & Tukey (1986). Based on the 2.2 threshold, the upper and lower boundaries were calculated, and outliers were identified. Figure 3-3 shows the data distribution after outlier removal.

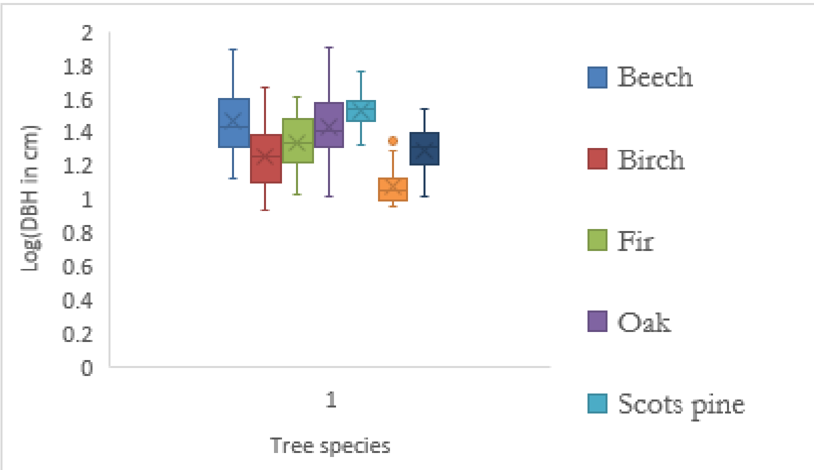

Figure 3-3: Distribution of Field DBH of tree species after Log transformation

This procedure reduced the number of data points to be deleted as outliers and preserves sample size. After transformation, all the data was normally distributed. However, Alder species showed one outlier.

3.1.3. Estimating Field AGB

Allometric equations relating aboveground biomass and DBH for the main tree species were sourced from Glob allometry (GlobAllomeTree, 2017). The selection process for the most suitable equation considered sample size, the location of study and coefficient of determination (R^2 value). Figure 3-4 below shows the mean and median field AGB for tree species within the study area. Beech trees show the highest Kg of AGB per tree. The mean and median AGB for Beech species is 436, with most trees having AGB above the mean. Birch species also have mean AGB of 129.4 with most trees above the mean value. Scots pine shows equal distribution of AGB on both sides of the mean.

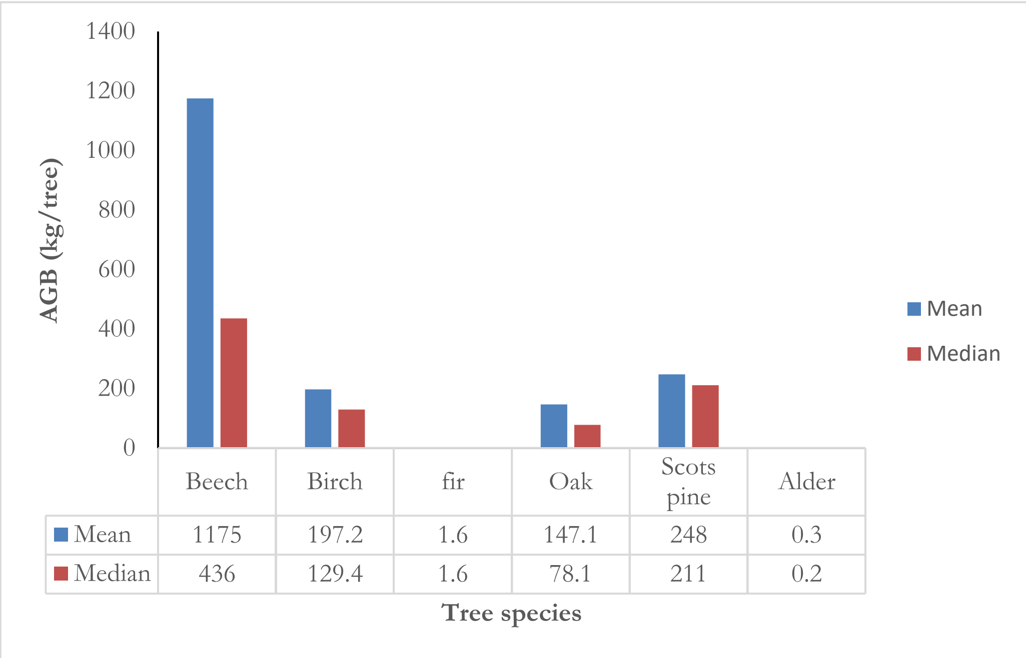

Figure 3-4: Mean and Median AGB of tree species: possible influence of outliers on AGB estimation

As can be seen in figure 3-4 above, *Alder sp* and *Douglas fir* showed the lowest mean AGB among the trees sampled in the Amtsvenn area. A ranking of these species based on contribution to above-ground biomass reveals that Beech, Scots pine and Birch are the three dominant species contributing to the biomass of the area.

3.2. Optimal flight pattern

The parallel and perpendicular flight patterns captured 346 and 359 images respectively over a forest block of 6.7ha. The geolocation details, accuracy and bundle block adjustment details are presented below. The geolocation details looks at the reprojection errors in x, y and z values by comparing the positions of points on the image to their true position on ground recorded by the differential GNSS.

3.2.1. Geolocation details

As presented in table 3-2, the geolocation details reveal errors in the x, y and z directions. The errors were all low, in the range of 1.2 and 2.3cm. The mean errors for the parallel flight pattern were numerically lower than those of the perpendicular or grid pattern, especially in the z-axis (height).The RMSE of parallel flight pattern was also numerically lower than corresponding perpendicular RMSE in the x and z-axis.

Table 3-2: Comparing geolocation details for parallel and perpendicular flight patterns.

	Geolocation details in Perpendicular pattern			Geolocation details in Parallel pattern		
GCP Name	Error X [m]	Error Y [m]	Error Z [m]	Error X [m]	Error Y [m]	Error Z [m]
GPS0001 (3D)	-0.01	-0.015	0.004	0.007	-0.025	-0.001
GPS0002 (3D)	0.017	-0.004	-0.018	-0.02	0.024	-0.002
GPS0003 (3D)	-0.031	0.043	0.029	0.017	0.001	0
GPS0004 (3D)	0.023	-0.025	-0.015	-41.757	6.512	-0.849
GPS0005 (3D)	0	0	0	0	0	0
Mean [m]	-0.006	0.006	0.004	-0.004	-0.001	-0.001
Sigma [m]	0.017	0.022	0.017	0.011	0.020	0.001
RMS Error [m]	0.018	0.023	0.017	0.012	0.020	0.001
n	5	5	5	5	5	5

As can be seen in figure xxx below, the reduction in RMSE is higher in the z axis for both flight pattern. However, the reduction is more in the case of the parallel flight pattern compared to the perpendicular flight pattern.

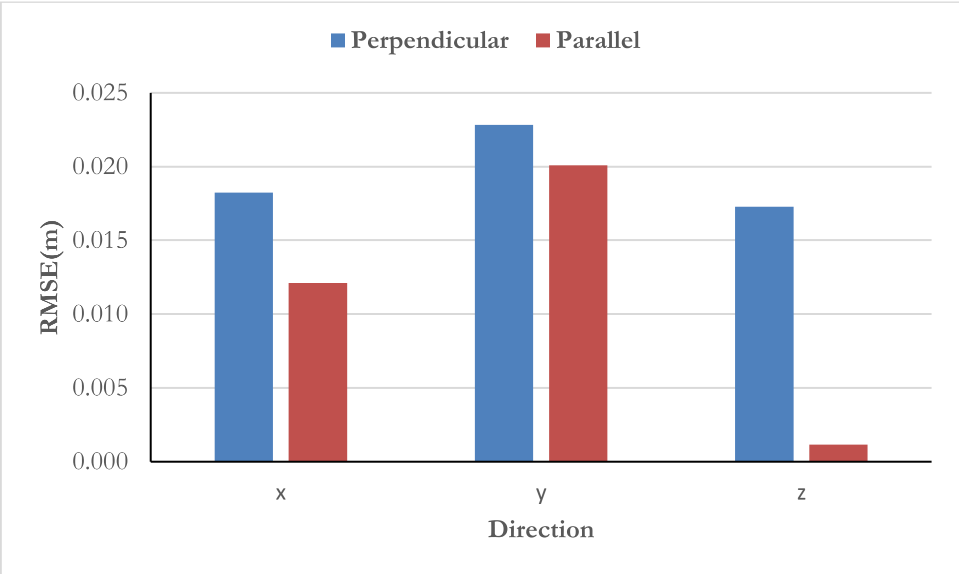

Figure 3-5: A comparison of RMSE resulting from parallel and perpendicular flight patterns

3.2.2. Bundle block Adjustment

The bundle block adjustment details reveal that the perpendicular flight pattern observed 807 thousand 2D and 366 thousand 3D points less than the parallel flight pattern. However, this difference could be due to the presences of some uncalibrated images and not necessarily due to flight pattern. Table 3-4 below shows the results.

Table 3-3: Comparing the number of 2D and 3D points from two flight patterns

	perpendicular pattern	Parallel pattern
# of 2D Key point	1139639	1946676
# of 3D key points	475734	842211
Mean Reprojection Error [pixels]	0.279	0.189

As can be seen in figure 3-6 below, both flight patterns suffer from some uncalibrated images represented in red dots. Also, in the orthophotos (appendix III), there are visible deformations in areas of uncalibrated images and along the boundaries. The red dots are uncalibrated images, while the blue dots are initial positions of images, and the green dots are computed positions of images.

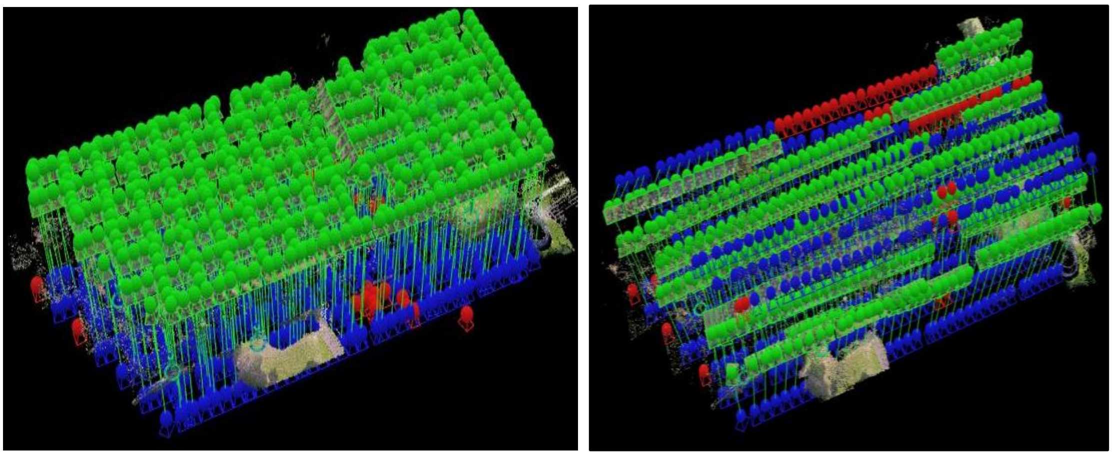

Perpendicular flight pattern **Parallel flight pattern**

Figure 3-6: Image calibration for parallel and perpendicular flight patterns (Red dots are uncalibrated images while Blue dots are initial position of images, and the green dots are computed positions of images)

Figure 3-7 below is a visualization of the resulting orthophoto from the two flight patterns. Image A is the product from processing a single flight at 45m, while image **B** and **C** comes from the processing images from the parallel and perpendicular flight patterns respectively. As can be seen in the figure, the orthophoto from the single and parallel flights show more deformations compared to the orthophoto from the perpendicular flights.

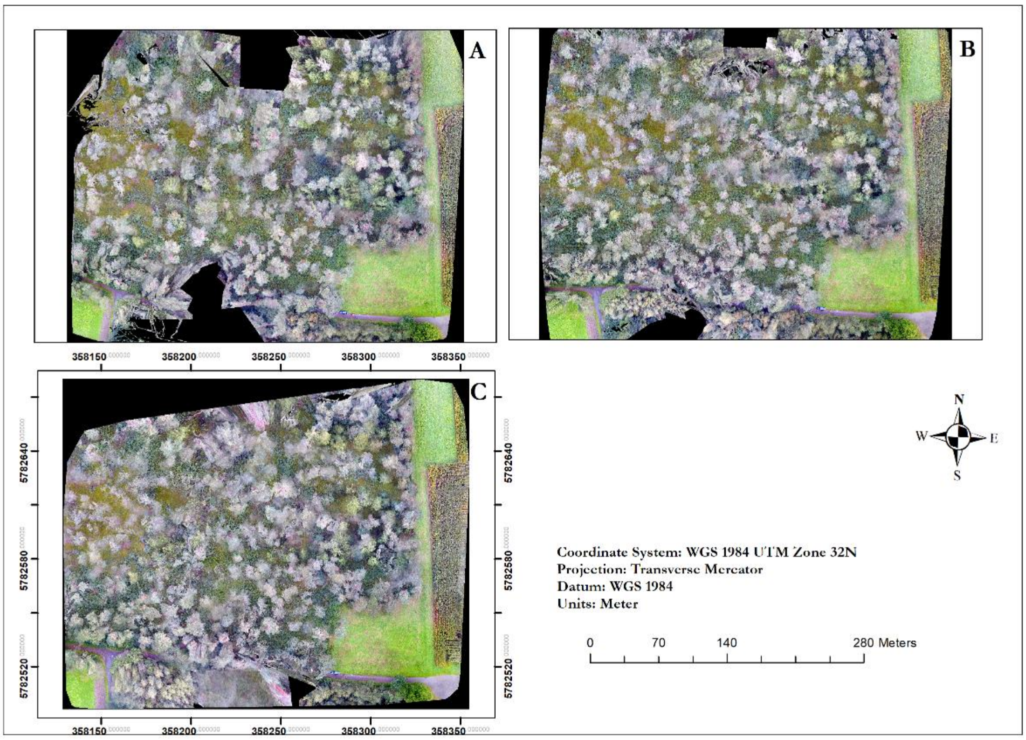

Figure 3-7: Visual comparison of the orthophotos resulting from single flight(A, at 45m height), parallel flight pattern (B, at 40 and 45m height) and perpendicular flight pattern (C, at 40 and 45mheight).

3.2.3. Effect of flight height above canopy on calibration of images

There is a pattern between flight height above tree canopy and the percentage of calibrated images. Table 3-5 below shows that increase in the flight height above tree canopy increases the % of image calibration. However, increase in flight height above tree canopy also increases the RMSE of georeferencing.

Table 3-4: Relationship between flight height above trees percentage of image calibration

Flight height (m)	Flight height above tree canopy	Orthophoto resolution (cm)	Average ground sampling distance (cm)	Geo-referencing Mean RMSE (m)	% of calibrated images
60	40	2.5	2.48	0.014	81
80	60	3.2	3.22	0.021	88
100	80	4	4.07	0.028	100
120	100	4.9	4.93	0.044	100

In table 3-6, increase in the flight height above tree canopy is accompanied by growth in the mean and median number of tie points extracted per image. However, this increase comes at the expense of accuracy. The geolocation error increases with increasing flight height as shown by the RMSE.

Table 3-5: Comparing variations in flight height above tree canopy (m) to root mean square error(m), mean and median tie points recorded per image and mean point density.

Flight height above tree canopy (m)	Mean key point density	Median of points matched per image	RMSE (m)
40	17439	15049.9	0.014
60	15191	15069.2	0.021
80	13324	10353.1	0.028
100	11933	9606.36	0.044

As can be seen in figure 3-8 below, increase in flight height above tree canopy is accompanied by an increase in the RMSE on GCPs. The increase in RMSE is more pronounced in the z-axis (height), compared to the x and y directions.

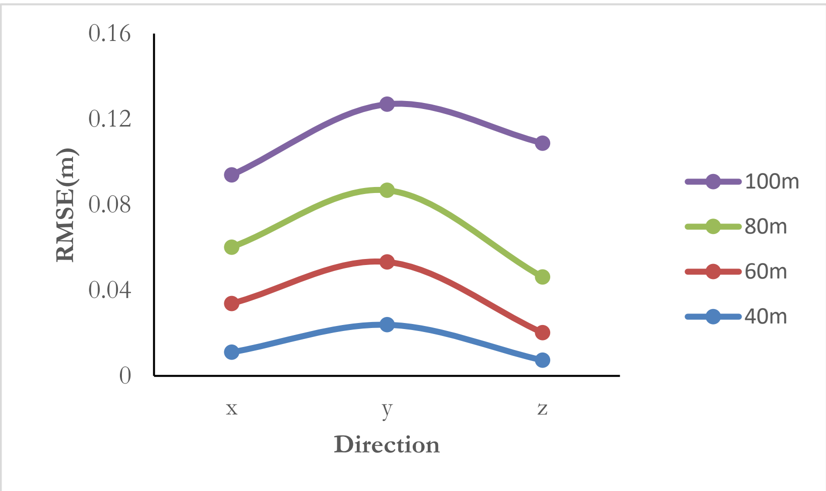

Figure 3-8: Influence of Flight height above tree canopy on image geolocation error (variation in x,y,z errors with flight height) using four flights at 40m, 60m, 80m and 100m above tree canopy (mean tree height is 20m).

3.3. Image Segmentation

The second research question focused on the accuracy of segmenting UAV-RGB and UAV-Pleiades using the multiresolution algorithm in eCognition and SLIC algorithm in R-studio. The question investigates the effect of filtering on segmentation accuracy of UAV-RGB. It also compares the segmentation accuracy of UAV-RGB, UAV-Pleiades, and the performance of SLIC and multiresolution segmentations. In eCognition, multiresolution segmentation made use of the ESP 2 tool. The results are presented below

3.3.1. Multiresolution segmentation of filtered and unfiltered UAV-RGB images

The three levels of segmentation for each block were visually assessed and those approved were quantitatively evaluated. Visual assessment was done by comparing the sizes of the segments in each level to the tree crown sizes in the original image. In the case of Filtered and unfiltered UAV-RGB images, segments of block 3 show a few trees grouped in one segment (figure 3-9 below). The segmentation of block 1 was visually similar for both image configurations. The Segments that were visually approved for quantitative assessment are visualised in figure 3-8 below.

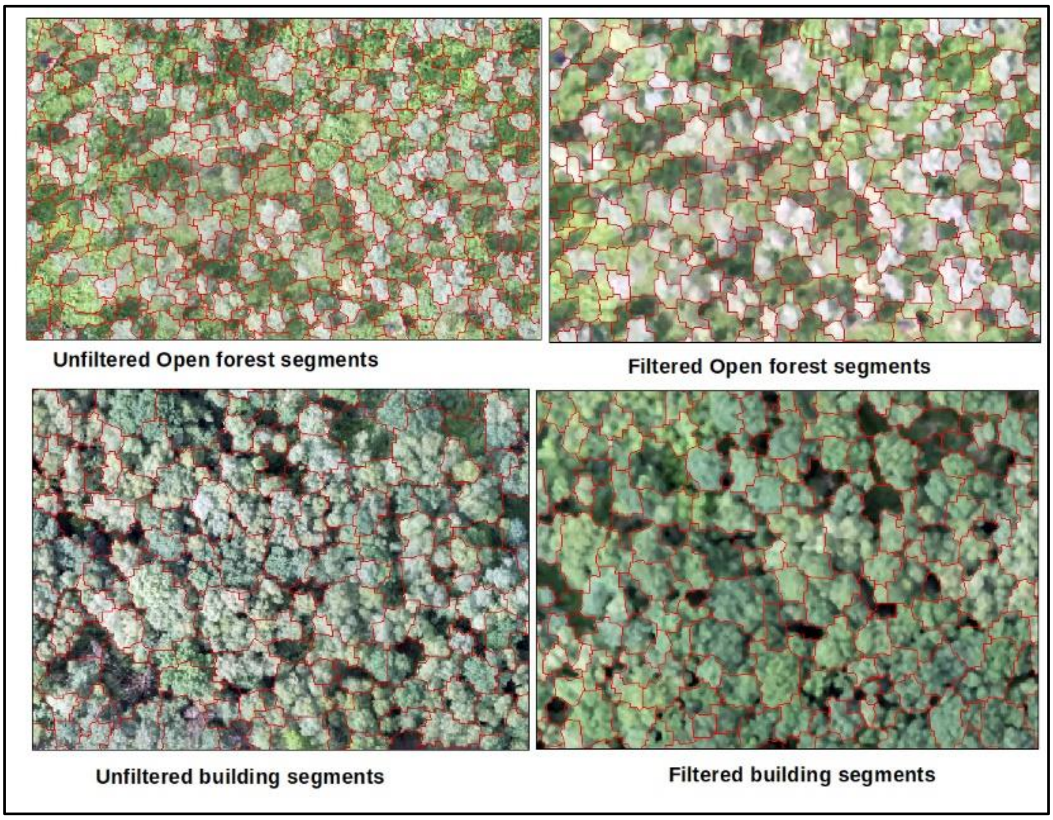

Figure 3-9: Visualising selected levels of segments from filtered and unfiltered UAV-RGB images for quantitative assessment (block 1-open forest and block 3-forest close to building).

Segmentation accuracies of filtered and unfiltered UAV-RGB images show that accuracy for each forest block varied across the image configurations. As can be seen in table 3-7, Filtered UAV-RGB image has highest accuracy in block 5 (84.8%), dense mixed forest with large tree crowns occupying almost same vertical space, and lowest(78.2%) in block 4, which is a dense mixed forest with intermingled tree crowns in two canopy levels. On the other hand, the unfiltered UAV-RGB image configuration has highest accuracy in block 4 block (85.1%) and lowest in block 5 (54.6%). The combined accuracy of segmenting five forest blocks is 73.1% for unfiltered UAV-RGB and 82.1% for the filtered UAV-RGB, The 9% difference could mean that filtering enhanced the segmentation accuracy.

Table 3-6: Segmentation accuracy of Filtered and unfiltered UAV-RGB image configurations using five forest blocks

Unfiltered UAV-RGB					
	Block 4	**Block 6**	**Block 1**	**Block 5**	**Block 3**
Reference area (ARi)	1104.83	4083.41	1622.88	1860.92	4175.35
segmented area (ADi)	1401.12	2892.15	2423.52	1115.15	3190.68
Intersection (ADi ∩ ARi)	1104.83	4083.41	1622.88	1830.22	4175.35
Over segmentation	0.21	-0.41	0.33	-0.64	-0.31
Under segmentation	0.00	0.00	0.00	0.02	0.00
Total detected error (Dij)	0.15	0.29	0.23	0.45	0.22
Accuracy	85.05	70.87	76.64	54.64	78.18
Filtered UAV-RGB					
Reference area (ARi)	1789.03	5293.69	1608.56	2994.60	2876.43
segmented area (ADi)	2586.60	4169.79	2065.23	2464.83	2121.26
Intersection (ADi ∩ ARi)	1789.03	5293.69	1608.56	2994.60	2143.55
Over segmentation	0.31	-0.27	0.22	-0.21	-0.01
Under segmentation	0.00	0.00	0.00	0.00	0.25
Total detected error (Dij)	0.22	0.19	0.16	0.15	0.18
Accuracy	78.20	80.94	84.36	84.80	81.97

3.3.2. Multiresolution segmentation of filtered UAV-RGB and UAV-Pleiades images using five forest blocks.

As shown in figure 3-10 below, the segmentation results of filtered blocks 6 (dense mixed forest with large tree crowns) and 5 (dense mixed forest with closed canopy) show some cases of over and under segmentation. However, a quantitative assessment is presented below.

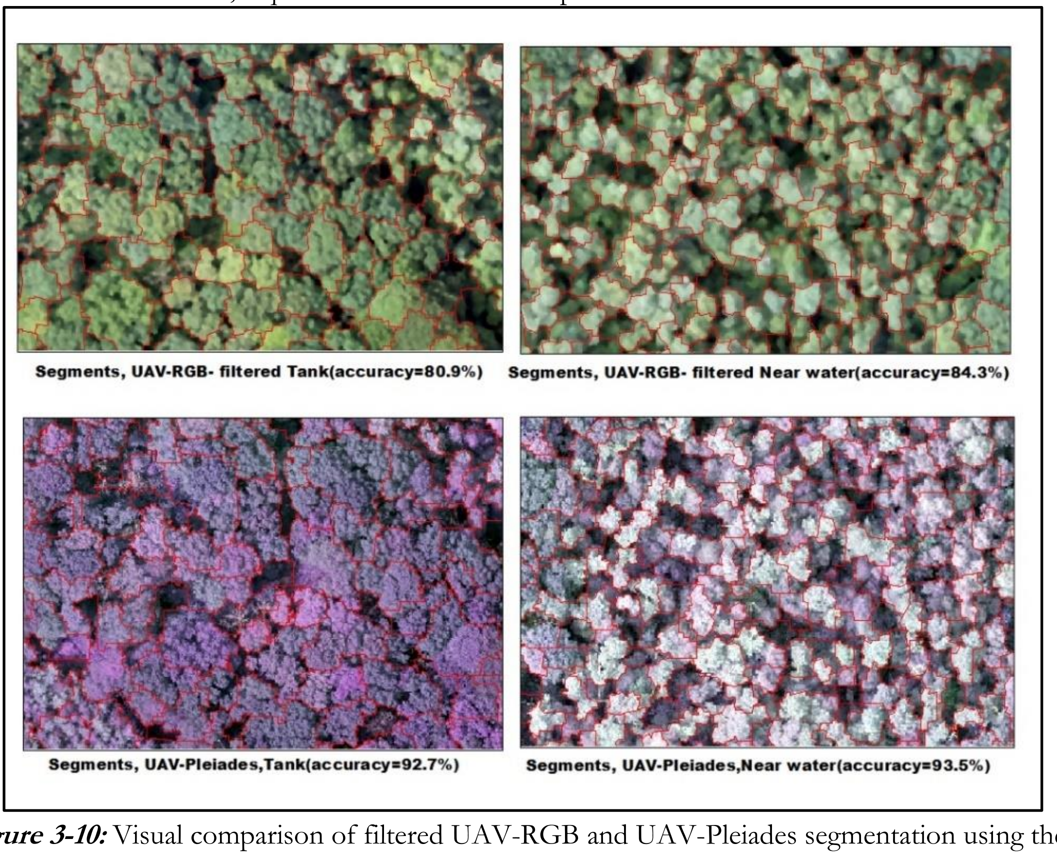

Figure 3-10: Visual comparison of filtered UAV-RGB and UAV-Pleiades segmentation using the block 6 (tank), and block 5 (near water)

As can be seen in table 3-8 the UAV-Pleiades image show highest accuracy in block 5 (91.9%) and lowest in block 5 (64.2%), compared to the filtered UAV-RGB with 84.8% and 78.2% in blocks 5 and 4 respectively. The addition of Pleiades image seems to have enhanced segmentation accuracy in the case of blocks 4, 6 and 5.

Table 3-7: Segmentation accuracy of Filtered UAV-RGB and UAV-Pleiades images using five forest blocks

	Block 4	Block 6	Block 1	Block 5	Block 3
Filtered UAV-RGB					
Reference area(ARi)	1789.03	5293.69	1608.56	2994.60	2876.43
segmented area(ADi)	2586.60	4169.79	2065.23	2464.83	2121.26
Intersection(ADi ∩ ARi)	1789.03	5293.69	1608.56	2994.60	2143.55
Over segmentation	0.31	-0.27	0.22	-0.21	-0.01
Under segmentation	0.00	0.00	0.00	0.00	0.25
Total detected error(Dij)	0.22	0.19	0.16	0.15	0.18
Accuracy	78.20	80.94	84.36	84.80	81.97
UAV-Pleiades					
Reference area(ARi)	1104.83	4083.41	1622.88	1860.92	3550.60
segmented area(ADi)	990.95	4553.46	3289.46	1678.55	5720.45
Intersection(ADi ∩ ARi)	1104.83	4083.41	1622.88	1830.22	3548.35
Over segmentation	-0.11	0.10	0.51	-0.09	0.38
Under segmentation	0.00	0.00	0.00	0.02	0.00
Total detected error(Dij)	0.08	0.07	0.36	0.06	0.27
Accuracy	91.87	92.70	64.18	93.50	73.15

3.3.3. Significance test for segmentation accuracies of filtered UAV-RGB, unfiltered UAV-RGB, and UAV-Pleiades image configurations using five forest blocks.

To test the hypothesis that there is no significant difference in the mean area segmented from filtered UAV-RGB, Unfiltered UAV-RGB and UAV-Pleiades image configurations, a student t-test was performed. As can be seen in tables 3-9 and 3-10 below, the distributions of the data extracted from best segmentation of the image categories are sufficiently normal to conduct a student t-test (Schmider, Ziegler, Danay, Beyer, & Bühner, 2010), except in the case of the UAV-Pleiades segments for block 3. Their skewness (< |2.0|), and kurtosis (< |9.0|) values are within acceptable range. In the case of block 3, a log transformation made it significantly normally distributed (skewness=0.07, <|2.0|).

Table 3-8: Normality test using skewness and skewness z-value for data meant for assessing the effect of image configuration on area segmented for forest blocks 1 and 6.

	Unfiltered block 1	Filtered block 1	UAV-Pl block 1	Unfiltered block 6	Filtered block 6	UAV-Pl block 6
Mean	19.25	30.42	47.54	60.09	81.31	91.40
Std. error	0.46	0.84	1.55	2.36	3.14	4.13
Kurtosis	2.63	2.70	4.08	4.36	3.89	9.54
Skewness	1.28	1.36	1.60	1.81	1.67	2.33
Count	665	486	378	367	296	275
Skewness z-value	0.36	0.61	0.97	1.30	1.88	1.77
Kurtosis **z-value**	0.17	0.31	0.38	0.54	0.81	0.43

Table 3-9: Normality test using skewness and skewness z-value for data meant for assessing effect of image configuration on area segmented for blocks 4 and 3

	Unfiltered block 4	**filtered block 4**	**UAV-Pl block 4**	**Unfiltered block 3**	**Filtered block 3**	**UAV-Pl block 3**
Mean	65.30	51.23	54.34	64.35	60.25	108.59
Std. error	3.91	2.57	3.14	3.04	2.80	7.02
Kurtosis	6.05	3.87	7.33	8.75	5.68	16.69
Skewness	2.10	1.82	2.12	2.37	1.98	3.44
Count	166	170	168	232	252	176
Skewness z-value	1.86	1.41	1.48	1.28	1.41	**2.04**
Kurtosis z-value	0.65	0.67	0.43	0.35	0.49	0.42

Pl= Pleiades

Also, Levene's F-test was done to test the assumption of homogeneous variance. As can be seen in table 3-11 below, F (11) = 65.91, p = 9.2E-135, there is a significant difference in the variances at 95% confidence level. Thus, the null hypothesis of equal variances was rejected, and an independent t-test with unequal variances was performed.

Table 3-10: ANOVA results of Levene's test for the theory that segmented area from the different image configurations has equal variances.

Source of Var.	SS	df	MS	F	P-value	F crit
Between Groups	696807.7	11	63346.15	65.91	9.2E-135	1.79
Within Groups	3477524	3618	961.17			
Total	4174331	3629				

The independent t-test with unequal variances (table 3-12), is associated with a significant difference in segmented area between filtered and unfiltered UAV-RGB images for blocks 1 (p = 3.81E-29), 6 (p = 9.39E-08), and 4 (p = 0.003). There is insufficient evidence to reject the null hypothesis in the case of block 3 (p = 0.156) as shown in table 3-12.

Table 3-11: Independent t-test results for the hypothesis that filtering does not affect the area segmented from UAV-RGB image at the 95% confidence level.

	Filtered, n=486 and Unfiltered, n=665 block 1 H_o, $\mu_1 = \mu_2$ df=770	**Filtered, n=296 and Unfiltered=367 block 6 H_o, $\mu_1 = \mu_2$, df=575**	**Filtered, n=170 Unfiltered, n=166 block 4 H_o, $\mu_1 = \mu_2$, df=287**	**Log(Filtered, n=252 Unfiltered, n=232) block 3, H_o, $\mu_1 = \mu_2$, df=481**
t Stat	-11.68	-5.41	-3.01	1.42
P(T<=t)one-tail	1.918E-29	4.695E-08	0.001	0.078
t-Critical, 1-tail	1.65	1.65	1.65	1.65
P(T<=t) 2-tail	3.837E-29	9.391E-08	0.003	0.156
t-Critical, 2-tail	1.96	1.96	1.97	1.96
	Significant difference	Significant difference	Significant difference	No significant difference

In the case of filtered UAV-RGB and UAV-Pleiades, as can be seen in table 3-13 below, the one tail t-test with unequal variance is associated with a significant difference between blocks 1 (p = 4.93E-21), 6 (p = 2.60E-02) and 3 (p = 1.05E-16). Block 4 did not show any significant difference (p = 2.22E-01) in the area segmented for both image configurations.

Table 3-12: Independent t-test results for the hypothesis that there is no significant difference in the area segmented for UAV-RGB and UAV-Pleiades images at 95% confidence level

	Filtered UAV, n=486 and UAV-Pl, n=378 block 1 H_o, $\mu_1 = \mu_2$ df=589	**Filtered UAV, n=296 and UAV-Pl, n=275 block 6 H_o, $\mu_1 = \mu_2$, df=521**	**Filtered UAV, n=170 and UAV-Pl, n=168 block 4 H_o, $\mu_1 = \mu_2$ df=323**	**log(Filtered UAV, n=252 and UAV-Pl, n=176) block 3 H_o, $\mu_1 = \mu_2$ df=379**
t Stat	-9.70	1.95	-0.77	-8.60
P(T<=t) one-tail	4.93E-21	2.60E-02	2.22E-01	1.05E-16
t-Critical,one-tail	1.65	1.65	1.65	1.65
P(T<=t),two-tail	9.86E-21	5.20E-02	4.44E-01	2.11E-16
t-Critical,two-tail	1.96	1.96	1.97	1.97
	Significant	Significant (one tail)	No Significant	significant

3.3.4. SLIC segmentation

In the case of SLIC segmentation, the results were visually poor. As can be seen in figure 3-11 below, post-processing of the output resulted in segments that cut across tree crowns. Therefore, segmentation accuracy assessment was not done for any output from SLIC.

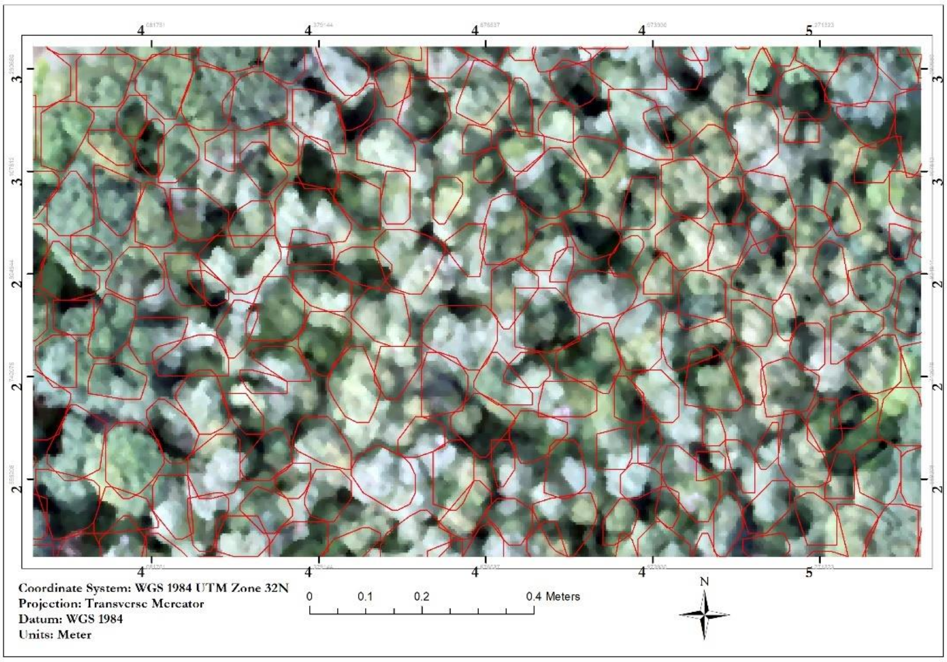

Figure 3-11: Visual assessment of SLIC segmentation output using forest block 5

3.4. Classification of UAV-RGB and UAV-Pleiades image configurations using three classifiers

The classification of UAV-RGB and UAV-Pleiades images was performed using ML, RT and SVM classifiers in ArcMap. The classification accuracies were compared between the two image configurations and across the three classifiers.The results presented in subsequent sections below.

3.4.1. Classification of UAV-RGB images (area-based)

The detailed maps of Maximum likelihood, Random trees and Support vector machine classifications for forest block 1 are presented in figure 3-12 below. From the maps, it can be deduced that the identification of tree species (Beech, Birch and Scots pine) and their surrounding environment from the UAV-RGB image configuration yielded good results using the three classifiers. The Random Trees classification produced a higher overall accuracy of 62%, compared to the 60.6% and 51.7% for Support Vector machines and Maximum likelihood classifiers respectively. Errors could, however, be visually recognised between the water and shadow classes.

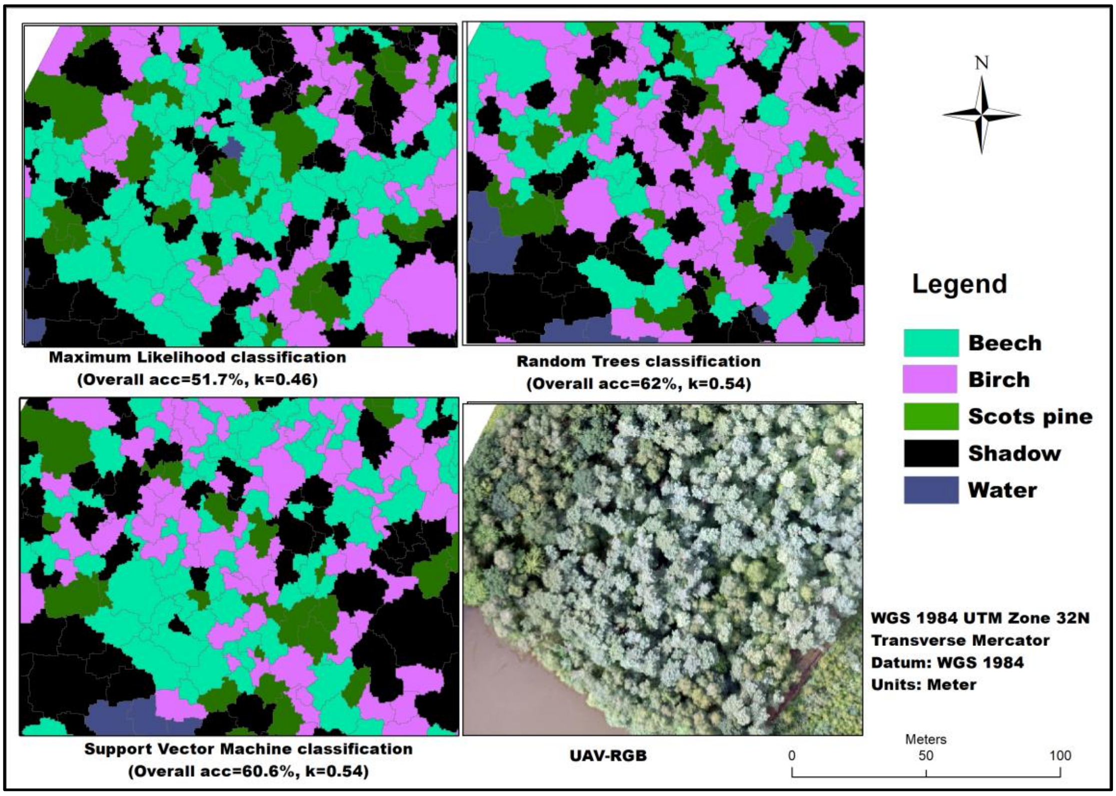

Figure 3-12: Map of block 4 showing classification of UAV-RGB image configuration using Maximum Likelihood (ML), Random Trees (RT) and Support Vector Machine (SVM) algorithms in ArcMap

As can be seen in figure 3-13 below, the classification of Scot pine is 44.7%, 39.3% and 49.3% for SVM, RT and ML classifiers respectively. 24.2% of Beech was correctly classified by SVM and RT, while ML classifier correctly classified 18.2%. All three classifiers registered an accuracy >40% for classification of Birch species. Greater than 50% of the classifications of SVM and RT are in better agreement (Kappa of 53.5% and 53.7% respectively), while < 50% of the classification of ML is in better agreement (kappa of 45.7%).

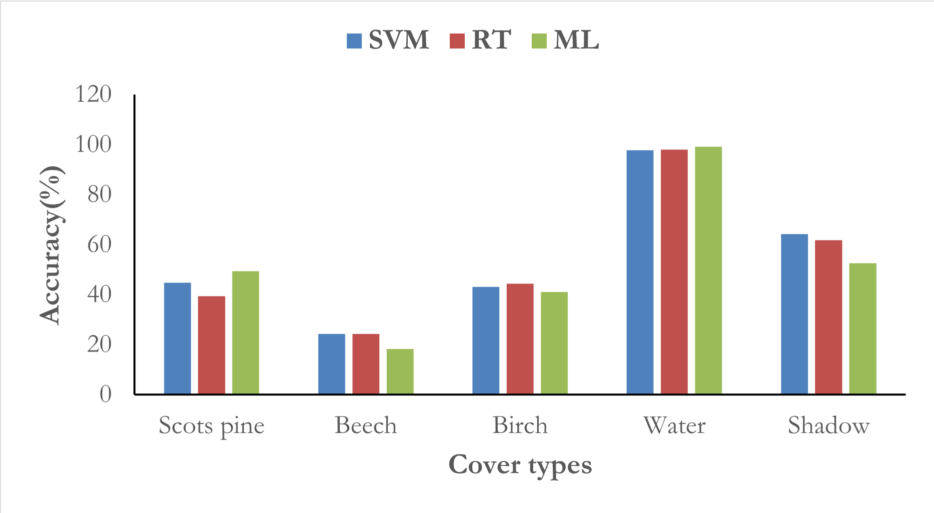

Figure 3-13: Class accuracy for the classification of Scots pine (n=20), Beech (n=10), Birch (20), and their environment (water and shadow) using Support Vector Machines (SVM), Random Trees (RT) and Maximum Likelihood (ML) classifiers.

3.4.2. Classification of UAV-Pleiades image using three classifiers

The tree species maps from Maximum Likelihood, Random Trees and Support Vector Machine classifications for block 4 are presented in figure 3-14. From the maps, it is clear that using the three classifiers, the discrimination of tree species (Beech, Birch and Scots pine) and their surrounding environment yielded good results from the UAV-Pleiades image configuration. The Support Vector Machine and Random Trees classification produced a higher overall accuracy of 84%, compared to the 74.8% for Maximum Likelihood classifiers respectively.

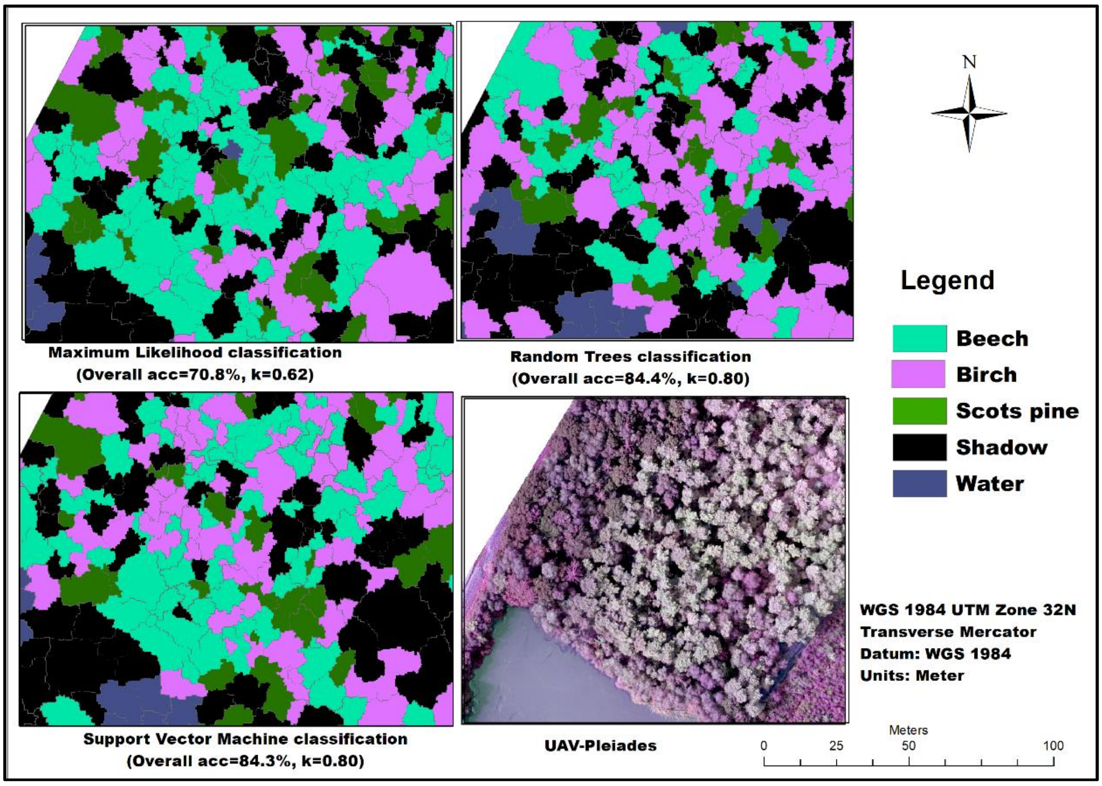

Figure 3-14: Map showing the classification of UAV-Pleiades block 4 using Maximum Likelihood (ML), Random Trees (RT), and Support Vector Machine (SVM) algorithms in ArcMap.

The classification results were best in depicting Scots pine and Birch using all three methods as shown in figure 3-15. Amongst the tree species, Beech had the lowest classification accuracy for all classifiers.

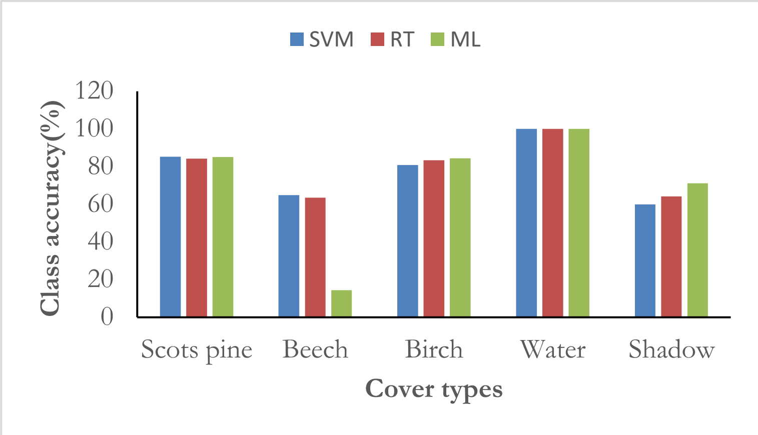

Figure 3-15: Class accuracies for each cover type using Support Vector Machines (SVM), Random Trees (RT) and Maximum likelihood (ML) classification algorithm.

A comparison of class accuracy reveals a general increase in the class accuracies recorded for UAV-Pleiades image compared to the UAV-RGB image. As can be seen in figure 3-16, the addition of Pleiades to UAV-RGB image increased the classification accuracy when using all three of the Classification algorithms. The classification accuracy of UAV-Pleiades image configuration is higher when using SVM and RT, compared to the ML classifier.

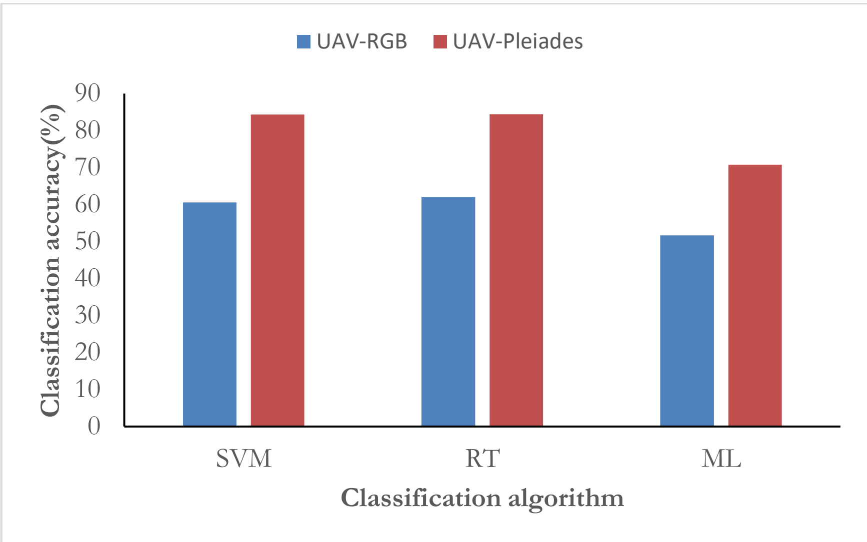

Figure 3-16: Comparing the classification accuracy of UAV-RGB and UAV-Pleiades image configurations using Maximum Likelihood (ML), Random Trees (RT) and Support Vector Machine (SVM) algorithms in ArcMap.

3.4.3. Classification accuracy assessment

The confusion matrix derived from the classification of both image configurations by the three classifiers is presented in table 3-14. The matrices consist of overall accuracy (OA), the degree of agreement between the detailed image and reality (kappa value), and class accuracy (CA). The kappa value, OA and CA for UAV-Pleiades image configuration are higher compared to that from the UAV-RGB image. The three classifiers could identify Scots pine (Sp) and Birch (Bi) from the UAV-Pleiades image with an accuracy of greater than 80%. Random trees and support vector machines classifiers were able to discriminate Beech (Be) and Birch (Bi) species from UAV-Pleiades image with an accuracy (CA) of greater than 60%, compared to the 14% accuracy recorded by maximum likelihood classifier for the same UAV-Pleiades image configuration.

Table 3-13: Comparison of the classification accuracies (%) of tree species and their environment for two image configurations and three classifiers

	UAV-RGB							UAV-Pleiades						
	Sp	**Bi**	**Be**	**Wa**	**Sh**	**OA**	**Kappa**	**Sp**	**Bi**	**Be**	**Wa**	**Sh**	**OA**	**Kappa**
SVM	44.7	43.1	24	97.7	61.7	62	0.54	84.2	83.3	63.5	100	64.2	84.3	0.8
RT	39.3	44.3	24	98	61.7	62	0.54	85.3	81	65	100	63.4	84.4	0.8
ML	49.3	41	18	99.1	52.5	51.7	0.46	85	84.4	14.3	100	71.2	70.8	0.62

Sp-Scots pine, Bi=Birch, Be=Beech, Wa=Water, Sh=Shadow, OA= Class accuracy, RT=Random trees, SVM=Support vector machines, ML=Maximum likelihood.

Details of the confusion matrix is presented in appendix IV. The UAV-Pleiades classifications were used to investigate significant differences in the performance of the three classifiers using McNemar test. The results are presented below.

3.4.4. Comparing SVM, RT and ML classifications results.

From the classified segments, a total of 113 test segments were extracted using the reference polygons. The McNemar's test (Adelabu et al., 2013), investigates if the difference in the number of misclassified test polygons is significant. As can be seen in table 3-15, the McNemar's Chi-squared statistic between SVM and RT classifiers is <1.98 as described in (Manandhar et al., 2009), at the 95% confidence level. The differences in these classifications were found not significant. In the case of SVM and ML, and between RT and ML classifiers, the McNemar's Chi-squared statistic is > 1.98. There is a significant difference in the classification of SVM and ML, and between RT and ML. Details of the 2x2 confusion matrix comparing these classifiers is presented in Appendix V.

Table 3-14: Comparison between SVM, RT and ML classifiers using McNemar's Chi-squared statistic.

	McNemar's Chi-squared statistic
SVM Vs RT	0.6
SVM Vs ML	2.8
RT Vs ML	2.5

3.5. Modelling DBH from CPA, and Predicting AGB

Based on the relationship between DBH and CPA, models were developed, validated and used to model AGB. The results are presented in subsequent sections below.

3.5.1. Relationship between DBH(field derived) and CPA(derived from image segmentation and classification) of tree species

Except for Beech species with a correlation coefficient of 0.27, there is a strong positive relationship between CPA and DBH of all the other tree species in the Amtsvenn area evidenced by the correlation coefficients of 0.85 0.85, 0.94, 0.92 and 0.87 for Scots pine, Birch, Oak and Douglas fir respectively. As can be seen in figure 3-17 below, more than 70% of the variations are explained for each species as shown by the R^2 values.

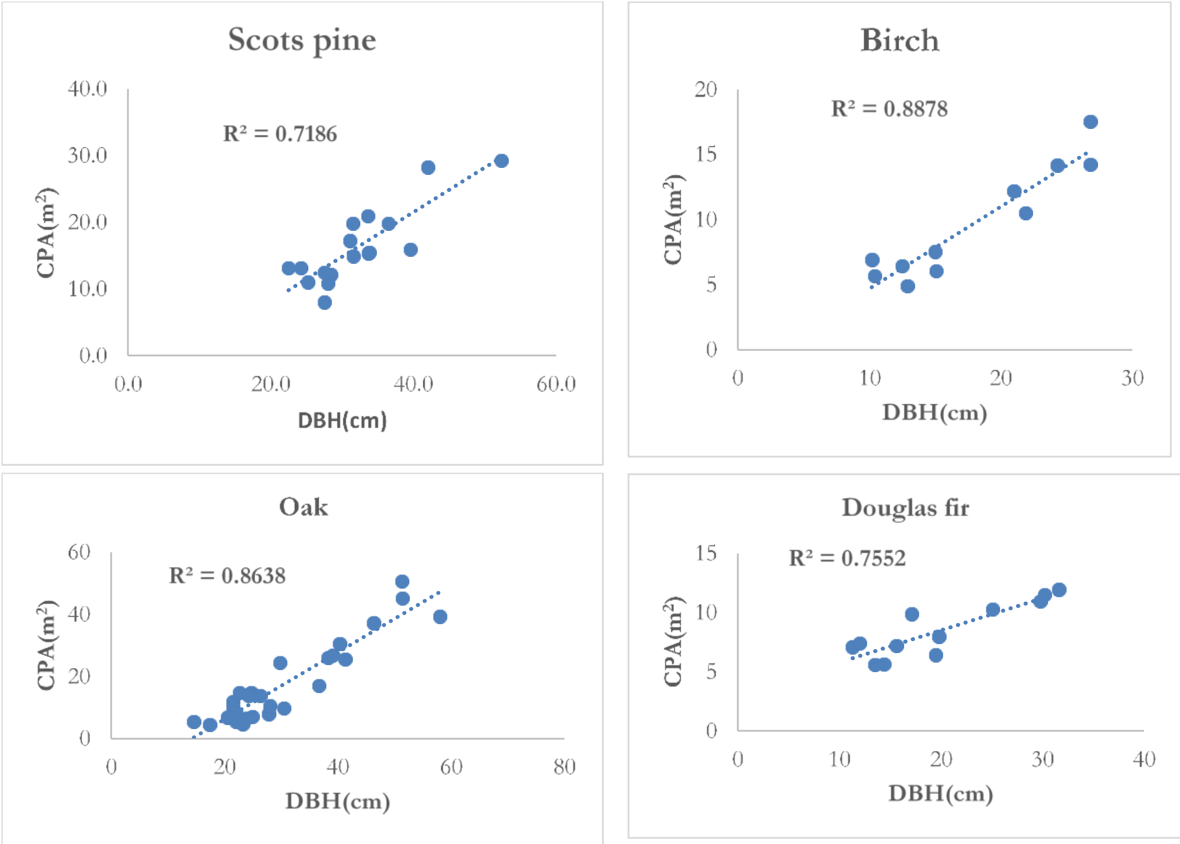

Figure 3-17: Regression analysis between CPA and DBH of main tree species within the Amtsvenn area.

As can be seen in figure 3-18 below, less than 10% of the variations in the CPA and DBH relationship is explained in the case of Beech trees.

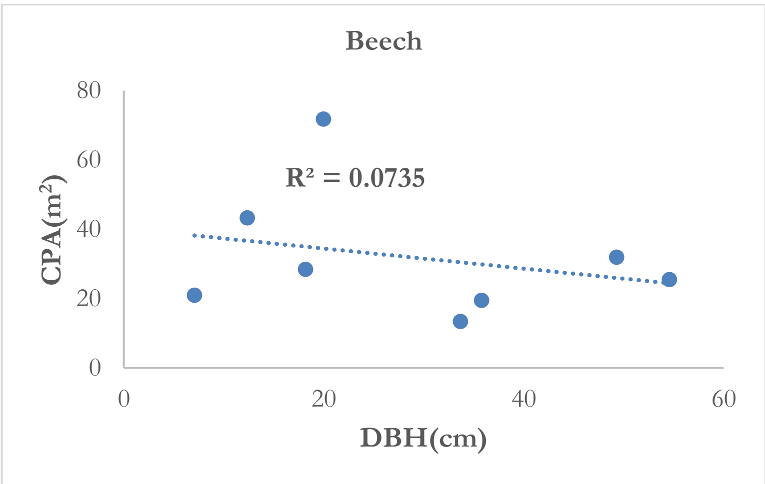

Figure 3-18: Relationship between DBH and CPA for Beech species.

The significance of the CPA and DBH relationship for each of these species was verified in an ANOVA analysis as shown in table 3-16 below. The relationship between CPA and DBH (after the removal of outliers) for Scots pine, Oak, Birch and Douglas fir are significant at 95% confidence level. Based on the significance of the relationships, models were developed. In the case of Beech, the CPA and DBH relationship was weak as can be seen in the figure below. The detailed table showing the t-test results is presented in appendix VI.

Table 3-15: ANOVA test showing the significance of CPA and DBH relationship for tree species at 95% confidence level.

Species	df	r	F	F-critical	P-value
Scots pine	17	0.85	49.2	4.1	6.00E-08
Oak	28	0.93	15.6	4	0.0002
Birch	11	0.94	12.5	4.4	0.002
Douglas fir	12	0.87	26.4	4.3	4.00E-05
Beech	8	0.33	0.1	4.6	0.74

3.5.2. Model development and Validation

Different models were developed and validated using the root mean square errors (RMSE). As can be seen in table 3-17, the RMSE for the Logarithmic model is lowest for Scots pine, and Birch species. The Linear and Power sigmoid models yield almost similar RMSEs for Oak species while the quadratic model yields the lowest RMSE for the Douglas fir species. There was a significant difference between the field derived DBH and predicted DBH from the linear, and power sigmoid models for Scots pine species as shown by their p-values from a one way ANOVA ($p < 0.05$). In the case of Birch and Douglas fir trees, predicted DBH is not significantly different from field DBH (p-values > 0.05). For Oak trees, the logarithmic model predicted DBH which is substantially different from field DBH (p-value < 0.05).

Table 3-16: Comparing DBH and CPA models for Birch, Scots pine, Oak and Douglas fir using R^2 and RMSE.

	Scots pine				**Birch**		
	R^2	RMSE(cm)	P-value		R^2	RMSE(cm)	P-value
Linear	0.77	4.99	7.97E-08	**Linear**	0.87	2.4	0.808
Log	0.65	3.71	9.98E-01	**Log**	0.83	1.3	0.866
Power	0.66	13.67	3.96E-04	**Power**	0.79	1.7	0.845
Quadratic	0.85	4.86	5.03E-01	**Quadratic**	0.88	3.9	0.748

	Oak				**Fir**		
	R^2	RMSE(cm)	P-value		R^2	RMSE	P-value
Linear	0.87	3.75	0.786	**Linear**	0.82	4.63	0.430
Log	0.8	14.49	0.004	**Log**	0.76	4.83	0.452
Power	0.82	3.88	0.785	**Power**	0.76	4.15	0.412
Quadratic	0.87	7.97	0.607	**Quadratic**	0.88	3.71	0.407

3.5.3. Model selection

All models with p-values < 0.05 for each species were rejected. The models with p-values > 0.05 at the 95% confidence level were considered good. However, the best model for each species was finally selected based on the magnitude of p-values and RMSE values. Models with large p-values at 95% confidence level, and accompanied by lower RMSE values were chosen as best for each species. The best models are presented in table 3-18 below.

Table 3-17: Best selected DBH (cm) and CPA (m²) models for Scots pine, Birch, Douglas fir and Oak trees species.

Species	Equation	R^2	RMSE(cm)
Scots pine	DBH= 16.425*ln(CPA) - 12.702	0.65	3.71
Birch	DBH = 13.477*ln(CPA) - 11.165	0.83	1.3
Douglass fir	DBH= 0.5897*CPA² - 7.2282*CPA + 34.959	0.88	3.71
Oak	DBH= 0.8363*CPA + 15.34	0.87	3.75

3.5.4. Predicting DBH with best models using samples from classified map

A total of 17 and 11 segments were used for predicting DBH in the case of Scots pine and Birch respectively. The predicted DBH had means of 32.3cm and 18.2cm for Scots pine and Birch, with respective standard deviations of 5.6cm and 5.9cm. A correlation analysis between field derived and predicted DBH shows a strong positive association in both species; Scots pine (r = 0.76) and Birch (r = 0.90). As can be seen in figure 3-19 below, 64% of field DBH was predicted by the model for Scots pine, while the model for Birch predicted 88%.

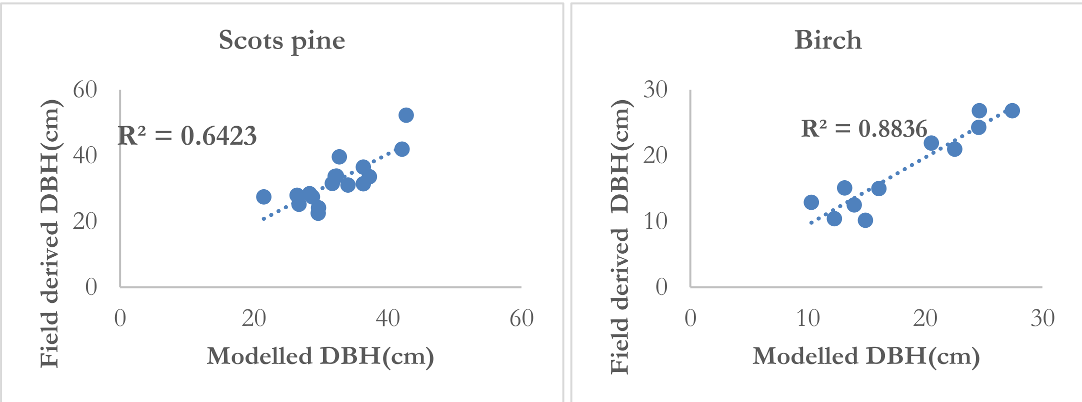

*Figure 3-19:*The relationship between Field derived and Predicted DBH for Scots pine and Birch tree species.

A paired t-test was performed to investigate a significant difference in the predicted and field-derived DBH. As shown in table 3-19, the log-transformed field-derived, and predicted DBH for Scots pine were significantly normally distributed (|skewness and kurtosis z-values| < 1.98) to conduct a t-test. Additionally, both variables were assumed to have homogenous variance based on visual assessment of variations in their descriptive statistics. The field derived from DBH for Birch was significantly not normally distributed (|skewness z-values| ≥ 1.98). To test for a significant difference between field and modelled DBH for Birch species, the Man Whitney U-test was performed. The details of the test are presented in appendix VII.

Table 3-18: Descriptive statistics and normality test for field derived and predicted DBH (Scots pine and Birch)

	log(Field derived DBH)		log(Predicted DBH)	
	Scots pine	Birch	Scots pine	Birch
Mean	1.50	1.23	1.50	1.24
SD	0.09	0.16	0.08	0.14
Skewness z-value	0.03	-1.98	-0.07	-0.97
Kurtosis z-value	0.03	-0.03	0.04	-0.03

The paired t-test (appendix 5) was associated with insufficient evidence to reject the null hypothesis that there is no significant difference between mean modelled and mean field derived DBH for Scots pine at the 95% confidence level. In the case of Birch species, the Man Whitney U-test for the average field and modelled DBH values is associated with a p-value of 0.409, higher than the 0.05 probability level. The results show that there is no statistically significant difference between modelled and field-derived DBH for Birch species.

3.5.5. Predicting AGB using samples from classified map

The predicted AGB had means of 169kg and 154.5kg per tree of Scots pine and Birch, with respective standard deviations of 1.12kg and 31kg. A correlation analysis between field derived and predicted AGB shows a strong positive association for both species; Scots pine (r = 0.83) and Birch (r = 0.96). As can be seen in figure 3-20 below, 68% of field AGB was predicted by the model for Scots pine, while the model for Birch predicted 92%.

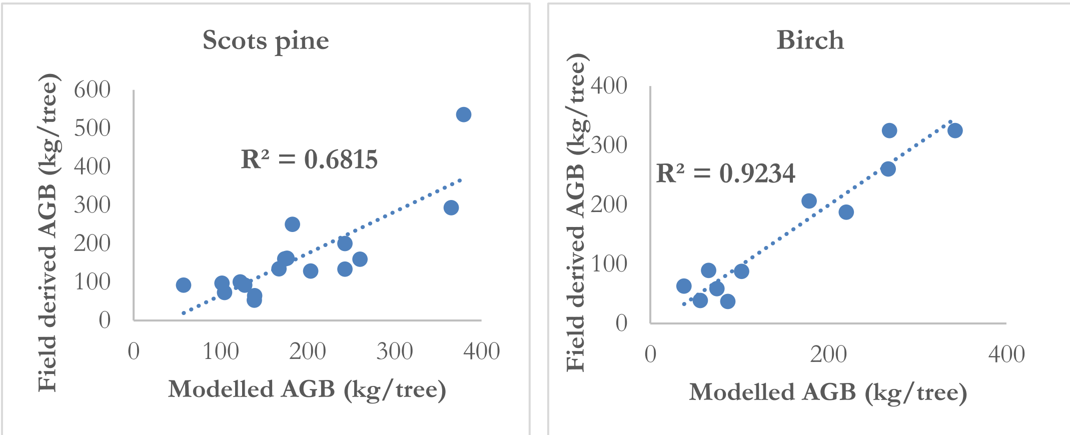

Figure 3-20: Relationship between field derived and modelled AGB for Scots pine and Birch tree species.

A paired t-test was envisaged to investigate a significant difference in the predicted and field-derived AGB, a. A check for normality, as a requirement for the t-test, shows that the variables were not all sufficiently normally distributed. As shown in table 3-20, the log-transformed field-derived, and predicted AGB for Scots pine is normally distributed (|skewness and kurtosis z values| < 1.98). Additionally, both variables were assumed to have homogenous variance based on visual assessment of variations in their descriptive statistics. On the contrary, this was not the same in the case of Birch. Thus a paired t-test was performed for Scots pine, while the Man Whitney U-test was done for Birch species. Details of the paired t-test for Scots pine trees is presented in appendix VIII, while the details of the Man Whitney U test for Birch species is presented in appendix IX.

Table 3-19: Descriptive statistics and normality test for log-transformed field and predicted AGB for Scots pine and Birch tree species.

	Log (Field derived AGB)		**Log (Predicted AGB)**	
	Scots pine	**Birch**	**Scots pine**	**Birch**
Mean	2.23	2.06	2.23	2.09
SD	0.21	0.36	0.21	0.32
Skewness z-value	-0.19	-4.45	-0.19	-2.18
Kurtosis z-value	0.11	-0.06	0.11	-0.07

The paired t-test for Scots pine is associated with a statistically significant difference ($p < 0.05$). Thus, the AGB prediction for Scots pine is significantly higher than the field derived AGB. With this evidence, the null hypothesis is rejected in favour of the alternative hypothesis that there is a significant difference in the mean log-transformed field and modelled AGB for Scots pine at the 95% confidence level. The Man Whitney U-test comparing field derived and modelled AGB for Birch species is associated with a statistically non-significant difference in the field and modelled AGB mean values for Birch species, at the 95% confidence level. The resulting p-value of 0.409 is > 0.05. The relationship between AGB and CPA for Scot pine is linear while AGB has a linear relationship with the natural log of CPA in the case of Birch species.

4. DISCUSSION

4.1. Optimal flight pattern and height of DJ Phantom 4 to produce good quality point cloud and orthophoto of the forest scene.

The first question in this study was to investigate optimal flight pattern and height that the DJ Phantom 4 with RGB camera sensor will fly over forest stands and produce sound quality point cloud and orthophoto. The findings are discussed in section 4.1.1 and 4.1.2 below.

4.1.1. Effect of flight pattern on the quality point cloud and orthophoto generation.

Nasrullah (2016) reported that cross or perpendicular flight pattern showed increased bounded block accuracy and eliminated the systematic radial error, especially in the z-coordinate. The results from this study also shows increased accuracy in the z-axis, and further expose that parallel flight pattern results in a much greater accuracy in the z-axis (height component), and registered more 2D and 3D tie points in the bounded block adjustment process. This means that the parallel flight pattern will result in better construction of point cloud and orthophoto (Khoshelham, 2012; Remondino et al., 2017). The lower RMSE for the height component (z) compared to the perpendicular flight pattern could be due to the differences in the plane of vision. In the parallel flight pattern, the sensor captures information along the same horizontal plane, making the extrapolation of height information more accurate. In the case of perpendicular flight pattern, the plane of vision is different (crossing), thus resulting in greater RMSE.

Nasrullah (2016) used flight height of 70m and 50m to configure the cross flight. In this study, flight heights of 40 and 45m were used to configure cross or perpendicular and parallel flight pattern. There is a possibility that for the effect of flight pattern in this study may have been influenced by the sub-optimal flight height that resulted to some uncalibrated images. Also, the height difference between two flights needs to be sufficient (greater than or equal to 20m) for the effect of flight pattern to be clearly noticed. In addition, the third flight, used to complete the perpendicular and parallel patterns, was acquired on a different date, with slightly different weather conditions. The differences in scene characteristics might have reduced tie point detection, image matching, and masking of the effect of flight pattern on geolocation and bundle block details. Although height information has not been used in this study, the smaller RMSE recorded by the parallel flight pattern is suggestive that parallel flight pattern could be better in the event that height information is needed. However, the observed differences in geolocation and bounded block adjustment details in this study qualitatively informs that the parallel flight pattern has chances of producing better quality point cloud and orthophoto.

4.1.2. Effect of flight height on the quality point cloud and orthophoto generation.

Increase in flight height above tree canopy increased the number of calibrated images, the number of 2D and 3D key points, and the RMSE error especially in the z-axis (height). This increase was relatively small and consistent with the results from the studies of Tahar, (2015) and Udin & Ahmad, (2014), who used Sony NEX-5n camera sensor on a multirotor UAV. The observed pattern in flight height and image calibration, 2D and 3D tie points and RMSE could be explained by the dynamic nature of remotely sensed target (trees). The leaves and branches of trees are always in motion from the movement of air, resulting in blurring of images. The movements change the orientation of the leaves at the time of image capture. At lower altitudes, the UAV camera sensor captures very fine details like changes in leave orientation, the intensity of sunshine, water on leaves. Once images are captured under such circumstances, the scenes appear to be different, irrespective of the overlap, and thus the description, identification and matching of tie points during the photogrammetric process are negatively influenced. Because the scene will be slightly different, the number of tie points identified and matched reduced, and image matching and calibration becomes a problem, leaving gaps in the areas where un-calibration occurred as shown in figure 4-1 below with red points.

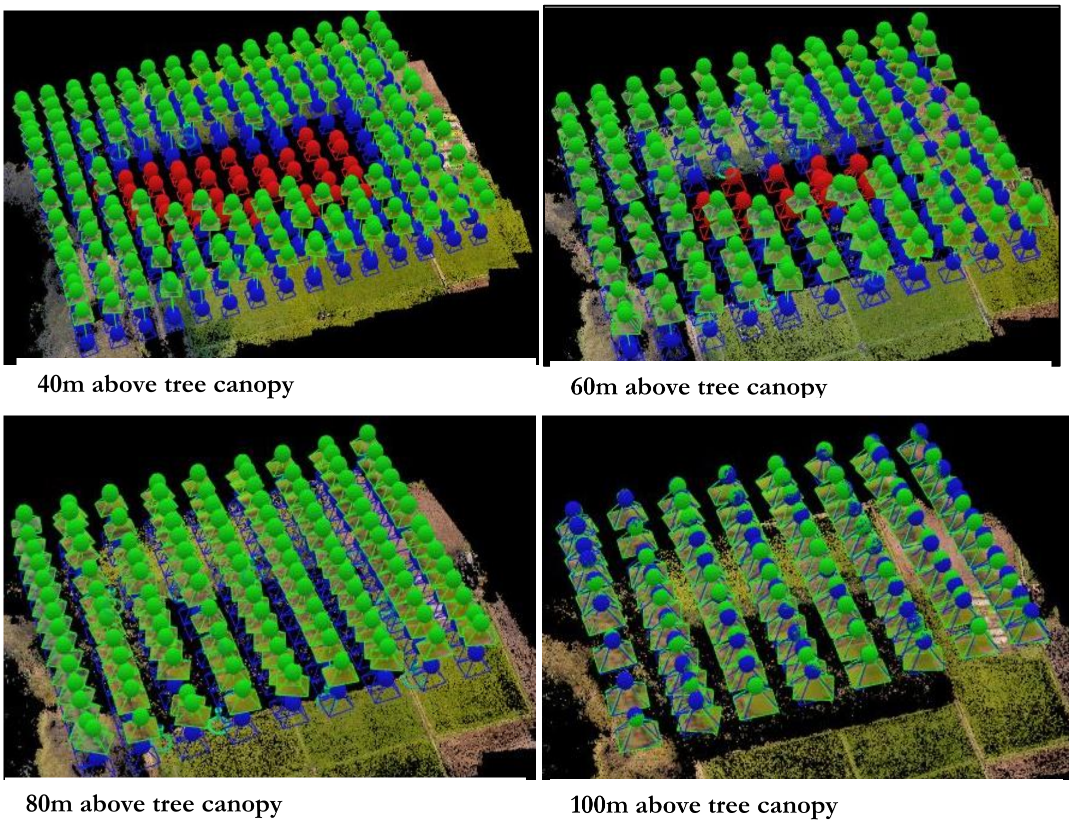

Figure 4-1: Variation in flight height and effect on image calibration (red points are uncalibrated images, while blue points are calibrated images)

At higher flight altitudes, the camera sensor captures images with coarse resolution, making each image scene identical. This eases feature identification, description, tie point identification and matching in the photogrammetric process, and enhances image calibration. However, increase in flight height above tree canopy increases the geolocation error related to GCPs and CPs, especially in the z-axis (height component).This is so because, at higher flight altitudes, the ground control points (GCPs) become less visible. Thus while marking them in Pix4D, their centres are not very visible. This result is in line with the work of (Tahar, 2015), who reported a jump in the RMSE of the GCPs in the vertical axis while using a Hexacopter UAV (Rotary-wing).

According to the Pix4D user manual, a minimum flight height of 60m is sufficient for image calibration. Contrary to this prescription, this study reveals a minimum flight height of 80m above tree canopy (higher for the DJ Phantom 4 drone resulted in a 100% calibration, all things being equal. This minimum flight height is different for different camera sensors. A Canon ELPH 520 HS digital camera attached to a commercial multirotor UAV produces optimal image calibration and good quality 3D products at a flight altitude of 20m above trees (Dandois et al., 2015). The minimum flight may also vary slightly over different forest types (open or closed, deciduous or coniferous). However, the number of flights used in this study are limiting. There is a need to do many more replications, and over different forest structures and types to ascertain this claim.

4.2. Segmentation of UAV-RGB and UAV-Pleiades image blocks using Multiresolution and SLIC segmentation algorithms.

The second question in this research was to investigate which image configuration; UAV-RGB and UAV-Pleiades result in a better segmentation. The objective begins with investigating the effects of filtering on segmentation accuracy of UAV-RGB image, then proceeded to investigate segmentation accuracy between UAV-RGB and UAV-Pleiades image configurations. Also, this question extended to evaluate which segmentation algorithm (SLIC or Multiresolution) does a better segmentation of the image configurations. The results are discussed in sections 4.2.1 and 4.2.2 below.

4.2.1. Segmentation of UAV-RGB and UAV-Pleiades image blocks using Multiresolution segmentation algorithm in eCognition.

The multi-resolution segmentation accuracy was numerically different for all the image configurations. The difference reflects variations in forest structural properties of the blocks. These properties include; stand density, crown size, vertical structure, the proximity to neighbouring trees and spectral variation in each canopy level. According to Block 1 is an open forest dominated by Scots pine. The tree crowns occupy same canopy level, with spaces between the crowns. The other blocks are mixed dense forest, with tree crowns at different canopy levels. However, the crown sizes were variable within each block. For all the segmented forest blocks, filtering resulted in a significant effect on the segmentation of UAV-RGB image blocks 1, 4, 5 and 6. Blocks 1, 5 and 6 show enhancement in segmentation accuracy, while block 4 show a decrease in segmentation accuracy.

According to Pu & Landry (2012), at higher resolutions, branches and within crown variations become prominent as noise, with the potential of complicating segmentation. Block 1 is an open forest with spaces between tree crowns and very low understory shrubs with branches that constitute noise. Filtering must have sharpened the crown boundaries, eliminate background noise from branches and irregularities within crowns and reduce over-segmentation, thus enhancing segmentation accuracy.

Variation in crown size (Gomes & Maillard, 2016), the absence of gaps between neighbouring tree crowns (Mike Wulder, Niemann, & Goodenough, 2000) and the lack of sufficient spectral variations between crowns of different species (Pu & Landry, 2012) limits segmentation accuracy. Blocks 5 and 6 are dense mixed forests with tree crowns touching each other within the same canopy level. However, the blocks show a high degree of spectral variability within the canopy level. Filtering of this blocks must have sharpened the boundaries between crowns with different spectral properties, reduce over-segmentation and significantly enhance segmentation accuracy. The enhancement could have been so because the crowns were not too intermingled.

Contrary to the segmentation of 20 and 25cm resolutions producing best segmentation (Okojie, 2017), the segmentation of 30cm resolution UAV-RGB image blocks yielded accuracies higher than 80%. The high accuracy is probably due to the filtering process which averages spectral values and reduces noise inherent to high-resolution images (Yong, Shi, Benediktsson, & Gao, 2018). Also, the partitioning of the area into blocks may have reduced complexity and thus enhance segmentation accuracy (Larsen et al., 2011).

The segmentation accuracy of the UAV-Pleiades image blocks was higher than the accuracy of segmenting UAV-RGB image blocks. The high accuracy could mean that the addition of the NIR band reduced the effect of shadow that exists in the UAV-RGB image. It, therefore, suggests that the addition of Pleiades to UAV-RGB enhanced the segmentation accuracy. The enhancement was statistically significant in blocks 1, 6 and 3. The significant improvement could be likened to the spatial arrangement and vertical structure of tree species within each of these blocks. Block 1 is an open forest with mostly Scots pine, with visible crowns that are closed within the same canopy. Addition of the NIR band from the Pleiades must have increased spectral variation, clearly showing boundaries and increase segmentation accuracy (Pu & Landry, 2012). Block 6 is composed of Scots pine, Oak, Birch and Beech, with each species grouped within the same canopy level. Block 3 has the Birch and Scots pine occupying specific locations and also within same canopy level. This spatial arrangement of tree species in these blocks, with each species occupying a particular vertical space, might have contributed to the high segmentation accuracy. Also, the addition of the NIR band from the Pleiades must have increase spectral variations between the crowns of tree species in these blocks and so enhance segmentation. The segmentation accuracy associated with the addition of Pleiades to UAV-RGB is higher than the results of segmenting high-resolution images like Geo-eye, and worldview (SK Baral, Malla, & Ranabhat, 2010; Srijana Baral, 2011). The differences in results might be partly because of the ESP2 tool, which was not used in the cited cases.

4.2.2. Segmentation of UAV-RGB and UAV-Pleiades image blocks using SLIC segmentation algorithm in R.

The segmentation of UAV-RGB and UAV-Pleiades using SLIC algorithm in R-environment was not very successful. The segments were visually rejected for quantitative assessment. The segments were of the same sizes, cutting tree crowns in parts and mixing tree crowns. The poor performance is probably because the forest scene is too complicated for the algorithm. The variation in colour and texture gradient in the forest seems too narrow for the algorithm to sufficiently differentiate and clearly segment. SLIC segmentation algorithm may not be suitable if the purpose of segmentation is to extract area for AGB modelling accurately. However, Yuan & Hu (2016) used the algorithm successfully for the identification of diseased tree crowns. In their work, the purpose of segmentation was to identify diseased trees. They generated equally sized SLIC superpixels, capturing mostly the colour information which denoted disease infestation. Pure training and validation samples of diseased and healthy trees were then extracted and used for classification.

4.3. Classification of UAV-RGB and UAV-Pleiades image blocks using Maximum likelihood, Random trees and Support vector machine classifiers.

The third research objective was to investigate the hypothesis that there is no significant difference in tree species classification accuracy using segmented layers from UAV-RGB and UAV-Pleiades images. Also, the objective evaluated classification results from three classifiers. The results are discussed in section 4.3.1 below.

4.3.1. Classification of UAV-RGB image blocks using Maximum likelihood, Random trees and Support vector machine classifiers.

The classification of different tree species in a mixed forest can be challenging using high-resolution UAV-RGB or the multispectral Pleiades as standalone The observed high accuracy can be explained by the sensitivity of the NIR band from the Pleiades to species. On the other hand, the class accuracies for UAV-RGB image block range from 49.3% in Scots pine to 24% in Beech species for all three classifiers. The low accuracy of classifying Beech species is probably because of fewer samples of Beech and high spectral mixing between Beech and Scots pine. Also, the Beech trees were younger, and so mostly occupied the lower canopy, and so its crowns were shaded by the shadows of mature and taller trees, causing it to be seen and classified as a shadow.

The overall accuracy and kappa value recorded in this study for the three classifiers are higher than that discussed in some works (Adelabu et al., 2013; Manandhar, Odeh, & Ancev, 2009). The higher accuracy could be due to the high spatial resolution of images used in this study compared to the 5m resolution of RapidEye dataset used in the other studies. High spatial resolution images display more features and allow the features to be differentiated, compared to lower or coarse resolution images, thus resulting in higher classification accuracies (Adam Van Etten, 2016; Baker, Warner, Conley, & McNeil, 2013; Hsieh, Lee, & Chen, 2001). The classification procedure and environment may also have had an influence. The present study performed classification in ArcMap, while the cited case classified in Matlab. This study made use of feature normalisation method as described in Hsu *et al.*, (2010). According to (Kuzmin et al., 2016), different normalisation methods may exert different effects on different classifiers. However, the impact of feature normalisation methods on classifiers was not assessed in this work. The McNemar test z-score < 1.96 for SVM and RT, mean that there is no significant difference between the classifiers. However, the classifications of ML and SVM, and ML and RT are significantly different at the 95% confidence level (test statistic >1.96). SVM and RT performed significantly better than the ML. This result is in line with other works (Adelabu et al., 2013; Manandhar et al., 2009; Pouteau, Collin, & Stoll, 2013), stating that RT and SVM are much better classifiers for tree species identification compared to Maximum Likelihood. The reason might be because SVM and RT classifiers perform multiple classifications of each object as specified by the user, then perform a vote of the plurality to get the best classification for each object. The iterative process minimises chances of misclassification. Also, these two classifiers require a limited number of pure samples to get a reasonable classification.

4.4. Modelling DBH and AGB for Scots pine and Birch.

The last objective of this study was to model DBH using CPA from classified segments and use this to model AGB and carbon. The objective was to answer the hypothesis that there is no significant difference between modelled and field measured DBH of dominant tree species within the study area. The selected species are Scots pine and Birch, and the findings are discussed in sections 4.4.1 below.

4.4.1. Modelling DBH and AGB for Scots pine and Birch

Logarithmic models were selected for predicting DBH from CPA for Scots pine and Birch. These logarithmic models reveal that as much as the increase in CPA increase DBH of both species, the rate of increase decreases as the competition for space, nutrients increases in the forest. The predictions made by these models were not significantly different from the estimations using field data. However, these models are more valid within the data range used for their development, and their statistical power is limiting due to the small sample size of trees used in their development and validation. The relationship between AGB and CPA is linear for Scots pine, meaning an increase in CPA increases AGB. This outcome is similar to the work of Wardani (2014), who reported a linear relationship between AGB and CPA for Scot pine species. In the case of Birch species, AGB has a linear relationship with the natural log of CPA. There is a need for further studies in this location to comprehensively ascertain the true statistical power of these models using larger sample size for each tree species.

4.5. The Limitations of this research.

Based on the highlighted results and their implications vis a vis other works, the following limitations are highlighted.

4.5.1. UAV data acquisition

The collection of data to test the effect of flight height on quality of point cloud ought to have been done over the same forest for which flight pattern was investigated. However, this was not possible due to permit issues. Also, the number of flights were limited to efficiently determine flight height thresholds for the Phantom 4 over the forest with different structures.

4.5.2. Field data collection and classification

The field data from last year was collected not for species classification, thus would not be most appropriate for classification. Species like Beech, Douglas fir, and European hornbeam were not adequately represented in the dataset for classification. Of the Scots pine, Birch and Oak that had a reasonable count, their locations were conflicting in some cases. The classification made use of feature normalisation without investigating the potential effect of this on classifiers, and so might have introduced anomalies.

5. CONCLUSIONS AND RECOMMENDATIONS

5.1. Conclusions.

This study has demonstrated that the relatively cheaper and flexible UAV platform with RGB camera sensor on board can produce images (UAV-RGB) from which the classification of tree species and their environment is possible. It has also demonstrated the added value of combining UAV-RGB and multispectral Pleiades images on segmentation and tree species identification for carbon estimation in a temperate forest. The study had four research questions and six hypothesis. The specific conclusions are presented below.

Question1: *Which flight pattern is optimal to generate a high-quality point cloud of forest stands using DJ Phantom 4 with RGB camera, and which flight height is optimal for image calibration?*

The first part of question one sort to assess the effect of flight pattern on the quality of point cloud, and orthophoto of forest stands, using DJ Phantom 4 with RGB camera onboard. This assessment is based on geolocation and bundle block adjustment details. The study reports that the parallel flight pattern results in a lower RMSE and higher numbers of 2D and 3D points, presuming that it has more chances of producing better quality products. The study thus concludes that flight pattern has an effect on the geolocation and bundle block adjustment details, and thus quality of point cloud and orthophoto of forest stands using DJ Phantom 4 with RGB camera on board.

The second part of question one investigated the relationship between flight height of DJ Phantom 4 above tree canopy and image calibration. The findings conclude that increase in flight height above tree canopy increases the % of images calibrated. Furthermore, the study identifies a minimum flight height of 80m above tree canopy as optimal for image calibration. However, the study equally notes that this minimum flight height may vary for different forest types, as well as for different camera brands mounted on the UAV.

Question 2: *Which image configuration; produces better segmentation (UAV-RGB or UAV-RGB combined with - the Pleiades), and which algorithm performs better segmentation: multiresolution (in eCognition) or SLIC (in R)?*

Two null hypothesis are investigated here. The first hypothesis states that there is no significant difference in the segmentation accuracies of UAV-RGB and UAV-Pleiades images. From statistical results, the study reports that the segmentation accuracy of UAV-Pleiades image was significantly higher than that of the UAV-RGB. Therefore, the work concludes with 95% confidence that the addition of multispectral Pleiades significantly increases the segmentation accuracy of UAV-RGB image.

The second hypothesis presumes that there is no significant difference in the accuracies of Multiresolution and SLIC segmentations of UAV-RGB and UAV-Pleiades images. From the results, the study concludes that multiresolution performs better to extract tree crowns for modelling DBH and forest carbon.

Question 3: *What is the difference in classification accuracy of tree species from UAV-RGB and UAV-Pleiades images using Maximum Likelihood, Random trees and support vector machine classifiers in ArcMap?*

Two null hypothesis are investigated in this question. The first is that the addition of multispectral Pleiades has no significant effect on the classification accuracy of UAV-RGB image. To this hypothesis, findings show both class and overall accuracy of UAV-Pleiades image significantly higher than that of UAV-RGB image. The study concludes with 95% certainty that the addition of multispectral Pleiades significant enhances and increase the accuracy of classifying Scots pine, Birch, and Beech tree species within their environment.

The second hypothesis states that there is no significant difference in the classification accuracy of ML, RT and SVM classifiers. The results reveal that the classification accuracies of RT and SVM were significantly higher than that of the ML classifier. Also, the classification accuracies of RT and SVM were significantly not different. The study thus concludes with 95% certainty that RT and SVM classifiers are significantly better in classifying Scots pine, Birch, and Beech tree species within their environment.

Question 4: *What is the difference in aboveground carbon of dominant tree species estimated from field DBH and predicted DBH using the best-classified image?*

The logarithmic relationships between CPA and DBH for Scots pine and Birch species are significant at the 95% confidence level and can be used to predict DBH as well as AGB/Carbon from classified segments with 95% confidence. However, these models are limiting due to a small sample size of tree species used.

Overall, combining the relative cheap UAV-RGB and multispectral Pleiades (50cm) images yields a better segmentation and classification of tree species. Multiresolution segmentation is better for AGB modelling while SLIC could be used for classification. Considering low cost, and simplicity, the implementation of SVM, ML and RT in ArcMap is preferred over environments like eCognition and R. Also, the use of support vector machine and random trees classifier with limited training samples is preferred to maximum likelihood classifier. The resulting CPA-DBH, and DBH-AGB models and be used to estimate forest carbon with certainty but low statistical power due to a limited sample size of trees used.

5.2. Recommendations.

Based on the highlighted limitations of the study, the following recommendations are highlighted

1. More regular and replicative flights should be performed with the Phantom 4 drone over a variety of forest stands at different flight heights to determine the minimum and maximum flight height that may result in good quality 3D products. Once optimal flight height is resolved, then the influence of flight pattern can be further investigated.
2. Exploiting the use of ESP2 tool for better segmentation could yield some impressive results, especially comparing it across different image resolutions.
3. Exploring the impact of feature normalisation on classification accuracy is in prospect.
4. The use of DJ Phantom 4 drone with multispectral and RGB camera sensor mounted on board could be used and comparison between UAV-RGB, UAV-RGB-NIR and UAV-Pleiades image configurations on segmentation and classification investigated. In this scenario, comparison of segmentation and classification with and without canopy height model could yield interesting results.

LIST OF REFERENCES

Achanta, R., Shaji, A., Smith, K., Lucchi, A., Fua, P., & Süsstrunk, S. (2012). SLIC superpixels compared to state-of-the-art superpixel methods. *IEEE Transactions on Pattern Analysis and Machine Intelligence*, *34*(11), 2274–2281. https://doi.org/10.1109/TPAMI.2012.120

Adam Van Etten. (2016). Quantifying the Effects of Resolution on Image Classification Accuracy. Retrieved February 10, 2018, from https://medium.com/the-downlinq/quantifying-the-effects-of-resolution-on-image-classification-accuracy-7d657aca7701

Adelabu, S., Mutanga, O., Adam, E., & Cho, M. A. (2013). Exploiting machine learning algorithms for tree species classification in a semiarid woodland using RapidEye image. *Journal of Applied Remote Sensing*, *7*(1), 73480-73480–13. https://doi.org/10.1117/1.JRS.7.073480

Alcantarilla, P. F., Bartoli, A., & Davison, A. J. (2012). KAZE features. In A. Fitzgibbon et al. (Eds.) (Ed.), *Lecture Notes in Computer Science (including subseries Lecture Notes in Artificial Intelligence and Lecture Notes in Bioinformatics)* (Vol. 7577 LNCS, pp. 214–227). Berlin heidelberg: Springer-Verlag. https://doi.org/10.1007/978-3-642-33783-3_16

Alkema, D., Bijker, W., Sharifa, A., Vekerdy, Z., & Verhoef, W. (2013). Data Integration. In Valentyn Tolpekin & Alfred Stein (Eds.), *The Core of GIScience: A systems-based approach* (pp. 206–213). Enschede: Faculty of Geo-Information Science and Earth Observation (ITC), University of Twente. https://doi.org/10.1016/B978-0-12-385889-4.00013-2

Anders, N. S., Seijmonsbergen, A. C., & Bouten, W. (2011). Segmentation optimization and stratified object-based analysis for semi-automated geomorphological mapping. *Remote Sensing of Environment*, *115*(12), 2976–2985. https://doi.org/10.1016/j.rse.2011.05.007

Arvor, D., Durieux, L., Andrés, S., & Laporte, M.-A. (2013). Advances in Geographic Object-Based Image Analysis with ontologies: A review of main contributions and limitations from a remote sensing perspective. *ISPRS Journal of Photogrammetry and Remote Sensing*, *82*, 125–137. https://doi.org/10.1016/j.isprsjprs.2013.05.003

Assefa, G., Mengistu, T., Getu, Z., & Zewdie, S. (2013). Training manual on: Forest carbon pools and carbon stock assessment in the context of SFM and REDD+, 74. Retrieved from https://www.forestcarbonpartnership.org/sites/fcp/files/2015/October/Forest carbon stock assessment_Manual.pdf

ASTRIUM. (2012). Pléiades Imagery User Guide, *2*(October), 118. Retrieved from http://www.cscrs.itu.edu.tr/assets/downloads/PleiadesUserGuide.pdf

Baboo, D. S. S., & Devi, M. R. (2010). An Analysis of Different Resampling Methods in Coimbatore, District. *Global Journal of Computer Science and Technology*, *10*(15), 61–66. Retrieved from http://globaljournals.org/GJCST_Volume10/10-An-Analysis-of-Different-Resampling-Methods-in-Coimbatore-District.pdf

Bailey, W. M. (2012). *Unmanned Aerial Vehicle Path Planning and Image Processing for Orthoimagery and Digital Surface Model Generation(Master's Thesis). Vanderbilt University*. University of Vanderbilt, Nashville. https://doi.org/10.1017/CBO9781107415324.004

Baker, B. A., Warner, T. A., Conley, J. F., & McNeil, B. E. (2013). Does spatial resolution matter? A multi-scale comparison of object-based and pixel-based methods for detecting change associated with gas well drilling operations. *International Journal of Remote Sensing*, *34*(5), 1633–1651. https://doi.org/10.1080/01431161.2012.724540

Bakx, W., Gorte, B., Feringa, W., Grabmaier, K., Janssen, L., Kerle, N., … Weir, M. (2013). Pre-processing. In Valentyn Tolpekin & Alfred Stein (Eds.), *The core of GISience:a processed-based approach* (2013th ed., p. 524). Enschede: Faculty of Geo-Information Science and earth Observation(ITC), University of Twente. Retrieved from https://issuu.com/itc-utwente/docs/corebook2013_05_pre-processing

Baral, S. (2011). *Mapping Carbon Stock Using High Resolution Satellite Images In Sub-Tropical Forest Of Nepal(Master's Thesis)*. University of Twente Faculty of Geo-Information Science and Earth Observation (ITC). Retrieved from http://www.itc.nl/library/papers_2011/msc/nrm/baral.pdf

Baral, S., Malla, R., & Ranabhat, S. (2010). Above-ground carbon stock assessment in different forest types of Nepal. *Banko Janakari*, *19*(2). https://doi.org/10.3126/banko.v19i2.2979

Belgiu, M., & Dră guţ, L. (2014). Comparing supervised and unsupervised multiresolution segmentation approaches for extracting buildings from very high resolution imagery. *ISPRS Journal of Photogrammetry and Remote Sensing*, *96*, 67–75. https://doi.org/10.1016/j.isprsjprs.2014.07.002

Birdal, A. C., Avdan, U., & Türk, T. (2017). Estimating tree heights with images from an unmanned aerial vehicle. *Geomatics, Natural Hazards and Risk*, *5705*(May), 1–13. https://doi.org/10.1080/19475705.2017.1300608

Bonan, G. B. (2008). Forests and Climate Change: Forcings, Feedbacks, and the Climate Benefits of Forests. *Science*, *320*(5882), 1444–1449. https://doi.org/10.1126/science.1155121
Breiman, L. (2001). Random forests. *Machine Learning*, *45*(1), 5–32. https://doi.org/10.1023/A:1010933404324
Brown, S. (2002). Measuring carbon in forests: Current status and future challenges. In *Environmental Pollution* (Vol. 116, pp. 363–372). https://doi.org/10.1016/S0269-7491(01)00212-3
Burges, C. J. C. (1998). A Tutorial on Support Vector Machines for Pattern Recognition. *Data Mining and Knowledge Discovery*, *2*(2), 121–167. https://doi.org/10.1023/A:1009715923555
Carleer, A., & Wolff, E. (2004). Exploitation of Very High Resolution Satellite Data for Tree Species Identification. *Photogrammetric Engineering & Remote Sensing*, *70*(1), 135–140. https://doi.org/10.14358/PERS.70.1.135
Cho, M. A., Debba, P., Mathieu, R., Naidoo, L., van Aardt, J., & Asner, G. P. (2010). Improving Discrimination of Savanna Tree Species Through a Multiple-Endmember Spectral Angle Mapper Approach: Canopy-Level Analysis. *IEEE Transactions on Geoscience and Remote Sensing*, *48*(11). https://doi.org/10.1109/TGRS.2010.2058579
Chubey, M. S., Franklin, S. E., & Wulder, M. A. (2006). Object-based Analysis of Ikonos-2 Imagery for Extraction of Forest Inventory Parameters. *Photogrammetric Engineering & Remote Sensing*, *72*(4), 383–394. https://doi.org/10.14358/PERS.72.4.383
Climate-Data.org. (2017). Climate Penang: Temperature, Climate graph, Climate table for Penang - Climate-Data.org. Retrieved July 27, 2017, from https://en.climate-data.org/location/890057/
Clinton, N., Holt, A., Yan, L., & Gong, P. (2010). An Accuracy Assessment Measure for Object Based Image Segmentation. *Photogrammetric Engineering & Remote Sensing*, *76*, 289–299. https://doi.org/10.14358/PERS.76.3.289.
Crommelinck, S., Bennett, R., Gerke, M., Koeva, M. N., Yang, M. Y., & Vosselman, G. (2017). SLIC superpixels for object delineation from UAV data. In *International Journal of Photogrametry and Remote Sensing*. Retrieved from http://uavg17.ipb.uni-bonn.de/wp-content/papercite-data/pdf/crommelinck2017uavg.pdf
Dandois, J. P., Olano, M., & Ellis, E. C. (2015). Optimal altitude, overlap, and weather conditions for computer vision uav estimates of forest structure. *Remote Sensing*, *7*(10), 13895–13920. https://doi.org/10.3390/rs71013895
Drǎ guţ, L., Tiede, D., & Levick, S. R. (2010). ESP: a tool to estimate scale parameter for multiresolution image segmentation of remotely sensed data. *International Journal of Geographical Information Science*, *24*(6), 859–871. https://doi.org/10.1080/13658810903174803
eCognition Developer. (2016). *eCognition ® Developer* (2016th ed.). Munich, Germany: Trimble Germany GmbH. Retrieved from www.eCognition.com
Erdbrügger, J. (2017). *Comparing tree parameters extracted from UAV images and TLS data sets Comparing tree parameters extracted from UAV images and TLS data sets (Master's Thesis)*. ITC, Faculty of Geo-Information Science and Earth Observation of the University of Twente.
Esch, T., Thiel, M., Bock, M., Roth, A., & Dech, S. (2008). Improvement of Image Segmentation Accuracy Based on Multiscale Optimization Procedure. *IEEE Geoscience and Remote Sensing Letters*, *5*(3), 463–467. https://doi.org/10.1109/LGRS.2008.919622
FAO. (2010). *Global Forest Resources Assessment 2010* (163rd ed.). *FAO Forestry Paper* (Vol. 163). Rome,: FAO. https://doi.org/ISBN 978-92-5-106654-6
Fassnacht, F. E., Latifi, H., Stereńczak, K., Modzelewska, A., Lefsky, M., Waser, L. T., … Ghosh, A. (2016, December). Review of studies on tree species classification from remotely sensed data. *Remote Sensing of Environment*. https://doi.org/10.1016/j.rse.2016.08.013
Fischler, M. A., & Bolles, R. C. (1981). Random sample consensus: a paradigm for model fitting with applications to image analysis and automated cartography. *Communications of the ACM*, *24*(6), 381–395. https://doi.org/10.1145/358669.358692
Ghassemian, H. (2016). A review of remote sensing image fusion methods. *Information Fusion*, *32*, 75–89. https://doi.org/10.1016/j.inffus.2016.03.003
Gibbs, H. K., & Herold, M. (2007). Tropical deforestation and greenhouse gas emissions. *Environmental Research Letters*, *2*(4), 45021. https://doi.org/10.1088/1748-9326/2/4/045021
Gomes, M. F., & Maillard, P. (2016). Detection of Tree Crowns in Very High Spatial Resolution Images. In Maged Marghany (Ed.), *Environmental Applications of Remote Sensing* (pp. 41–71). InTech. https://doi.org/10.5772/62122
Gonzalez, P., Asner, G. P., Battles, J. J., Lefsky, M. A., Waring, K. M., & Palace, M. (2010). Forest carbon densities and uncertainties from Lidar, QuickBird, and field measurements in California. *Remote Sensing*

of Environment, *114*(7), 1561–1575. https://doi.org/10.1016/j.rse.2010.02.011
Haijian, M., Qiming, Q., & Xinyi, S. (2008). Shadow segmentation and compensation in high resolution satellite images. In *International Geoscience and Remote Sensing Symposium (IGARSS)* (Vol. 2, p. II-1036-II-1039). Boston: IEEE. https://doi.org/10.1109/IGARSS.2008.4779175
Hay, G. J., Castilla, G., Wulder, M. A., & Ruiz, J. R. (2005). An automated object-based approach for the multiscale image segmentation of forest scenes. *International Journal of Applied Earth Observation and Geoinformation*, *7*, 339–359. https://doi.org/10.1016/j.jag.2005.06.005
Hoaglin, D. C., Iglewicz, B., & Tukey, J. W. (1986). Performance of Some Resistant Performance Rules for Labeling Outlier. *Journal of the American Statistical Association*, *81*(396), 991–999. https://doi.org/10.1080/01621459.1986.10478363
Hogland, J., Billor, N., & Anderson, N. (2013). Comparison of standard maximum likelihood classification and polytomous logistic regression used in remote sensing. *European Journal of Remote Sensing*, *46*(1), 623–640. https://doi.org/10.5721/EuJRS20134637
Hongoa, J. R. (2017). *Accuracy of Tree Height Derived from Point Clouds of of UAV Compared to Airborne LiDAR and Its Effect on Estimating Biomass and Carbon Stock in Part of Tropical Forest in Malaysia(Master's Thesis).* University of Twente Faculty of Geo-Information Science and Earth Observation (ITC). Retrieved from https://ezproxy.utwente.nl:2315/library/2017/msc/nrm/hongoa.pdf
Hsieh, P. F., Lee, L. C., & Chen, N. Y. (2001). Effect of spatial resolution on classification errors of pure and mixed pixels in remote sensing. *IEEE Transactions on Geoscience and Remote Sensing*, *39*(12), 2657–2663. https://doi.org/10.1109/36.975000
Hsu, C., Hsu, C., Chang, C., & Lin, C. (2010). A practical guide to support vector classification. Retrieved from http://citeseerx.ist.psu.edu/viewdoc/summary?doi=10.1.1.224.4115
Hu, Y., Su, Z., Li, W., Li, J., & Ke, X. (2015). Influence of tree species composition and community structure on carbon density in a subtropical forest. *PLoS ONE*, *10*(8), e0136984. https://doi.org/10.1371/journal.pone.0136984
Hua, J., Balagurunathan, Y., Chen, Y., Lowey, J., Bittner, M. L., Xiong, Z., … Sebastiani, P. (2006). Normalization Benefits Microarray-Based Classification. *EURASIP Journal on Bioinformatics and Systems Biology*, *43056*, 1–13. https://doi.org/10.1155/BSB/2006/43056
IPCC. (2006). *2006 IPCC Guidelines for National Greenhouse Gas Inventories*. *IPCC*. Retrieved from http://www.ipcc-nggip.iges.or.jp
IPCC. (2013). Fifth Assessment Report - Climate Change 2013. Retrieved May 31, 2017, from http://www.ipcc.ch/report/ar5/wg1/
Jagalingam, P., & Hegde, A. V. (2015). A Review of Quality Metrics for Fused Image. *Aquatic Procedia*, *4*, 133–142. https://doi.org/10.1016/j.aqpro.2015.02.019
Jeevan, M. (2015). Possibly the simplest way to explain K-Means algorithm. Retrieved February 4, 2018, from http://bigdata-madesimple.com/possibly-the-simplest-way-to-explain-k-means-algorithm/
Jose, ´ Navar *. (2009). Allometric equations for tree species and carbon stocks for forests of northwestern Mexico. *Forest Ecology and Managemen*, *257*, 427–434. https://doi.org/10.1016/j.foreco.2008.09.028
Juniati, E., & Arrofiqoh, E. N. (2017). Comparison of pixel-based and object-based classification using parameters and non-parameters approach for the pattern consistency of multi scale landcover. In *International Archives of the Photogrammetry, Remote Sensing and Spatial Information Sciences - ISPRS Archives* (Vol. 42, pp. 765–771). Wuhan, China. https://doi.org/10.5194/isprs-archives-XLII-2-W7-765-2017
Kanavath, R., & Metz, M. (2017). GRASS GIS manual: i.superpixels.slic. Retrieved August 11, 2017, from https://grass.osgeo.org/grass72/manuals/addons/i.superpixels.slic.html
Karna, Y. K., Hussin, Y. A., Gilani, H., Bronsveld, M. C., Murthy, M. S. R., Qamer, F. M., … Baniya, C. B. (2015). Integration of WorldView-2 and airborne LiDAR data for tree species level carbon stock mapping in Kayar Khola watershed, Nepal. *International Journal of Applied Earth Observation and Geoinformation*, *38*, 280–291. https://doi.org/10.1016/j.jag.2015.01.011
Ke, Y., Quackenbush, L. J., & Im, J. (2010). Synergistic use of QuickBird multispectral imagery and LIDAR data for object-based forest species classification. *Remote Sensing of Environment*, *114*(6), 1141–1154. https://doi.org/10.1016/j.rse.2010.01.002
Khoshelham, K. (2012). Accuracy Analysis of Kinect Depth Data. *ISPRS - International Archives of the Photogrammetry, Remote Sensing and Spatial Information Sciences*, *XXXVIII-5/*, 133–138. https://doi.org/10.5194/isprsarchives-XXXVIII-5-W12-133-2011
Koju, U., Zhang, J., & Gilani, H. (2017). Exploring multi-scale forest above ground biomass estimation with optical remote sensing imageries. *IOP Conference Series: Earth and Environmental Science*, *57*(1), 12011. https://doi.org/10.1088/1755-1315/57/1/012011
Kuzmin, A., Korhonen, L., Manninen, T., & Maltamo, M. (2016). Automatic segment-level tree species

recognition using high resolution aerial winter imagery. *European Journal of Remote Sensing*, *49*(1), 239–259. https://doi.org/10.5721/EuJRS20164914
Larsen, M., Eriksson, M., Descombes, X., Perrin, G., Brandtberg, T., & Gougeon, F. A. (2011). Comparison of six individual tree crown detection algorithms evaluated under varying forest conditions. *International Journal of Remote Sensing*, *32*(20), 5827–5852. https://doi.org/10.1080/01431161.2010.507790
Lawrence, R. L., Wood, S. D., & Sheley, R. L. (2006). Mapping invasive plants using hyperspectral imagery and Breiman Cutler classifications (randomForest). *Remote Sensing of Environment*, *100*(3), 356–362. https://doi.org/10.1016/j.rse.2005.10.014
Lobo, A. (1997). Image segmentation and discriminant analysis for the identification of land cover units in ecology. *IEEE Transactions on Geoscience and Remote Sensing*, *35*(5), 1136–1145. https://doi.org/10.1109/36.628781
Lu, D. (2006). The potential and challenge of remote sensing‐ based biomass estimation. *International Journal of Remote Sensing*, *27*(7), 1297–1328. https://doi.org/10.1080/01431160500486732
Lu, D., & Weng, Q. (2007). A survey of image classification methods and techniques for improving classification performance. *International Journal of Remote Sensing*, *28*(5), 823–870. https://doi.org/10.1080/01431160600746456
Manandhar, R., Odeh, I. O. A., & Ancev, T. (2009). Improving the Accuracy of Land Use and Land Cover Classification of Landsat Data Using Post-Classification Enhancement. *Remote Sensing*, *1*(3), 330–344. https://doi.org/10.3390/rs1030330
Möller, M., Lymburner, L., & Volk, M. (2007). The comparison index: A tool for assessing the accuracy of image segmentation. *International Journal of Applied Earth Observation and Geoinformation*, *9*(3), 311–321. https://doi.org/10.1016/j.jag.2006.10.002
Mtui, Y. P. (2017). *Tropical rainforest above Ground Biomass and Carbon Stock Estimation for Upper and Lower canopies Using Terrestrial Laser Scanner and Canopy Height Model from Unmanned Aerial Vehicle (UAV) in Ayer-Hitam, Malaysia(Master's Thesis).* University of Twente Faculty of Geo-Information and Earth Observation(ITC). Retrieved from http://www.itc.nl/library/papers_2017/msc/nrm/mtui.pdf
Näsi, R., Honkavaara, E., Tuominen, S., Saari, H., Pölönen, I., Hakala, T., … Reinikainen, J. (2016). UAS based tree species identification using the novel fpi based hyperspectral cameras in visible, NIR and SWIR spectral ranges. *ISPRS - International Archives of the Photogrammetry, Remote Sensing and Spatial Information Sciences*, *XLI-B1*, 1143–1148. https://doi.org/10.5194/isprs-archives-XLI-B1-1143-2016
Nasrullah, A. R. (2016). Systematic Analysis of Unmanned Aerial Vehicle (UAV) Derived Product Quality (MSc thesis), (February), 95. Retrieved from http://adlib.itc.utwente.nl/detail.aspx?parentpriref=
Nevalainen, O., Honkavaara, E., Tuominen, S., Viljanen, N., Hakala, T., Yu, X., … Tommaselli, A. (2017). Individual Tree Detection and Classification with UAV-Based Photogrammetric Point Clouds and Hyperspectral Imaging. *Remote Sensing*, *9*(3), 185. https://doi.org/10.3390/rs9030185
Nex, F., & Remondino, F. (2014). UAV for 3D mapping applications: A review. *Applied Geomatics*. https://doi.org/10.1007/s12518-013-0120-x
Obeyed, M. H. (2014). Predictive models between diameter , height , crown diameter and age of Pinus brutia ten . in Zawita and Atrush districts. *Global Journal of Bio-Science and Biotechnology*, *3*(2), 203–210. Retrieved from http://www.scienceandnature.org/GJBB_Vol3(2)2014/GJBB-V3(2)2014-14.pdf
Okojie, J. A. (2017). *Assessment of Forest Tree Structural Parameter Extractability From Optical Imaging Uav Datasets, in Ahaus Germany(Master's Thesis).* University of Twente Faculty of Geo-Information Science and Earth Observation (ITC). Retrieved from http://www.itc.nl/library/papers_2017/msc/nrm/okojie.pdf
Onilude, Q. ., Akinyemi, O., Julius A.J, Ogunremi, O. ., & Ogunremi, O. . (2015). Modelling DBH and Crown diameter for Triplochiton scleroxylon (K. Schum) in Nigeria. *Academia Journal of Scientific Research*, *3*(11), 178–183. https://doi.org/10.15413/ajsr.2015.0122
Pandit, V. R., & Bhiwani, R. J. (2015). Image Fusion in Remote Sensing Applications: A Review. *International Journal of Computer Applications*, *120*(10), 975–8887. https://doi.org/10.1007/3-540-29711-1
Patenaude, G., Milne, R., & Dawson, T. P. (2005, April). Synthesis of remote sensing approaches for forest carbon estimation: reporting to the Kyoto Protocol. *Environmental Science and Policy*. https://doi.org/10.1016/j.envsci.2004.12.010
Pix4D SA. (2017). Pix4Dmapper 4.1 Use Manual. (Pix4D SA, Ed.). Lausanne: Pix4D. Retrieved from https://support.pix4d.com/hc/en-us/articles/204272989-Offline-Getting-Started-and-Manual-pdf-
Pouliot, D. A., King, D. J., Bell, F. W., & Pitt, D. G. (2002). Automated tree crown detection and delineation in high-resolution digital camera imagery of coniferous forest regeneration. *Remote Sensing of Environment*, *82*(2–3), 322–334. https://doi.org/10.1016/S0034-4257(02)00050-0
Pouteau, R., Collin, A., & Stoll, B. (2013). A Comparison of Machine Learning Algorithms for Classification of Tropical Ecosystems Observed by Multiple Sensors at Multiple Scales. In *34th International Symposium*

on Remote Sensing of Environment (pp. 1–6). Retrieved from http://www.isprs.org/proceedings/2011/isrse-34/211104015Final00913.pdf

Pretzsch, H. (2009). Forest dynamics, growth and yield: From measurement to model. *Southern Forests*, *73*(1), 1–39. https://doi.org/10.1007/978-3-540-88307-4_1

Proisy, C., Couteron, P., & Fromard, F. (2007). Predicting and mapping mangrove biomass from canopy grain analysis using Fourier-based textural ordination of IKONOS images. *Remote Sensing of Environment*, *109*(3), 379–392. https://doi.org/10.1016/j.rse.2007.01.009

Pu, R., & Landry, S. (2012). A comparative analysis of high spatial resolution IKONOS and WorldView-2 imagery for mapping urban tree species. *Remote Sensing of Environment*, *124*, 516–533. https://doi.org/10.1016/j.rse.2012.06.011

Radoux, J., & Bogaert, P. (2017). Good practices for object-based accuracy assessment. *Remote Sensing*, *9*(7), 23. https://doi.org/10.3390/rs9070646

Ramón, A. D.-V., Raúl, de la R., Lorenzo, L., & Pablo, J. Z.-T. (2015). High-resolution airborne UAV imagery to assess olive tree crown parameters using 3D photo reconstruction: Application in breeding trials. *Remote Sensing*, *7*(4), 4213–4232. https://doi.org/10.3390/rs70404213

Remondino, F., Nocerino, E., Toschi, I., & Menna, F. (2017). A Critical Review of Automated Photogrammetric Processing of Large Datasets. *The International Archives of the Photogrammetry, Remote Sensing and Spatial Information Sciences, Volume XLII-2/W5, 2017 26th International CIPA Symposium 2017, 28 August–01 September 2017, Ottawa, Canad*, *XLII*(September), 9. https://doi.org/10.5194/isprs-archives-XLII-2-W5-591-2017

Sahu, D. K., & Parsai, M. P. (2012). Different Image Fusion Techniques –A Critical Review. *International Journal of Modern Engineering Research (IJMER)*, *2*(5), 4298–4301. Retrieved from www.ijmer.com

Schmider, E., Ziegler, M., Danay, E., Beyer, L., & Bühner, M. (2010). Is It Really Robust? *ResearchGate*, *6*(4), 147–151. https://doi.org/10.1027/1614-2241/a000016

Schwenk, W. S., Donovan, T. M., Keeton, W. S., & Nunery, J. S. (2012). Carbon storage, timber production, and biodiversity: Comparing ecosystem services with multi-criteria decision analysis. *Ecological Applications*, *22*(5), 1612–1627. https://doi.org/10.1890/11-0864.1

Shah, S. K., & Acharya, H. (2010). Modelling the relationship between canopy projection area and above-ground carbon stock of intermingled canopy trees using high-resolution satellite imagery. *Banko Janakari*, *23*(2), 20–29. https://doi.org/10.3126/banko.v23i2.15463

Sharma, R. P., Vacek, Z., & Vacek, S. (2016). Individual tree crown width models for Norway spruce and European beech in Czech Republic. *Forest Ecology and Management*, *366*, 208–220. https://doi.org/10.1016/j.foreco.2016.01.040

Sheldon, S., Xiao, X., & Biradar, C. (2012). Mapping evergreen forests in the Brazilian Amazon using MODIS and PALSAR 500-m mosaic imagery. *ISPRS Journal of Photogrammetry and Remote Sensing*, *74*, 34–40. https://doi.org/10.1016/j.isprsjprs.2012.07.003

Shimano, K. (1997). Analysis of the relationship between DBH and crown projection area using a new model. *Journal of Forest Research*, *2*(4), 237–242. https://doi.org/10.1007/BF02348322

Sileshi, G. W. (2014). A critical review of forest biomass estimation models, common mistakes and corrective measures. *Forest Ecology and Management*, *329*, 237–254. https://doi.org/10.1016/j.foreco.2014.06.026

Simon, B. (2017). Superpixels in imager | R-bloggers. Retrieved December 24, 2017, from https://www.r-bloggers.com/superpixels-in-imager/

Sisodia, P. S., Tiwari, V., & Kumar, A. (2014). Analysis of Supervised Maximum Likelihood Classification for remote sensing image. In *International Conference on Recent Advances and Innovations in Engineering (ICRAIE-2014)* (pp. 1–4). IEEE. https://doi.org/10.1109/ICRAIE.2014.6909319

Sivagami, R., Vaithiyanathan, V., Sangeetha, V., Ifjaz Ahmed, M., Joseph Abraham Sundar, K., & Divya Lakshmi, K. (2015). Review of image fusion techniques and evaluation metrics for remote sensing applications. *Indian Journal of Science and Technology*, *8*(35). https://doi.org/10.17485/ijst/2015/v8i35/86677

Strahler, A. H., Boschetti, L., Foody, G. M., Friedl, M. A., Hansen, M. C., Herold, M., … Woodcock, C. E. (2006). *Global Land Cover Validation: Recommendations for Evaluation and Accuracy Assessment of Global Land Cover Maps. Change* (Vol. 48pp). Italy. https://doi.org/10.1080/01431160512331326521

Stutz, D. (2015). Superpixel segmentation: An evaluation. In *Lecture Notes in Computer Science (including subseries Lecture Notes in Artificial Intelligence and Lecture Notes in Bioinformatics)* (Vol. 9358, pp. 555–562). Springer International Publishing. https://doi.org/10.1007/978-3-319-24947-6_46

Stutz, D., Hermans, A., & Leibe, B. (2016). Superpixels: An Evaluation of the State-of-the-Art. *Computer Vision and Image Understanding*. https://doi.org/10.1016/j.cviu.2017.03.007

Tahar, K. N. (2015). Multi rotor UAV at different altitudes for slope mapping studies. In *International Archives* *of the Photogrammetry, Remote Sensing and Spatial Information Sciences - ISPRS Archives* (Vol. 40, pp. 9–16). Toronto, Canada: The International Archives of the Photogrammetry, Remote Sensing and Spatial Information Sciences, Volume XL-1/W4. https://doi.org/10.5194/isprsarchives-XL-1-W4-9-2015

Udin, W. S., & Ahmad, A. (2014). Assessment of photogrammetric mapping accuracy based on variation flying altitude using unmanned aerial vehicle. In *IOP Conference Series: Earth and Environmental Science* (Vol. 18, p. 12027). Kuching, Sarawak,: Institute of Physics Publishing. https://doi.org/10.1088/1755-1315/18/1/012027

Ward, B. S. (2013). The Global Forest Observations Initiative (GFOI), *m*(January 2013), 2011–2013.

Wardani, S. F. Y. (2014). Estimation of Carbon Stock Changes in Above Ground Woody Biomass due to Volcano Pyroclastic Flow and Pyroclastic Surge. *Indonesian Journal of Geography*, *46*(1), 78. https://doi.org/10.22146/ijg.4993

Weather and Climate.com. (2017). Weather and Climate: Gronau, Germany, average monthly min and max Temperature (fahrenheit). Retrieved July 27, 2017, from https://weather-and-climate.com/average-monthly-min-max-Temperature-fahrenheit,gronau-north-rhine-westphalia-de,Germany

Wei, W., Chen, X., & Ma, A. (2005). Object-oriented Information Extraction and Application in High-resolution Remote Sensing Image. *Ieee*, *0*(C), 5–8. https://doi.org/10.1109/IGARSS.2005.1525737

Weih, R. C., & Riggan, N. D. (2010). Object-based classification vs. pixel-based classification: Comparitive importance of multi-resolution imagery. *The International Archives of the Photogrammetry, Remote Sensing and Spatial Information Sciences*, *XXXVIII*, 1–6. Retrieved from https://pdfs.semanticscholar.org/c09d/862d113ccf887813119b9a26606e64064f55.pdf

White, J. C., Coops, N. C., Wulder, M. A., Vastaranta, M., Hilker, T., & Tompalski, P. (2016, September 2). Remote Sensing Technologies for Enhancing Forest Inventories: A Review. *Canadian Journal of Remote Sensing*. Taylor & Francis. https://doi.org/10.1080/07038992.2016.1207484

Wulder, M. a. (1998). Optical remote-sensing techniques for the assessment of forest inventory and biophysical parameters. *Progress in Physical Geography*, *22*(4), 449–476. https://doi.org/10.1177/030913339802200402

Wulder, M. A., White, J. C., Niemann, K. O., & Nelson, T. (2004). Comparison of airborne and satellite high spatial resolution data for the identification of individual trees with local maxima filtering. *International Journal of Remote Sensing*, *25*(11), 2225–2232. https://doi.org/10.1080/01431160310001659252

Wulder, M., Niemann, K. O., & Goodenough, D. G. (2000). Local maximum filtering for the extraction of tree locations and basal area from high spatial resolution imagery. *Remote Sensing of Environment*, *73*(1), 103–114. https://doi.org/10.1016/S0034-4257(00)00101-2

Yilmaz, V., & Gungor, O. (2016). Fusion of very high-resolution UAV images with criteria-based image fusion algorithm. *Arabian Journal of Geosciences*, *9*(1), 1–16. https://doi.org/10.1007/s12517-015-2109-8

Yong, L. Z., Shi, W. Z., Benediktsson, J. A., & Gao, L. (2018). A modified mean filter for improving the classification performance of very high-resolution remote-sensing imagerye. *International Journal of Remote Sensing*, *39*(3), 770–785. https://doi.org/10.1080/01431161.2017.1390275

Yuan, Y., & Hu, X. (2016). Random forest and objected-based classification for forest pest extraction from uav aerial imagery. *ISPRS - International Archives of the Photogrammetry, Remote Sensing and Spatial Information Sciences*, *XLI-B1*, 1093–1098. https://doi.org/10.5194/isprs-archives-XLI-B1-1093-2016

Zarco-Tejada, P. J., Diaz-Varela, R., Angileri, V., & Loudjani, P. (2014). Tree height quantification using very high resolution imagery acquired from an unmanned aerial vehicle (UAV) and automatic 3D photo-reconstruction methods. *European Journal of Agronomy*, *55*, 89–99. https://doi.org/10.1016/j.eja.2014.01.004

Zhang, C., & Qiu, F. (2012). Mapping individual tree species in an urban forest using airborne lidar data and hyperspectral imagery. *Photogrammetric Engineering & Remote Sensing*, *78*(10), 1079–1087. https://doi.org/10.14358/PERS.78.10.1079

Zhang, X., Wang, S., Yang, M., & Li, H. (2016). Research Article Individual Tree Location and Canopy Delineation Based on Quickbird Imagery. *Advance Journal of Food Science and Technology*, *10*(2), 99–110. https://doi.org/10.19026/ajfst.10.1806

Zhang, Y. J. (1996). A survey on evaluation methods for image segmentation. *Pattern Recognition*, *29*(8), 1335–1346. https://doi.org/10.1016/0031-3203(95)00169-7

Zhang, Z., Cao, L., & She, G. (2017). Estimating forest structural parameters using canopy metrics derived from airborne LiDAR data in subtropical forests. *Remote Sensing*, *9*(9), 940. https://doi.org/10.3390/rs9090940

Zhu, H., Cai, L., Liu, H., & Huang, W. (2016). Information extraction of high resolution remote sensing images based on the calculation of optimal segmentation parameters. *PLoS ONE*, *11*(6), e0158585. https://doi.org/10.1371/journal.pone.0158585

Appendix I: Variation in parameters for the segmentation of forest blocks under three imaged configurations, and segmentation levels selected for assessment.

Filtered UAV-RGB

Forest block	**Step size level 1**	**Step size level 2**	**Step size level 3**	**Shape**	**Compactness**	**Level selected**
1(Open forest)	0.2	0.4	5	0.6	0.9	1
3(Building)	0.5	1	20	0.7	0.9	1&2
4(Water)	0.5	1	20	0.7	0.8	1&2
5(Near water)	0.5	1	20	0.7	0.8	1&2
6(Tank)	0.5	1	20	0.7	0.9	1&2

Unfiltered UAV-RGB

Forest block	**Step size level 1**	**Step size level 2**	**Step size level 3**	**Shape**	**Compactness**	**Level selected**
1(Open forest)	0.5	1	20	0.6	0.8	1&2
3(Building)	0.5	0.8	1.6	0.8	0.9	2&3
4(Water)	0.5	1	20	0.6	0.8	1&2
5(Near water)	0.5	1	20	0.7	0.8	1&2
6(Tank)	0.5	1	20	0.6	0.8	1&2

UAV-Pleiades

Forest block	**step size level 1**	**step size level 2**	**step size level 3**	**shape**	**compactness**	**Level selected**
1(Open forest)	0.2	0.4	5	0.7	0.9	1&2
3(Building)	0.5	1	20	0.7	0.8	1&2
4(Water)	0.5	1	20	0.7	0.8	1&2
5(Near water)	0.5	1	20	0.6	0.8	1&2
6(Tank)	0.4	0.8	1.6	0.5	0.8	1&2

Appendix II: SLIC segmentation

```
#SEGMENTING UAV-RGB AND UAV-PLEIADES IMAGE CONFIGURATIONS WITH SLIC#
#-Section 1-------------------------------------------------------------------------------------------------------
library(tidyverse)
library(imager)
library(rgdal)
library(maptools)
library(rgdal)
library(spdep)
library(rgeos)
library(raster)
library(spatstat)
library(sp)
Path=("C:/Users/Effiom/Desktop/SLIC_segmentation_filtered_30cm/Near_Water")
setwd(Path)
im <- load.image("Path/Near_water_3x3filtered_30cm1.jpg")
#Convert to CIELAB colour space, then create a data.frame with three colour channels as columns
d <- sRGBtoLab(im) %>% as.data.frame(wide="c")%>%
  dplyr::select(-x,-y)
#Run k-means with 2 centers
km <- kmeans(d,2)
#Turn cluster index into an image
seg <- as.cimg(km$cluster,dim=c(dim(im)[1:2],1,1))
plot(im,axes=FALSE)
highlight(seg==1)
#-Section 2-------------------------------------------------------------------------------------------------------
#Compute SLIC superpixels
#im: input image
#nS: number of superpixels
#ratio: determines compactness of superpixels.
#low values will result in pixels with weird shapes
#... further arguments passed to kmeans
slic <- function(im,nS,compactness=1,...)
{
  #If image is in colour, convert to CIELAB
  if (spectrum(im) ==3) im <- sRGBtoLab(im)
  #The pixel coordinates vary over 1...width(im) and 1...height(im)
  #Pixel values can be over a widely different range
  #We need our features to have similar scales, so
  #we compute relative scales of spatial dimensions to colour dimensions
  sc.spat <- (dim(im)[1:2]*.28) %>% max #Scale of spatial dimensions
  sc.col <- imsplit(im,"c") %>% map_dbl(sd) %>% max
  #Scaling ratio for pixel values
  rat <- (sc.spat/sc.col)/(compactness*10)
   X <- as.data.frame(im*rat,wide="c") %>% as.matrix
  #Generate initial centers from a grid
  ind <- round(seq(1,nPix(im)/spectrum(im),l=nS))
  #Run k-means
  km <- kmeans(X,X[ind,],...)
  #Return segmentation as image (pixel values index cluster)
  seg <- as.cimg(km$cluster,dim=c(dim(im)[1:2],1,1))
  #Superpixel image: each pixel is given the colour of the superpixel it belongs to
  sp <- map(1:spectrum(im),~ km$centers[km$cluster,2+.]) %>% do.call(c,.) %>% as.cimg(dim=dim(im))
```

```
  #Correct for ratio
  sp <- sp/rat
  if (spectrum(im)==3)
  {
    #Convert back to RGB
    sp <- LabtosRGB(sp)
  }
  list(km=km,seg=seg,sp=sp)
}
#-Section 3-----------------------------------------------------------------------------------------------------
#400 superpixels
out <- slic(im,1800, compactness = 1)
#Superpixels
plot(out$sp,axes=FALSE)
#Segmentation
plot(out$seg,axes=FALSE)
#Show segmentation on original image
(im*add.colour(abs(imlap(out$seg)) == 0)) %>% plot(axes=FALSE)
segPoly<-((abs(imlap(out$seg)) == 0))
plot(segPoly)
#----------------------------------------------------------------------------------------------------------
```
Source: (Simon, 2017)

Appendix III: Orthophotos produced from images taken at different heights above tree canopy

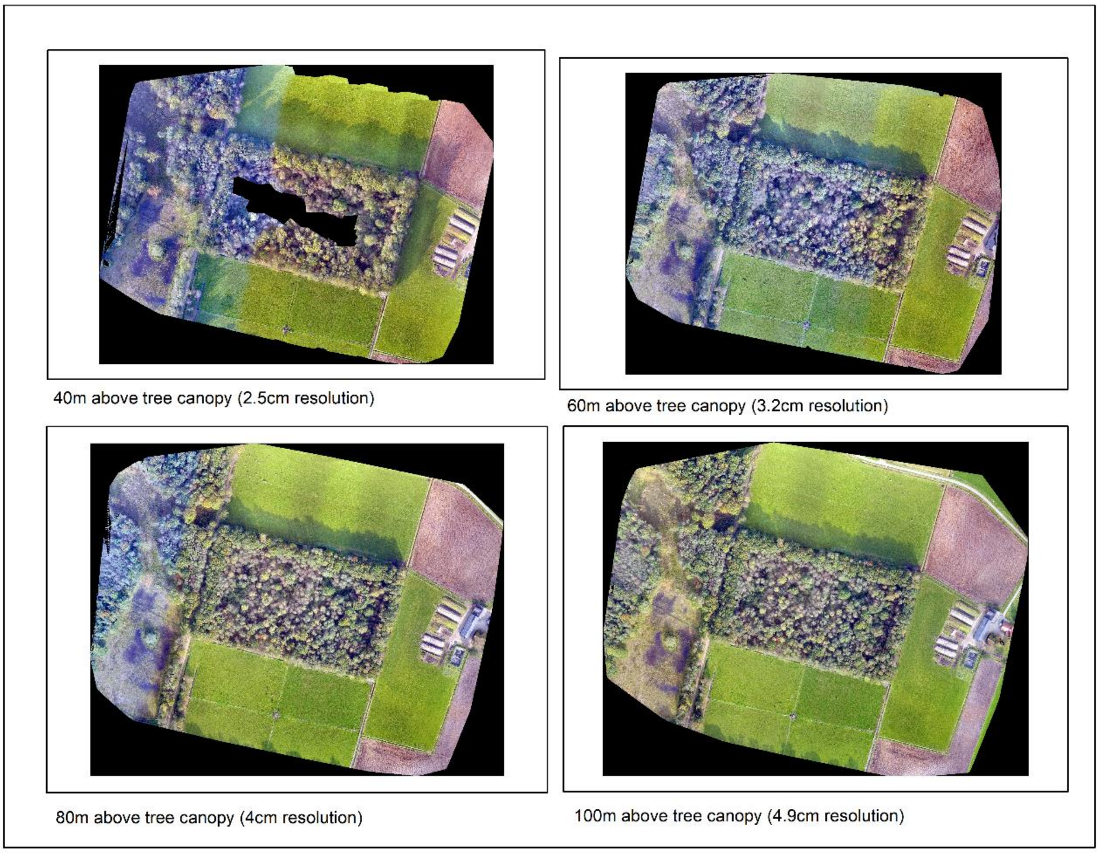

40m above tree canopy (2.5cm resolution)

60m above tree canopy (3.2cm resolution)

80m above tree canopy (4cm resolution)

100m above tree canopy (4.9cm resolution)

Appendix IV: Comparison of the confusion matrix obtained after the classification of tree species from UAV-RGB and UAV-Pleiades image configurations using Maximum Likelihood (ML), Random Trees (RT) and Support Vector Machines (SVM) in ArcMap.

UAV-RGB-MLC

	Sp	**Bi**	**Be**	**Wa**	**Sh**
Sp	499.4	78.0	69.1	1.1	364.5
Bi	32.5	722.7	83.6	63.3	862.2
Be	73.2	458.2	453.5	100.5	1405.2
Wa	0.2	18.5	0.0	2143.9	0.5
Sh	87.5	326.7	137.2	779.1	1471.6
CA(%)	49.3	41	18.2	99.1	52.5
	OA=51.7%, k=0.46				

UAV-Pleiades-MLC

	Sp	**Bi**	**Be**	**Wa**	**Sh**
Sp	472.5	23.3	28.4	30.2	1.7
Bi	6.1	381.8	53.6	6.9	4.0
Be	128.7	178.9	520.4	39.6	28.7
Wa	0.0	0.0	0.0	1252.0	0.0
Sh	11.9	20.1	19.2	0.0	126.5
CA(%)	85	84.4	14.3	100	71.2
	OA=70.8%, k=0.62				

UAV-RGB-RT

	Sp	**Bi**	**Be**	**Wa**	**Sh**
Sp	552.4	141.2	141.2	5.1	564.4
Bi	58.5	940.6	104.9	232.2	787.1
Be	6.8	39.3	61.0	9.6	135.3
Wa	1.1	41.9	0.3	2170.0	1.0
Sh	74.0	441.2	308.7	798.3	2616.2
CA(%)	39.3	44.3	24.2	98	61.7
	OA=62.0%, k=0.54				

UAV-Pleiades-RT

	Sp	**Bi**	**Be**	**Wa**	**Sh**
Sp	489.1	34.4	42.9	12.4	1.7
Bi	6.4	399.8	67.9	0.0	5.8
Be	104.1	145.6	484.3	1.4	27.0
Wa	0.0	0.0	0.0	1314.8	0.0
Sh	19.7	24.1	26.6	0.0	126.5
CA(%)	84.2	83.3	63.5	100.0	64.2
	OA=84.4%, k=0.797				

UAV-RGB-SVM

	Sp	**Bi**	**Be**	**Wa**	**Sh**
Sp	551.4	126.1	118.0	3.0	435.9
Bi	61.2	955.9	219.1	154.5	828.8
Be	27.0	154.1	240.9	20.1	554.0
Wa	1.4	46.8	0.1	2174.4	2.3
Sh	51.7	321.1	736.0	165.3	2283.0
CA(%)	44.7	43.1	24.2	97.7	61.7
	OA=62.0%, k=0.54				

UAV-Pleiades-SVM

	Sp	**Bi**	**Be**	**Wa**	**Sh**
Sp	486.4	43.2	32.3	6.5	1.6
Bi	5.1	391.9	80.6	0.0	6.6
Be	115.2	120.0	486.4	0.2	27.1
Wa	0.0	0.0	0.0	1322.0	0.0
Sh	12.5	48.9	22.3	0.0	125.6
CA(%)	84.2	83.3	63.5	100	64.2
	OA=84.4%, k=0.797				

Sp-Scots pine, Bi=Birch, Be=Beech, Wa=Water, Sh=Shadow, CA= Class accuracy, RT=Random trees, SVM=Support vector machines, ML=Maximum likelihood.

Appendix V: 2x2 Confusion matrix, comparing the performance of SVM, RT and ML classifiers using the McNemar's test.

	SVM-CC	SVM-WC	Total
RT-CC	23	12	35
RT-WC	16	62	78
Total	39	74	**113**

McNemar's Chi-squared statistic	0.321
Degrees of freedom	1
P-value	0.571
Odds ratio	0.75
Lower 95% CL	0.324
Upper 95% CL	1.69

	SVM-CC	SVM-WC	Total
ML-CC	22	13	35
ML-WC	23	55	78
Total	45	68	**113**

McNemar's Chi-squared statistic	**2.8**
Degrees of freedom	1
P-value	0.134
Odds ratio	0.565
Lower 95% CL	0.263
Upper 95% CL	1.164

	RT-CC	RT-WC	Total
ML-CC	24	9	33
ML-WC	17	63	80
Total	41	72	**113**

McNemar's Chi-squared statistic	**2.5**
Degrees of freedom	1
P-value	0.556
Odds ratio	0.733
Lower 95% CL	0.305
Upper 95% CL	1.709

CC=Correctly classified, WC=Wrongly classified

Appendix VI: Results of t-test investigating the significant difference between Field and modelled DBH for Scots pine at 95% confidence level.

	log(Modelled DBH (cm))	log(Field DBH (cm))
Variance	0.01	0.01
Observations	17.00	17
Pearson Correlation	0.76	
$\mu_1 - \mu_2$	0.00	
df	16.00	
t Stat	0.24	
P(T<=t) one-tail	0.408	
t Critical one-tail	1.75	
P(T<=t) two-tail	0.816	
t Critical two-tail	2.12	

Appendix VII: Results of Man Whitney U-test, comparing the difference in mean field derived and modelled DBH values for Birch species.

	Modelled DBH(cm)	Field derived DBH(cm)
Rank Sum	130	123
U	64	57
Minimum U	57	
Mean value	60.5	
SD	15.23	
p-value	0.409	

Appendix VIII: Results of t-test investigating the significant difference between field and modelled AGB for Scots *pine*, at 95% confidence level.

	log(Modelled AGB(kg/tree))	log(Field AGB(kg/tree))
Mean	2.23	2.13
Variance	0.04	0.06
Observations	17	17
Pearson Correlation	0.76	
$\mu_1 - \mu_2$	0	
df	16	
t Stat	2.49	
P(T<=t) one-tail	0.012	
t Critical one-tail	1.75	
P(T<=t) two-tail	0.024	
t Critical two-tail	2.12	

Appendix IX: Man Whitney U-test comparing mean field and modelled AGB values for Birch species at 95% confidence level.

	Modelled AGB(kg/tree)	Field derived AGB(kg/tree)
Rank Sum	130	123
U	64	57
Minimum U	57	
Mean value	60.5	
SD	15.23	
p-value	0.409	